Università degli Studi di Torino
Scuola di Dottorato
Dottorato di Ricerca in Fisica

Swimmer Dynamics in Complex Flows

Francesco Michele Ventrella

Tutor: Filippo De Lillo

A Gianluca, Dodò, Eugenio, Checco e Alessandro.

Per essere stati al mio fianco fino al traguardo.

Lontani ma vicini.

Contents

List of Pubblications

This thesis is based on the research carried out over the three-year doctoral program at Università di Torino, under the supervision of Professor Filippo De Lillo. The aim of this research is to study the behavior of microorganisms in fluids, with the formulation of theoretical and numerical models.

Part of the original work presented in this thesis has been published in the following journal articles:

1. Ventrella, F. M., Pujara, N., Boffetta, G., Cencini, M., Thiffeault, J. L., De Lillo, F. (2023). Microswimmer trapping in surface waves with shear. Proceedings of the Royal Society A, 479(2278), 20230280.

2. Ventrella, F. M., Boffetta, G., Cencini, M., De Lillo, F. (2024). Modeling straight and circle swimmers: from single swimmer to collective motion. The European Physical Journal E, 47(11), 65.

In particular, Chapter 6 is based on publication 1, and Chapter 8 on publication 2.

Part I

Swimmers in Low Reynolds Regime

Both our studies on microswimmers start from a microscopical description. For this reason, it is better to start this dissertation with an introduction to micro-hydrodynamics and, in particular, to the role of particles in fluids.

In fluid mechanics, the study of particles can be broadly categorized into two main types: active and passive particles. Understanding the behaviour of these particles is crucial for explaining complex systems, from fluid dynamics to biological systems.

Passive particles do not have the ability to move autonomously. Their motion is purely driven by external forces such as gravity, thermal fluctuations, or external fields. Passive particles are often used in modelling simpler systems, like colloids or dust particles in a fluid, and their dynamics follow classical equilibrium statistical mechanics principles.

On the other hand, active particles are self-propelled agents capable of converting stored or environmental energy into motion. These include living organisms such as bacteria, cells, or even synthetic microswimmers. Unlike passive particles, active particles exhibit non-equilibrium behavior, often leading to collective dynamics like swarming or flocking. Their study provides valuable insights into phenomena such as biological transport and the behavior of robotic systems. In this work, we refer to microswimmers as specific cases of active particles whose locomotion mechanisms are driven by propulsion organelles such as cilia or flagella.

The interaction between fluids and particles is a fundamental area of research in both physics and engineering, with significant implications for a wide range of applications. Understanding how particles behave in fluids, and how fluids respond to the presence of these particles, is essential for advancing knowledge in fields such as environmental science, medicine, materials science, and industrial processes.

One of the key reasons to study fluid-particle interactions is that they occur in numerous natural and man-made systems. In nature, phenomena like sediment transport, the dispersion of pollutants in the atmosphere, or the motion of microorganisms in biological fluids all involve complex fluid-particle interactions.

Additionally, the study of these interactions helps to improve technologies such as drug delivery systems, where understanding the dynamics of particles (like nanoparticles) in the bloodstream is critical for developing targeted therapies. Similarly, in climate science, the modelling of aerosols and particulate matter in the atmosphere is crucial for predicting

their effects on weather patterns and climate change.

From a theoretical perspective, fluid-particle interactions challenge classical fluid dynamics and statistical mechanics, especially when considering complex systems involving active particles or non-Newtonian fluids. These studies lead to new insights into non-equilibrium systems, turbulence, and multiphase flow behavior.

In this thesis, the fluid-particle interaction problem is studied with a particular focus on biological aspects, such as the formation of biological clusters in the ocean and the modelling of self-propelled swimmers capable of coupling and interact with similar agents. By exploring these biological contexts, the thesis aims to enhance the understanding of collective behaviors and aggregation mechanisms, providing insights relevant to both natural phenomena and potential technological applications.

Chapter 1

Non motile particles

1.1 The Stokes equation

The Navier-Stokes equations form the foundation of fluid dynamics and describe the motion of fluid substances such as liquids and gases. These equations express the balance of momentum in a fluid and account for internal viscosity, external forces, and pressure. Mathematically, the Navier-Stokes equations are a set of nonlinear partial differential equations that describe the flow of incompressible and compressible fluids. For an incompressible, Newtonian fluid, the equations can be written as:

$$\frac{\partial \mathbf{u}}{\partial t} + \mathbf{u} \cdot \nabla \mathbf{u} = -\frac{\nabla p}{\rho} + \nu \nabla^2 \mathbf{u} + \mathbf{f}, \tag{1.1}$$

$$\nabla \cdot \mathbf{u} = 0 \tag{1.2}$$

where $\mathbf{u}$ is the velocity field, p is the pressure field, ν is the cinematic viscosity and $\mathbf{f}$ represents external body forces (e.g. gravity). The equation represents the conservation of momentum, and it is coupled with the continuity equation, $\nabla \cdot \mathbf{u} = 0$, to ensure incompressibility.

Solving the Navier-Stokes equations is highly complex due to their nonlinear nature. While analytical solutions are known for a limited number of simplified cases, numerical methods are generally required to tackle real-world problems.

The Navier-Stokes equations can be non-dimensionalized to identify the dimensionless parameters that characterize fluid flow. To non-dimensionalize these equations, we introduce characteristic scales for the problem: L for the characteristic length scale, U for

the characteristic velocity scale and $T = L/U$ for the characteristic time scale. We define the following non-dimensional variables:

$$\tilde{\mathbf{u}} = \frac{\mathbf{u}}{U}, \quad \tilde{\mathbf{x}} = \frac{\mathbf{x}}{L} \quad \tilde{t} = \frac{tU}{L}, \quad \tilde{p} = \frac{p}{\rho U^2}, \quad \tilde{\mathbf{f}} = \frac{\mathbf{f}L}{U^2}. \tag{1.3}$$

Substituting these dimensionless variables into the Navier-Stokes equations, we obtain:

$$\frac{\partial \tilde{\mathbf{u}}}{\partial \tilde{t}} + \tilde{\mathbf{u}} \cdot \nabla_{\tilde{\mathbf{x}}} \tilde{\mathbf{u}} = \nabla_{\tilde{\mathbf{x}}} \tilde{p} + \frac{1}{Re} \nabla^2_{\tilde{\mathbf{x}}} \tilde{\mathbf{u}} + \tilde{\mathbf{f}}, \tag{1.4}$$

where we introduced the Reynolds number as:

$$\mathrm{Re} = \frac{UL}{\nu}. \tag{1.5}$$

The Reynolds number is the ratio of inertial forces (represented by the non linear term) to viscous forces in the flow. It is the only dimensionless parameter of NS and it characterizes the flow regime at the two extremes: for $\mathrm{Re} \gg 1$, inertial forces dominate, often resulting in turbulent flow and for $\mathrm{Re} \ll 1$, viscous forces dominate, leading to *creeping flow*.

In the latter case the left hand side in equation (1.2) could be neglected and one obtains:

$$\nabla p = \nu \nabla^2 \mathbf{u} + \mathbf{f}, \tag{1.6}$$

that is the Stokes equations describing creeping flows. Unlike the Navier-Stokes equation (1.2), the Stokes equation (1.6) is linear and time-independent. A primary consequence of this property is that the fluid field is fully determined once the boundary conditions are defined. Furthermore, a Stokes flow is time-reversal invariant. The latter property has important consequences in the context of biological organisms living in low Reynolds number regimes, as we will explore later in the text.

1.2 Sphere in creeping flow

The solution for the flow induced by a moving sphere at zero Reynolds number is a classical result of fluid dynamics. If the sphere has radius R, is located at the origin and translates with velocity $\mathbf{U}$ with no rotation, the flow velocity in the surrounding fluid at location $\mathbf{r}$ (magnitude r) away from the centre of the sphere is given by:

$$\mathbf{u}(\mathbf{r}) = \frac{3}{4}\mathrm{R}\left(\frac{\mathbf{1}}{r} + \frac{\mathbf{rr}}{r^3}\right) \cdot \mathbf{U} + \frac{1}{4}\mathrm{R}^3\left(\frac{\mathbf{1}}{r^3} - \frac{3\mathbf{rr}}{r^5}\right) \cdot \mathbf{U}. \tag{1.7}$$

(a) (b)

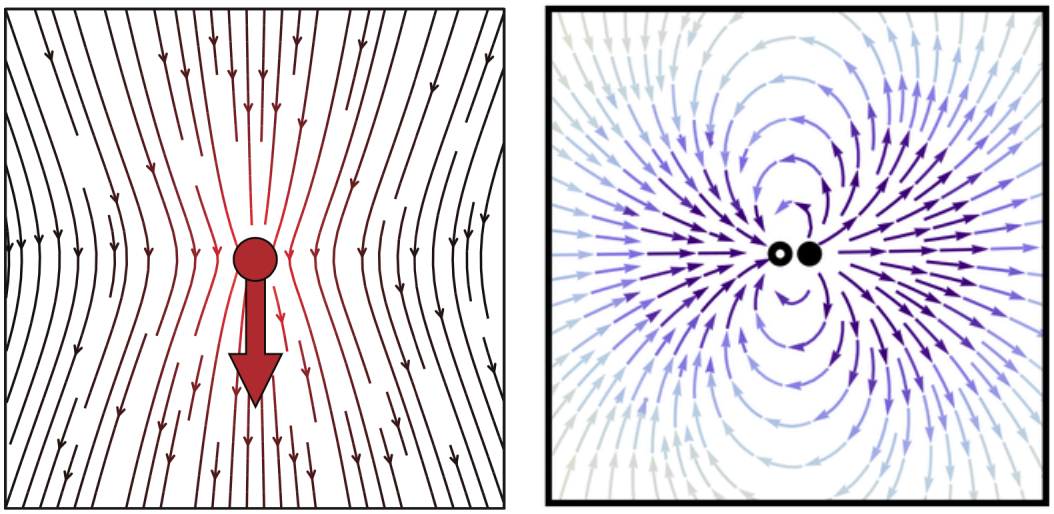

Figure 1.1: (a) Stokeslet: solution of the Stokes equation for point-like forcing. Image from [2]. (b) A source dipole. Image from [3].

This solution can be interpreted physically as due to the superposition of two flow singularities: a stokeslet (first term, decaying spatially as $1/r$) and a potential source dipole (second term, decaying spatially as $1/r^3$). A picture of these two flow perturbations are in figure 1.1. From equation (1.7), we can calculate the drag force $\mathbf{F}$ exerted on the sphere by the fluid considering the total stress exerted on the sphere surface [1]. This leads to the *Stokes' formula*:

$$\mathbf{F} = 6\pi\mu R\mathbf{U}, \tag{1.8}$$

where $\mu = \nu\rho$ is the dynamic viscosity.

The Stokeslet is the name given to the Green function for Stokes flows, induced by a point force $\mathbf{F}$ applied locally as a Dirac delta function. If the singularity is located at the origin, the fluid velocity $\mathbf{u}_F$ is solution of:

$$0 = -\nabla p + \mu\nabla^2\mathbf{u}_F + \delta(\mathbf{r})\mathbf{F}, \quad \nabla\cdot\mathbf{u}_F = 0 \tag{1.9}$$

and given by:

$$\mathbf{u}_F(\mathbf{r},\mathbf{F}) = \frac{1}{8\pi\mu}\left(\frac{\mathbf{1}}{r} + \frac{\mathbf{rr}}{r^3}\right)\cdot\mathbf{F}. \tag{1.10}$$

Together with eq. (1.8), the latter gives the first term on the right-hand side of Eq. (1.7).

The second flow in Eq. (1.7) is a potential source dipole. If such a dipole of strength $\mathbf{M}$ is located at the origin, the corresponding flow singularity is given by:

$$\mathbf{u}_{SD}(\mathbf{r}, \mathbf{M}) = \frac{1}{4\pi}\left(\frac{\mathbf{1}}{r^3} - \frac{3\mathbf{rr}}{r^5}\right) \cdot \mathbf{M}. \tag{1.11}$$

This flow can be interpreted as a source and a point sink merging together. Consider a three-dimensional point source flow whose strength m measures the flow rate injected by the source into the fluid. If the source is located at the origin, the corresponding flow, with velocity denoted $\mathbf{u}_m$, is potential (i.e., irrotational), incompressible and is given classically by

$$\mathbf{u}_m(\mathbf{r}; m) = \frac{m}{4\pi}\frac{\mathbf{r}}{r^3} \tag{1.12}$$

which may be verified using spherical symmetry and the condition that the volume flux through any surface containing the origin is m. A source dipole is obtained by placing a sink of strength $-m$ at a position $\mathbf{d}$ relative to a source of strength m, and taking the limit $|\mathbf{d}| \to 0$ while the product $m|\mathbf{d}|$ remains finite. The flow is obtained by assuming a linear superposition and using a Taylor expansion, so that

$$\mathbf{u}_m(\mathbf{r}; m) + \mathbf{u}_m(\mathbf{r} - \mathbf{d}; -m) \approx \mathbf{d} \cdot \nabla \mathbf{u}_m = \frac{1}{4\pi}\left(\frac{1}{r^3} - \frac{3\mathbf{rr}}{r^5}\right) \cdot (m\mathbf{d}), \tag{1.13}$$

which is exactly Eq. (1.11) with $\mathbf{M} = m\mathbf{d}$.

In the context of this work, Eq. (1.7) plays a crucial role in the analysis due to the explicit dependence on R.

1.3 The Jeffery equation

The Jeffery equation describes the orientation dynamics of an ellipsoidal particle immersed in a viscous fluid subjected to a linear flow. Consider an ellipsoidal particle with a unit vector $\mathbf{p}$ indicating the direction of its principal axis [4]. The flow around the particle is assumed to be a simple linear flow. This is true in the case of small particles whose size allows for approximating fluid gradients along the body as linear.

According to Jeffery's theory , the time evolution of the orientation vector $\mathbf{p}$ of an ellipsoid, characterised by the two semi-axis a and b with $a > b$, in a flow field with rate-of-strain tensor $\mathbf{S}$ and vorticity tensor $\mathbf{\Omega}$ is given by:

$$\dot{\mathbf{p}} = \mathbf{\Omega}\mathbf{p} + \lambda \left[\mathbf{S}\mathbf{p} - \left(\mathbf{p}^T \mathbf{S}\, \mathbf{p} \right) \mathbf{p} \right], \tag{1.14}$$

where $\mathbf{\Omega} = \frac{1}{2}\left(\nabla\mathbf{u} - (\nabla\mathbf{u})^T\right)$ is the vorticity tensor (related to the rotation of a volume of fluid), $\mathbf{S} = \frac{1}{2}\left(\nabla\mathbf{u} + (\nabla\mathbf{u})^T\right)$ is the rate-of-strain tensor (connected with the rate of the deformation of the volume of fluid) and $\lambda = \frac{a^2-b^2}{a^2+b^2}$ is the shape parameter.

Jeffery's equation shows that the rotation of an ellipsoidal particle is influenced by both the vorticity tensor $\mathbf{\Omega}$ and the rate-of-strain tensor $\mathbf{S}$. The term involving λ reflects the alignment of the particle with the flow and depends on the particle's shape. For example: when $\lambda = 0$, the particle behaves like a sphere and is affected only by the rotational term, when $\lambda \neq 0$, the particle experiences additional alignment and rotation effects due to its shape and, in particular, when $\lambda = 1$, the particle behaves like a thin rod and tends to align with the local fluid velocity.

1.3.1 2D case

As an example let's consider the case of a two-dimensional parallel flow $\mathbf{u} = (u_x(y), 0)$.

Let's introduce a 2D reference system in which the swimming angle is measured from the horizontal direction ($n_x = \cos\theta$, $n_y = \sin\theta$) and let's place a small particle in y_0. In this framework the equation (1.14) could be simplified into the following:

$$\dot{\theta} = -S[1 - \lambda\cos(2\theta)] \tag{1.15}$$

where $S = \frac{1}{2}\frac{\partial u_x}{\partial y}\Big|_{y_0}$. The equation admits a solution that is:

$$\theta(t) = \operatorname{arccot}(2St + c) \tag{1.16}$$

where c determines the initial angle. This solution describes the rotation of the major axis of the ellipsoid and will be later applied to the case of the Kolmogorov flow, which is a simple two dimensional parallel flow with a sinusoidal profile.

Chapter 2

Motile particles: Microswimmers

Microswimmers are microscopic organisms or synthetic particles capable of self-propulsion in a fluid environment. These tiny swimmers include biological entities such as bacteria, algae, and sperm cells, as well as engineered micro-robots designed for medical or industrial applications. Microswimmers operate in a low Reynolds number regime, significantly affecting their movement strategies (see Fig. 2.1). These microorganisms and artificial swimmers employ various propulsion mechanisms like flagella, cilia, or chemical reactions. The study of microswimmers is crucial for understanding biological processes, as their behaviours offer insights into both natural and engineered transport phenomena at the microscopic scale.

2.1 The Scallop Theorem

The Scallop Theorem was proposed by Edward Purcell in 1977 [6]. It states that a simple, time-reversible motion cannot produce net propulsion in a highly viscous environment. This theorem is named after the motion of a scallop, which moves forward by simply opening and closing its shell in a time-symmetric manner. Such motion is possible only at finite Re.

At low Reynolds numbers, where viscous forces dominate over inertial forces, the governing Stokes equations is linear and time-reversible. As a result, if a swimmer's movement is identical when performed in reverse (a reciprocal motion), it will return to its original position without making any net progress. For instance, if a microswimmer

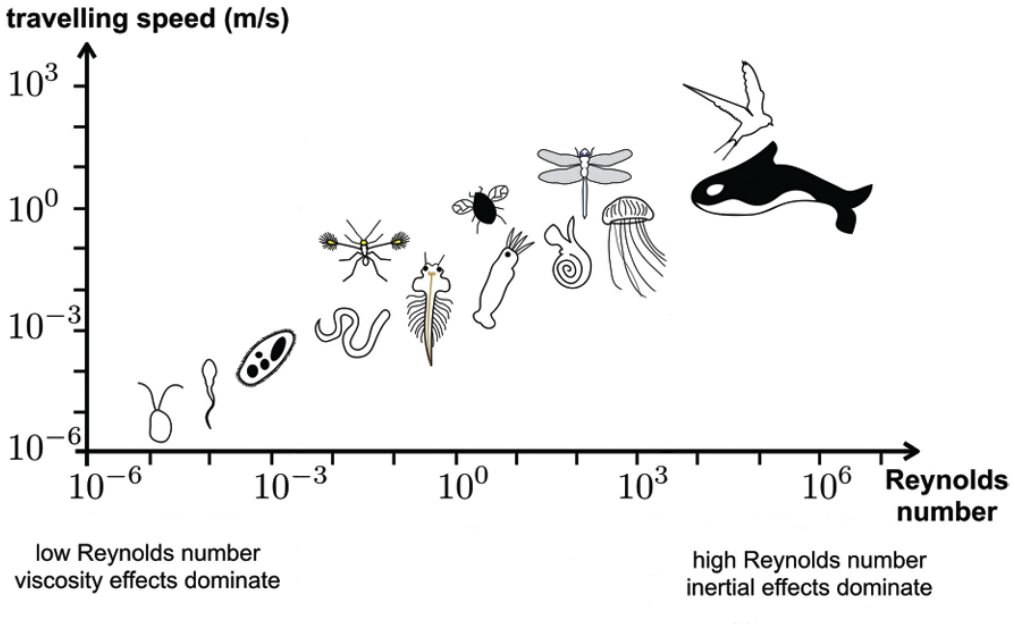

Figure 2.1: Reynolds numbers for different species. The organisms shown schematically from low to high Reynolds numbers are: algae, bacterium, paramecium, nematode, fairyfly, brine shrimp, larval squid, wasp, pteropod, dragonfly, jelly fish, whale, swallow. Image from [5].

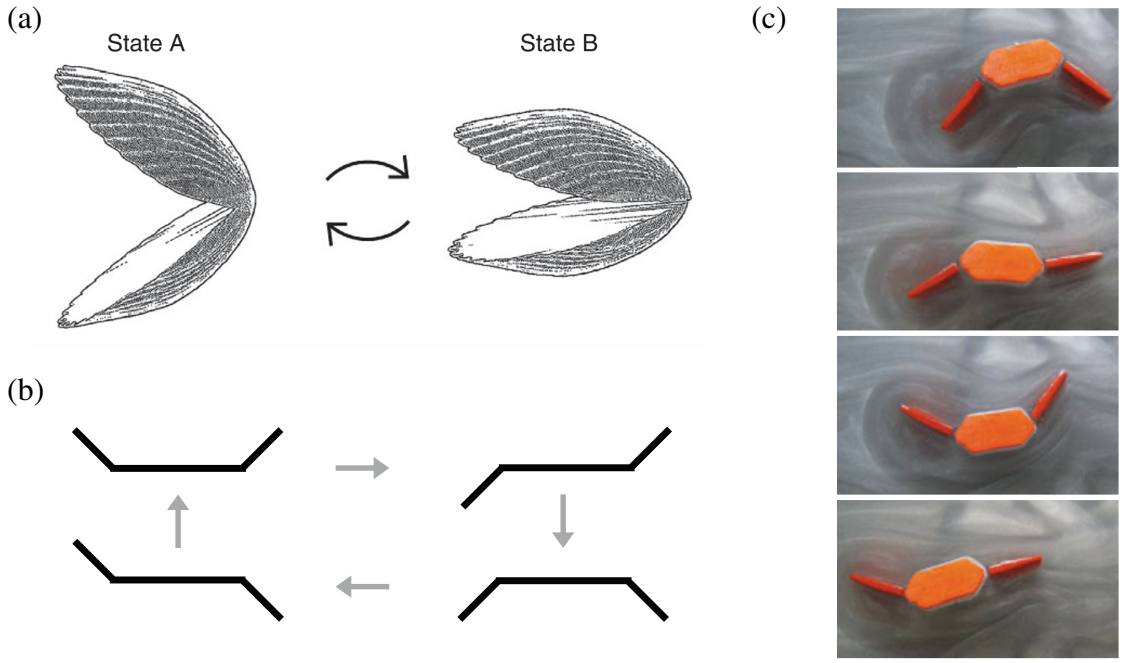

Figure 2.2: (a) Schematic drawing of Purcell's scallop with reciprocal motion. Image from [8]. (b) Purcell's two-hinge swimmer. (c) Macroscale experimental realisation of Purcell's swimmer [7]

tries to move like a scallop by repeatedly opening and closing, it will not achieve forward motion because the fluid's response is symmetric in time (Fig. 2.2(a)). For simple swimmers, we therefore need at least two degrees of freedom and to actuate them in a non-reciprocal way. Examples of such swimmers include Purcell's two-hinged swimmer illustrated schematically in figure 2.2(b) with a macroscale experimental implementation shown in panel (c) [7]. The Scallop Theorem implies that microswimmers must employ non-reciprocal motion, i.e. a motion which does not achieve propulsion. This can be achieved through flexible appendages like rotating flagella, the coordinated beating of cilia, or shape-changing mechanisms. For instance, some bacteria like *Escherichia coli*, swim using rotating helical flagella, while sperm cell propels itself by generating wave-like motions along its flagellum.

Although the detailed description of the swimming mechanism is beyond the scope of this thesis, it is instructive to see how simple dynamic models can be introduced according to the scallop theorem. The Najafi-Golestanian model is a theoretical model describing the propulsion mechanism of a simple three-sphere microswimmer at low Reynolds numbers.

This model is significant because it demonstrates a minimal, non-reciprocal mechanism to achieve propulsion in a highly viscous environment, overcoming the constraints posed by the Scallop Theorem (Fig. 2.3).

The model consists of three aligned spheres connected by two arms of varying lengths. These arms can extend and contract, mimicking internal degrees of freedom. The key aspect of the model is the sequential change in the lengths of the arms connecting the spheres, which ensures a non-reciprocal motion. The three spheres are denoted as 2, 1, and 3, with arms of lengths L_{12} and L_{13} connecting the spheres. The spheres undergo a sequence of expansions and contractions in the lengths L_{12} and L_{13}, controlled by a periodic function. The motion is carefully chosen to be non-reciprocal, such that the sequence of length changes in the arms does not retrace the same steps in reverse order. This non-reciprocal motion generates a net displacement of the entire three-sphere structure over a period of oscillation, allowing the swimmer to move in a specific direction. On the contrary, in the case in which the system is described by only one degree of freedom, for example only the left arm extends and retracts, the system agrees with the Scallop theorem and no net motion is produced. The model successfully illustrates how a simple configuration can achieve propulsion by breaking time-reversal symmetry, even in the absence of inertia.

2.2 Swimming strategies

For the vast majority of small organisms swimming occurs with no net force. For a simple swimmer, far from the cell there is no Stokeslet component of the flow, and the dominant flow is a force dipole, decaying spatially as $1/r^2$. The physical origin of this force dipole is illustrated in figure 2.4 for three microorganisms, namely a swimming spermatozoon, a bacterium and a biflagellated alga. In all cases, the flagella produce local hydrodynamic forces (drawn with empty arrows) as they move relative to the surrounding fluid. This results in locomotion and therefore the moving cell exerts a force on the fluid in the opposite direction (filled arrows). Since only the flagella create propulsion but both the flagella and the cell body experience drag, the centre of drag and the centre of propulsion are physically separated, leading to a dipolar structure of the induced flow. This simple

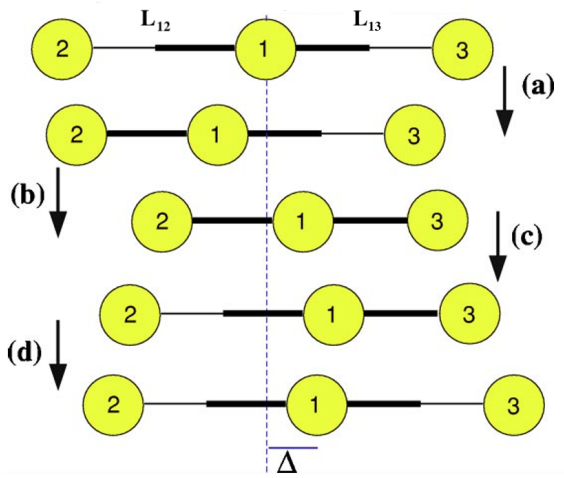

Figure 2.3: The proposed non-reciprocal motion of the swimmer follows a complete cycle consisting of four consecutive stages that break time-reversal symmetry: (a) the left arm contracts; (b) the right arm then contracts; (c) the left arm extends back to its original length; and finally, (d) the right arm returns to its original length. By completing this cycle, the entire system moves to the right by a displacement of Δ. Image from [9]

physical picture can be extended naturally to the case of more complex geometries, larger organisms and multiple flagella.

To compute the flow due to a force dipole, consider a force $-F\mathbf{e}$ located at the origin and an equal and opposite force $F\mathbf{e}$ at location $\epsilon l\mathbf{d}$ away, where $\mathbf{d}$ is a unit vector and ϵ a small dimensionless number. For sake of simplicity equation (1.10) could be rewritten as:

$$\mathbf{u}(\mathbf{r}) = F\mathbf{G}(\mathbf{r}, \mathbf{e}) \tag{2.1}$$

where the vector $\mathbf{G}$ is related to the Green's function of the Stokes equations. By the linearity of Stokes equations, the total flow $\mathbf{u}$ is given by a superposition of the two Stokeslet produced by the two forcing:

$$\mathbf{u}(\mathbf{r}) = F\mathbf{G}(\mathbf{r} - \epsilon l\mathbf{d}, \mathbf{e}) - F\mathbf{G}(\mathbf{r}, \mathbf{e}) = -\epsilon l F(\mathbf{d} \cdot \nabla)\mathbf{G}(\mathbf{r}, \mathbf{e}) + O(\epsilon^2). \tag{2.2}$$

Defining $\mathcal{P} = \epsilon l F$ the *dipole strength* one can write the field produced by the dipole at first order as:

$$\mathbf{u}_{\text{dipole}}(\mathbf{r}, \mathbf{e}.\mathbf{d}) = -\mathcal{P}(\mathbf{d} \cdot \nabla)\mathbf{G}(\mathbf{r}, \mathbf{e}) \tag{2.3}$$

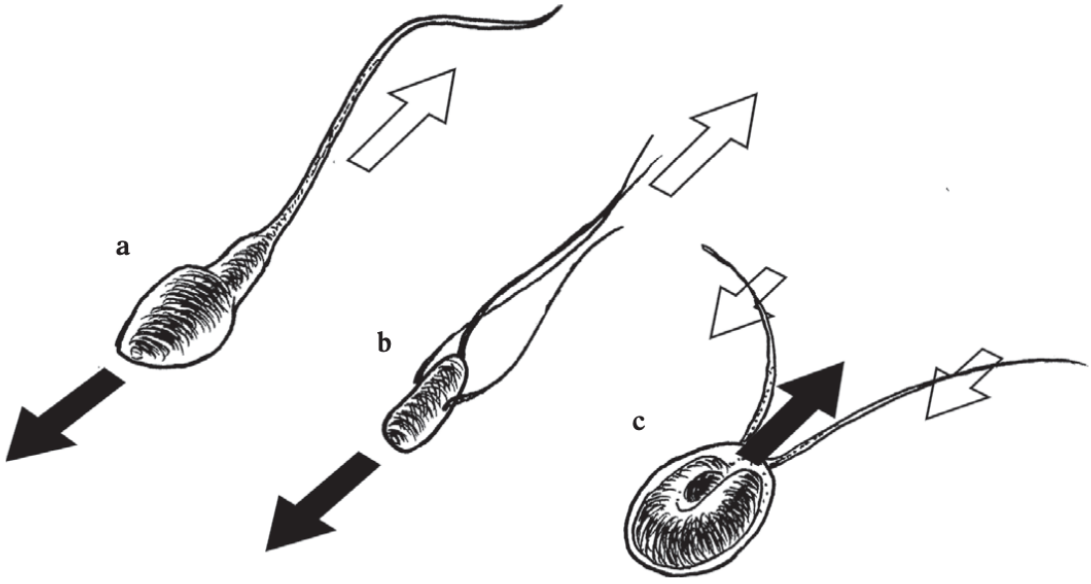

Figure 2.4: Schematic force dipoles for swimming microorganisms. Force-free swimming of a spermatozoon (a) and a bacterium (b). In both cases, the moving cell body induces a local frontward force on the surrounding fluid (drawn with filled arrow) while the flagellum induces a backward propulsive force (empty arrow) leading to a force dipole. In contrast, for a biflagellated alga (c), the force dipole is reversed in sign and the cell is pulling itself into the fluid. Image from [10].

Using the standard results from vector calculus one obtains (see [10] for full derivation):

$$\mathbf{u}_{\text{dipole}}(\mathbf{r},\mathbf{e},\mathbf{d}) = \frac{\mathcal{P}}{8\pi\mu}\left[\frac{(\mathbf{d}\times\mathbf{e})\times\mathbf{r}}{r^3} - \frac{(\mathbf{d}\cdot\mathbf{e})\,\mathbf{r}}{r^3} + \frac{3(\mathbf{e}\cdot\mathbf{r})(\mathbf{d}\cdot\mathbf{r})\,\mathbf{r}}{r^5}\right] \tag{2.4}$$

The first term on the right-hand side is antisymmetric in $\mathbf{d}$ and $\mathbf{e}$ and thus disappears when $\mathbf{d} = \mathbf{e}$. In contrast, the other two terms are symmetric, and when $\mathbf{d} = \mathbf{e}$ they lead to the axisymmetric solution. It is possible to use the symmetric/antisymmetric decomposition:

$$\mathbf{u}_{\text{dipole}}(\mathbf{r},\mathbf{e},\mathbf{d}) = \mathbf{u}^{\text{sym}}_{\text{dipole}}(\mathbf{r},\mathbf{e},\mathbf{d}) + \mathbf{u}^{\text{antisym}}_{\text{dipole}}(\mathbf{r},\mathbf{e},\mathbf{d}) \tag{2.5}$$

where

$$\mathbf{u}^{\text{sym}}_{\text{dipole}}(\mathbf{r},\mathbf{e},\mathbf{d}) = \frac{1}{2}\left[\mathbf{u}_{\text{dipole}}(\mathbf{r},\mathbf{e},\mathbf{d}) + \mathbf{u}_{\text{dipole}}(\mathbf{r},\mathbf{d},\mathbf{e})\right] \tag{2.6}$$

$$= \frac{\mathcal{P}}{8\pi\mu}\left[-\frac{(\mathbf{d}\cdot\mathbf{e})\,\mathbf{r}}{r^3} + \frac{3(\mathbf{e}\cdot\mathbf{r})(\mathbf{d}\cdot\mathbf{r})\,\mathbf{r}}{r^5}\right] \tag{2.7}$$

$$\mathbf{u}^{\text{sym}}_{\text{dipole}}(\mathbf{r},\mathbf{e},\mathbf{d}) = \frac{1}{2}\left[\mathbf{u}_{\text{dipole}}(\mathbf{r},\mathbf{e},\mathbf{d}) - \mathbf{u}_{\text{dipole}}(\mathbf{r},\mathbf{d},\mathbf{e})\right] \tag{2.8}$$

$$= \frac{\mathcal{P}}{8\pi\mu}\left[\frac{(\mathbf{d}\times\mathbf{e})\times\mathbf{r}}{r^3}\right] \tag{2.9}$$

The symmetric solution is a particular case of the so-called *stresslet* (Fig. 2.5(a)), while the antisymmetric solution is interpreted as due to a net torque applied to the fluid and is called *rotlet* (Fig. 2.5(b)).

The sing of $\mathcal{P}$ allows the swimmers to be classified into two main categories. Cells characterised by $\mathcal{P} > 0$ are classified as *pushers*. In contrast, cells with $\mathcal{P} < 0$ are classified as *pullers*.

The ability of microswimmers to achieve optimal propulsion strategies is of crucial importance for their locomotory performance and survival at low Reynolds numbers. From a qualitative point of view pushers, such as *E. Coli* and spermatozoa, swim body-first with their flagella behind the cell body propelling themselves by pushing fluid outward from their back with the flagellum and, at the same time, pushing the fluid away from the front due to the resistance of the body. Under the hypothesis of incompressibility, this propulsion mechanism creates a characteristic flow field, with fluid being pulled inward along the sides of the swimmer and pushed outward along its axis of movement (Fig. 2.4(a-b)). This is an example of an *extensile* force dipole ($\mathcal{P} > 0$). Pullers, such as *Chlamydomonas*, whose flagella are located in front of the swimmer, drag the body

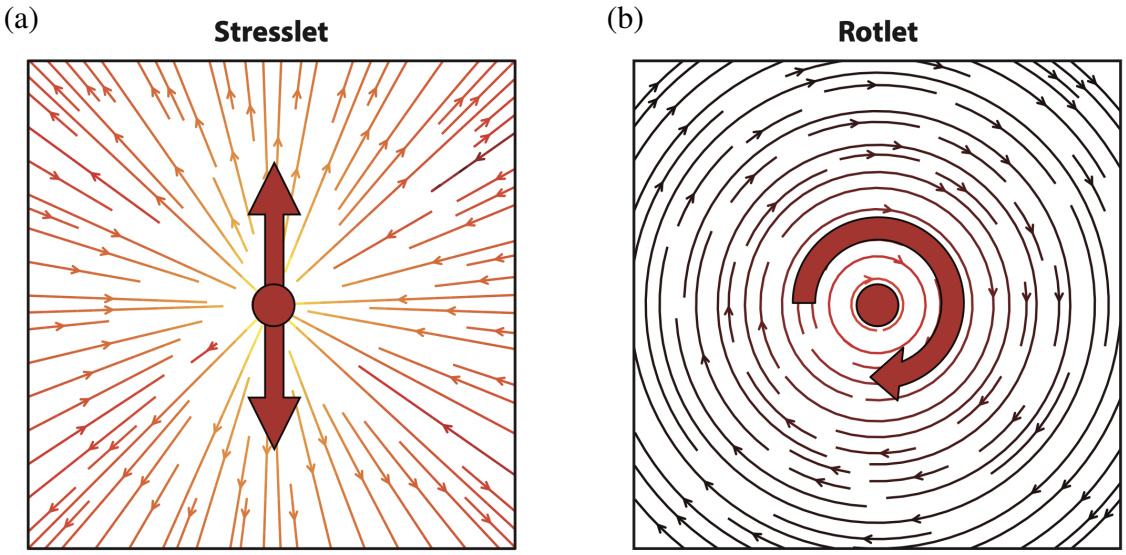

Figure 2.5: Streamlines driven by stresslet, and rotlet singularities in Stokes flow. Image from [2]

forward by pulling fluid inward at the front and pushing it outward along their sides (Fig. 2.4(c)), following the scheme of a *contractile* force dipole ($\mathcal{P} < 0$).

2.3 Theoretical models for motility

Microorganisms evolved specialized organelles like flagella and cilia to facilitate swimming in liquid environments [11]. Eukaryotic flagella and cilia share an almost identical internal structure, characterized by a series of doublet microtubules (Fig. 2.6(a)). These are interconnected by dynein molecular motors, which generate sliding forces that enable active bending [12, 13]. While the distinction between flagella and cilia is not strictly defined, flagella are typically long and sparse, whereas cilia are shorter and more numerous. For instance, the ciliate *Paramecium caudatum* (Fig. 2.6(b)) has a body approximately $250\mu m$ long and $50\mu m$ wide, covered with around 15.000 cilia, each approximately 10-15μm long and $0.2\mu m$ in diameter. These cilia beat at a frequency of about $30Hz$, enabling the organism to swim at speeds of roughly 10 body lengths per second. The density of cilia is approximately 50 per $100\mu m^2$ [14]. Cilia generate propulsion through a cycle of effective and recovery strokes (Fig. 2.6(c)). These strokes propagate across the cell surface in coordinated patterns known as *metachronal* waves, driving movement

efficiently (Fig. 2.6(d)).

The aim of theoretical studies here presented is to model the continuous movement of flagella and cilia. A precise mathematical treatment of this problem will not be provided, as it falls outside the scope of this work, but it is useful to highlight the existence of models that simulate the mean flow induced by the motion of cilia and flagella. The two main models found in the literature are the *waving sheet model* and the *squirmer model*.

2.3.1 The waving sheet model

The model was introduced in 1951 by Taylor [15]. In his paper, Taylor assumed the possibility of swimming without inertia in a low Re regime. Since microorganisms were observed to deform their flagella in a wave-like fashion to produce propulsion from the back (i.e., spermatozoa), he focused on the simplest setup possible, namely that of a flexible infinite two-dimensional sheet deforming as a travelling wave of transverse displacements. With reference to Figure 2.6(d), it is worth noting that the envelope surface of cilia displacement (i.e. a metachronal wave) is mathematically described as a flexible two-dimensional sheet, such that this model can be applied to both flagellate and ciliate swimmers. The main assumption for this mathematical treatment is that the flagellum exhibits purely planar dynamics, allowing the reduction from the three-dimensional space in which the swimmer exists to two-dimensional plane (see Fig 2.7(a)). The kinematics of material points on the sheet (i.e. the flagellum), (x_s, y_s), is described by the periodic waving motion:

$$x_s = A\cos(kx - \omega t - \phi) \quad \text{and} \quad y_s = B\sin(kx - \omega t), \tag{2.10}$$

where A is the amplitude of the longitudinal wave, B is the transverse amplitude, k and ω are respectively the wavenumber and angular frequency, and ϕ is a phase difference between the two deformation modes (Fig. 2.7(a)). With this formulation, the trajectories of material points are ellipses in (x, y) space.

The fluid motion is solved above the sheet in the region $y > y_s$, and the flow is described by the Stokes equations. Since the kinematics of the sheet is prescribed, the no-slip boundary condition sets the value of the flow velocity on the sheet, namely

$$\mathbf{u}(x = x_s, y = y_s) = \frac{\partial}{\partial t}(x_s, y_s). \tag{2.11}$$

(a)

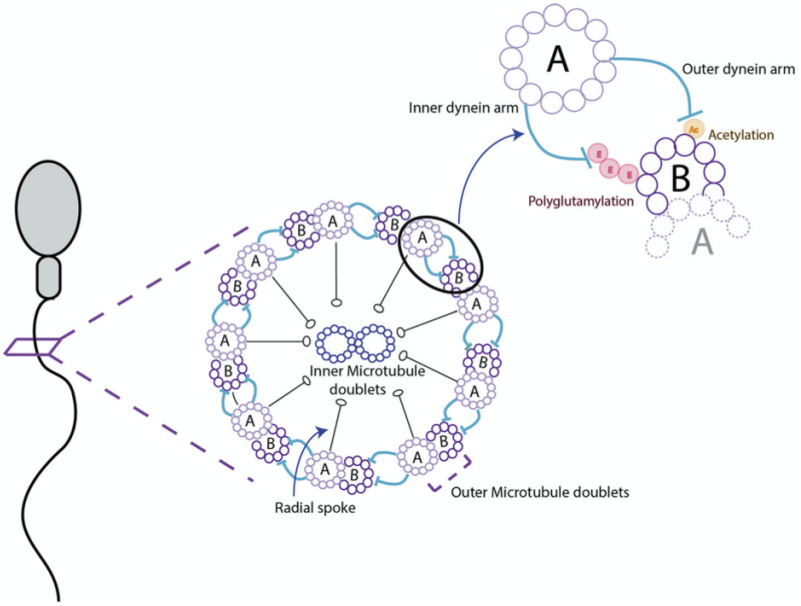

(b)

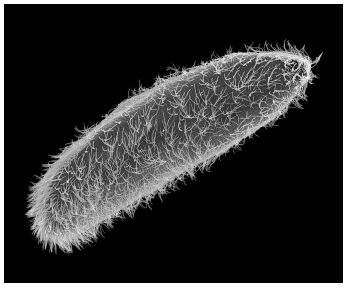

(c)

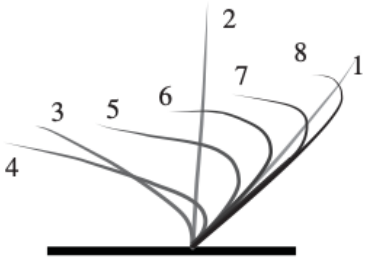

(d)

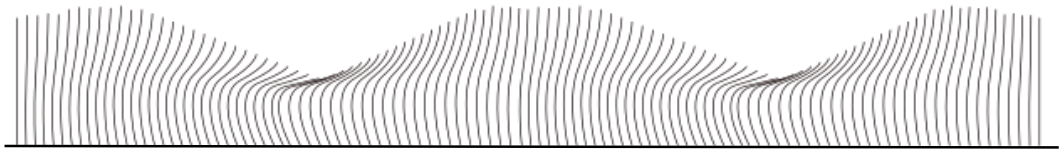

Figure 2.6: (a) Molecular mechanism of flagellar beating. The axoneme of the spermatozoon is formed by nine outer doublets of microtubules (A and B) and an inner microtubule doublet. The movement of the flagella is powered through the interaction of the inner and outer dynein arms extending from the A tube of the outer doublets with the B tube of the adjacent doublet. Image from [13]. (b) Scanning electron micrograph of Paramecium caudatum. (c) The cilium undergoes an *effective stroke*, creating a large force on the fluid (snapshots 1 to 4))and this is followed during the second half of the motion by a distinct *recovery stroke*, where the cilium bends to decrease its hydrodynamic drag (snapshots 5 to 8)). (d) Coordinated ciliary movement creates the metachronal waves. Each cilium performs an effective stroke and a recovery stroke as shown in panel (c).

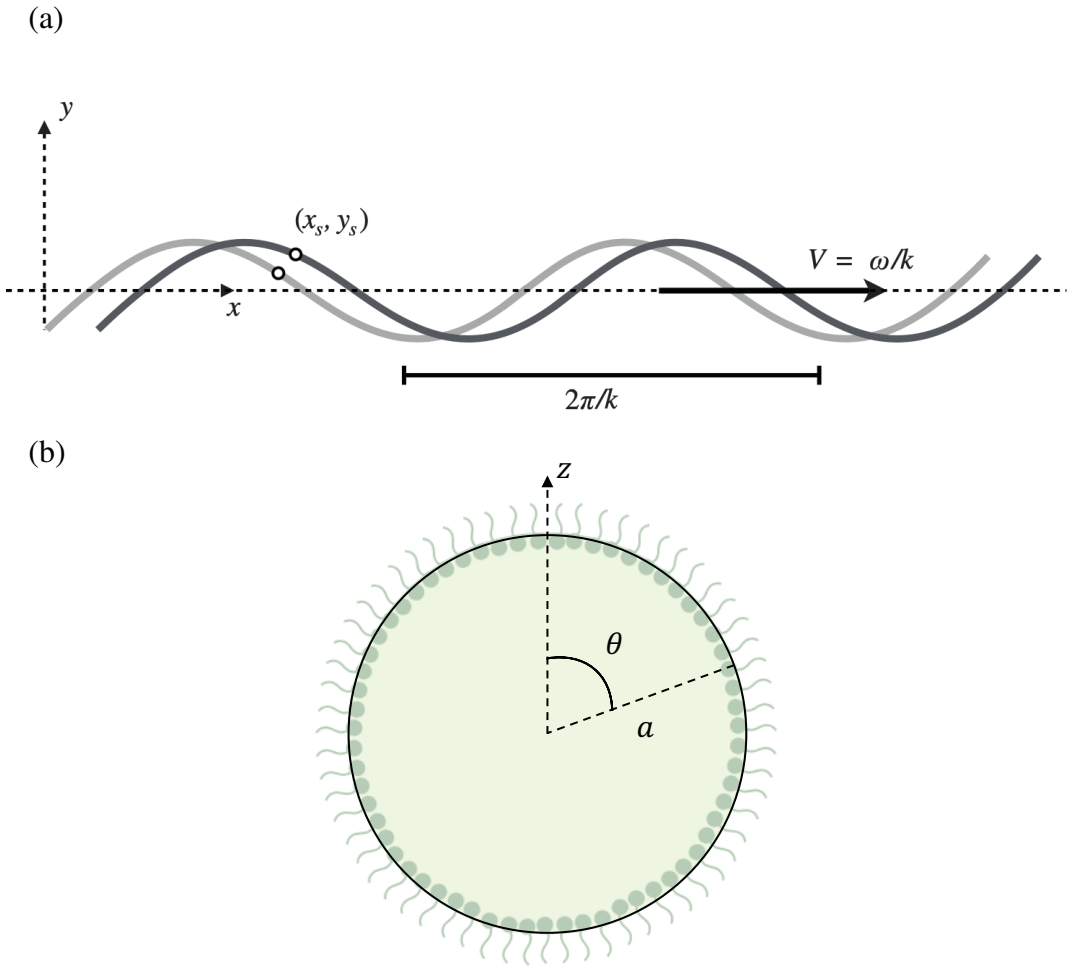

Figure 2.7: (a) A waving sheet of wavelength $2\pi/k$, frequency ω, and wave speed $V = \omega/k$. Working in a frame in which the sheet centreline is stationary, x and y are the lab frame coordinates, while x_s and y_s denote the material points on the sheet. (b) Bidimensional polar coordinate relative to a spherical squirmer.

Far from the sheet, we assume that no net force or pressure gradient be induced and we solve for the unknown velocity U induced along the direction of propagation of the wave as

$$\lim_{y\to\infty} \mathbf{u} = U\mathbf{e}_x. \tag{2.12}$$

The resulting value of U is then interpreted as the opposite of a locomotion speed. In the long wave limit, a perturbative approach can be applied (further mathematical details in [10]). The solution for the flow induced at infinity is

$$U = \frac{\omega k}{2}(B^2 + 2AB\cos\phi - A^2). \tag{2.13}$$

This model could be used to describe the flow field produced by singular flagellum and metachronal waves. This result is in agreement with experiments where, for example, a spermatozoon is seen to send bending waves propagating from the cell body towards the free (distal) end of the flagellum, leading to locomotion head first [16].

2.3.2 The squirmer model

In 1952, M.J. Lighthill pioneered the mathematical analysis of ciliary swimming [17]. He modelled the surface generated by the ciliary tips, expressing their displacement and deformation as velocity boundary conditions. This approach, now known as the *squirmer model*, has since been refined and extended by researchers like Blake [18] and Pedley [19] to analyse various aspects of ciliary swimming.

The squirmer model is a widely used theoretical framework to study the locomotion of microorganisms in viscous environments, particularly at low Reynolds numbers. The squirmer model provides a simplified mathematical representation of a microswimmer. The squirmer is modelled as a spherical or ellipsoidal particle. Instead of explicitly modelling appendages like flagella or cilia, here, the surface of the body undergoes periodic small-amplitude deformation of its surface, leading to instantaneous velocity boundary conditions applied on an effective spherical frame.

We use spherical coordinates with the origin at the centre of a sphere of radius a in order to describe the flow (Fig. 2.7(b)). Although the original squirmer model imposed no restriction on surface velocity, many studies have assumed for simplicity that the surface

velocity is steady, axisymmetric (and thus has no dependence on the azimuthal angle ϕ) and tangential to the surface. In this simple situation, the tangential surface velocity u_θ of the spherical squirmer is described by spherical harmonics or series expansions. In order to derive the general solutions $u_\theta(r,\theta,t)$ and $u_r(r,\theta,t)$ the goal is to solve the Stokes equations thanks to the Legendre polynomial approach for axisymmetric problems and imposing the boundary conditions given by

$$u_\theta(a,\theta,t) = \sum_n B_n(t)\frac{2}{n(n+1)}P_n^{'}(\cos\theta)\sin\theta, \tag{2.14}$$

$$u_r(a,\theta,t) = \sum_n A_n(t)P_n(\cos\theta) \tag{2.15}$$

where P_n is the Legendre polynomial and the coefficients and $B_n(t)$ and $A_n(t)$ are implicit defied by P_n (refer to [10] for details). It is possible to show that B_1 and B_2 are related respectively to the Stokeslet and stresslet mode, thus, neglecting $n > 2$ terms, it is possible to obtain the general solution:

$$u_\theta(r,\theta,t) = \frac{B_1}{2}\left[\left(\frac{a}{r}\right)^3 + \frac{a}{r}\right]\sin\theta + B_2\left[\left(\frac{a}{r}\right)^4\right]\sin\theta\cos\theta, \tag{2.16}$$

$$u_r(r,\theta,t) = B_1\left[\left(\frac{a}{r}\right)^3 - \frac{a}{r}\right]\cos\theta + \frac{B_2}{2}\left[\left(\frac{a}{r}\right)^4 - \left(\frac{a}{r}\right)^2\right]\left(3\cos^2\theta - 1\right). \tag{2.17}$$

This solution exhibits the same decaying behavior with respect to r as the equation (1.7) which similarly describes the behaviour of a sphere in a fluid. Moreover the ratio B_2/B_1 defines a pusher squirmer if it is greater than zero and viceversa for the puller.

We conclude by comparing the predictions of the squirmer model with experimental data. In particular, we focus on the ciliated green alga *Volvox carteri*, a multicellular organism with an approximately spherical shape (schematically represented in figure 2.7(b)). The coordinated motion of its cilia generates large-scale flows, driving the organism's locomotion.

Figure 2.8 presents time-averaged flow measurements obtained using particle image velocimetry, showing the flow induced by multiple flagella when the cell is immobilized by a pipette [20]. The model effectively reproduces the main characteristics of the experimental observations, including the slight front-back asymmetry, the peak flow velocity near the equator, and the overall structure of the flow field.

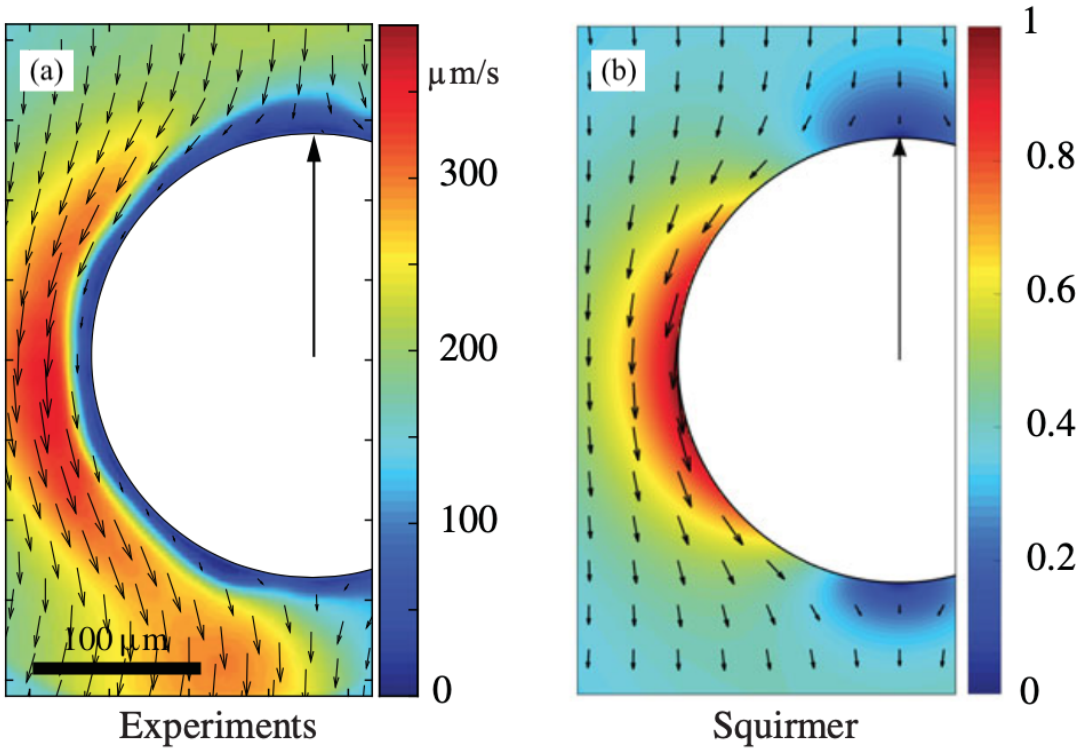

Figure 2.8: (a) Measured time-averaged flow around the cell held in place by a pipette [20]. (b) Prediction of the squirmer model.

Part II

Microswimmers in the Ocean

Many phytoplankton species, inhabiting lakes and oceans, are motile, an ability that allows them to migrate vertically in the water column to better exploit light, which is available near the surface, and to search for nutrients, which are typically more plentiful at depth. While migrating they must contend with the background fluid motion driven by waves, currents, and turbulence. As a primary producer of biomass in aquatic ecosystems, phytoplankton supports the aquatic food web and sequesters carbon. Thus, geophysical processes that affect the vertical migration and spatial distribution of phytoplankton are fundamental to aquatic ecology and biogeochemistry. The oceans cover approximately 71% of the Earth's surface and host an extraordinary diversity of organisms, ranging from microscopic algae (phytoplankton) to large marine mammals [21]. phytoplankton is particularly significant because, despite its small size, it constitutes a substantial portion of marine biomass and is essential for oxygen production and the carbon cycle. This imbalance is due not only to the difference in size but also to the oceans' greater efficiency in recycling nutrients and supporting more complex food webs. Additionally, oceans play a crucial role in atmospheric carbon sequestration through phytoplankton, a process that is less significant in lakes.

The motion of phytoplankton is significantly influenced by the surrounding flow field. The total velocity acting on the organism results from the superposition of its self-propulsion and the advecting velocity field. Furthermore, the swimming direction is modified by flow gradients according to Jeffery's equation (1.14), which accounts for the organism's shape. This coupling between swimming, advection, and body rotations has been studied in different contexts and shown to affect the spatial distributions of microswimmers and alter their vertical migration. In isotropic turbulence, microswimmers cluster and align nematically with fluid vorticity [22, 23]. These results were extended, showing that the swimming direction also aligns in a polar way with fluid velocity due to correlations between the velocity field and velocity gradients along microswimmer trajectories, combined with swimming which breaks the fore-aft symmetry of relative motion with respect to the flow [24, 25]. Microswimmers also show interesting spatial distributions in cellular flows [26, 27, 28] and isolated vortices [29, 30, 31, 32, 33] and nontrivial transport effects have been studied in microchannel flows [34, 35, 36, 37, 38]. Recent extensions of this research have begun to consider active control of transport by

mechanisms such as optimal swimming strategies [39, 40, 41], biological responses to hydrodynamic cues [42, 43, 44], and mutual interactions of microswimmers in the presence of background flow [45].

Since upwards vertical migration towards well-lit waters is a common goal, many phytoplanktonic microswimmers exhibit gravitaxis, i.e. they tend to orient their swimming direction against gravity, owing to a bottom-heaviness within an uneven body mass distribution. When combined with flow-induced reorientation, this produces a phenomenon known as gyrotaxis [46, 47]. Gyrotactic microswimmers display a plethora of behaviour in different flow conditions [48, 49, 50]. In turbulent flows, they form small-scale clusters, fractal distributions, and sample vertical fluid velocities in shape-dependent ways [51, 52, 53, 24, 49, 54, 55]. Gyrotaxis can also lead to trapping in high shear [56, 57, 50], which has been proposed as a mechanism for the formation of 'thin phytoplankton layers' commonly observed in the field [58, 59]. When the fluid acceleration is comparable to the gravitational one, swimmers respond to the total acceleration and can cluster in high vorticity regions [52].

Chapter 3

Thin Phytoplankton layers

Recent investigation of ocean flora and fauna have revealed the occurrence of thin layers, dense aggregations of organisms, throughout the oceans. These layers, typically several centimetres to a few meters thick, can extend horizontally for kilometres (see Fig.3.1) and often appear in coastal waters where vertical density gradients reduce turbulent mixing [60, 61, 62]. Thin layers are temporally stable, persisting for hours to days, and have a great ecological relevance.

Thin phytoplankton layers are associated with elevated concentrations of organic debris (marine snow) and bacteria, which enhance zooplankton growth and provide prey densities essential for fish larvae survival. However, they can also have negative effects: many species in these layers produce toxins that disrupt feeding and increase mortality among zooplankton and fish [63].

The depths at which thin layers form are frequently correlated with strong fluid density gradients (stratification) and vertical shear. Shear plays a dual role: while it can facilitate layer formation through mechanisms like *straining* or *gyrotactic trapping*, it can also destabilize layers through turbulence, in contrast with stratification [58]. The stability of these layers is governed by the *Richardson number*, Ri, which express the ratio between stratification and shear forces:

$$Ri = \frac{g}{\rho} \frac{\frac{\partial \rho}{\partial z}}{\left(\frac{\partial u}{\partial z}\right)^2}$$

where g is the gravitational acceleration, ρ is the fluid density. As an example, when $Ri < 0.25$, the water column is expected to be unstable [64]. This prediction agrees

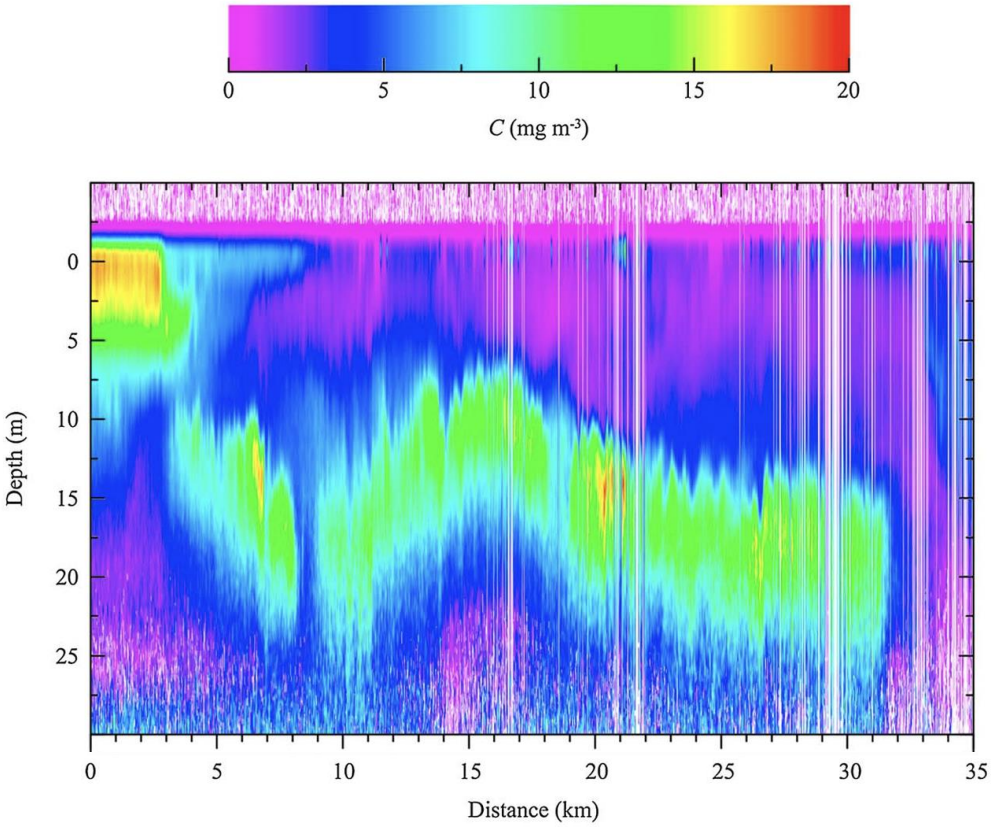

Figure 3.1: Measurements of subsurface plankton layers made in the western Arctic Ocean. Chlorophyll concentration, C, as a function of depth and position along the flight track according to the colour bar at the top. The vertical white lines denote missing data because of ice on the surface. Image from [62]

with observations that found no layers when $Ri < 0.23$, likely because of mixing due to turbulence [60].

Thin layers are ruled by a variety of processes, both abiotic and biological [58]. Using figure 3.2 as reference let's give a brief overview on these mechanisms:

1. Straining: horizontal heterogeneities in phytoplankton concentration are stretched into thin layers due to differential advection at different depths, see Fig. 3.2(a).

2. Motility: directed swimming behaviour enables phytoplankton to aggregate at optimal depths guided by light or nutrient gradients, see Fig. 3.2(b).

3. Buoyancy: non-motile cells with densities distinct from surrounding water accumulate at their neutral buoyancy depth, see Fig. 3.2(c).

4. Gyrotactic Trapping: vertical migrations of motile phytoplankton are suppressed in regions of high fluid shear, trapping cells at specific depths in thin layers, see Fig. 3.2(d).

5. Growth Enhancements: optimal mid-depth conditions for light and nutrient availability can increase growth rates, producing localized thin layers, see Fig. 3.2(e).

6. Intrusions: high-concentration phytoplankton waters transported into adjacent low-concentration regions form layers through physical processes, see Fig. 3.2(f).

These diverse mechanisms illustrate the complexity of thin layer dynamics, where interactions between physical fluid properties and biological behaviors play a central role.

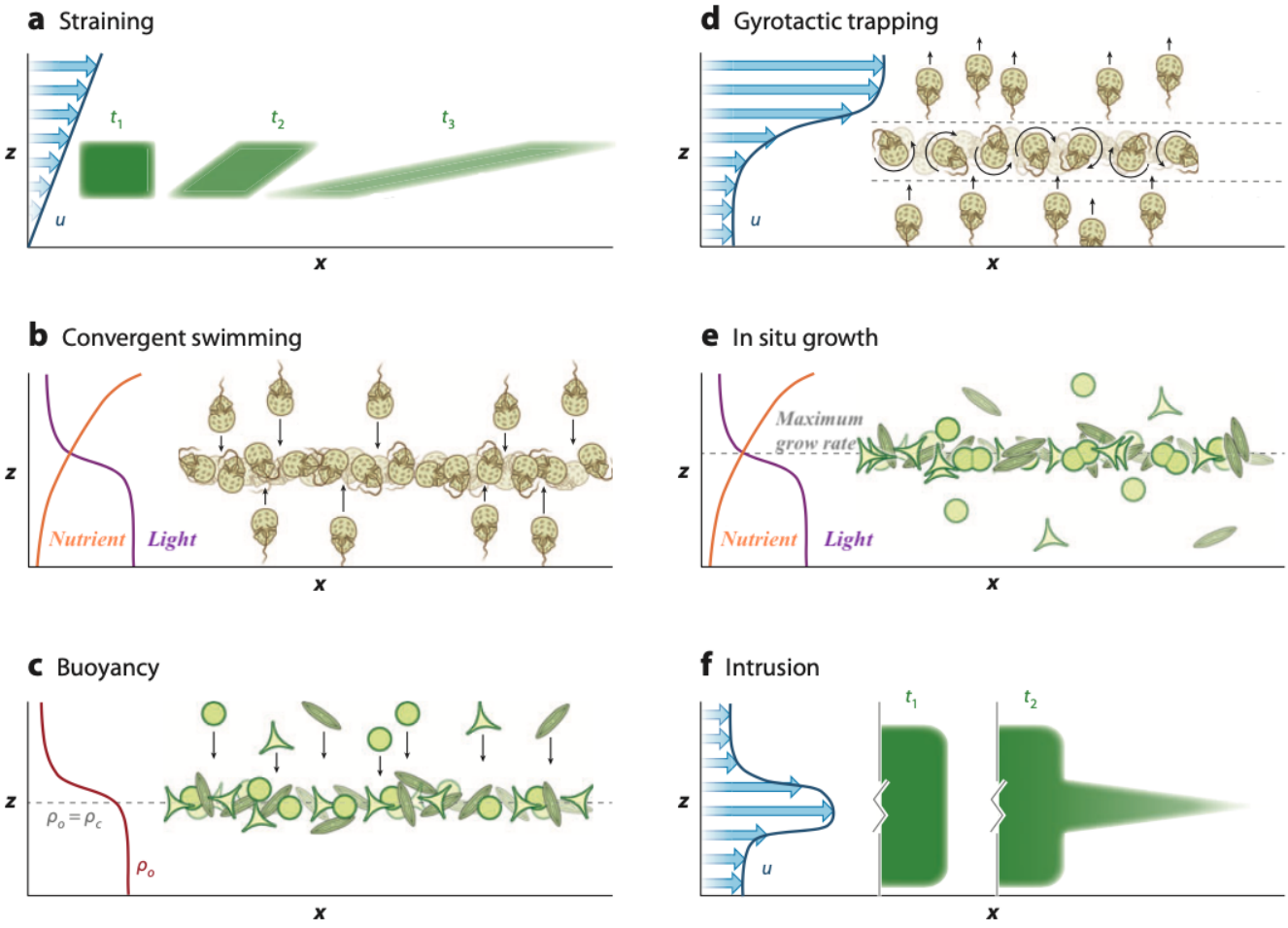

Figure 3.2: Diverse mechanisms can drive the formation of thin phytoplankton layers. For descriptions see the text. Image from [58]

Chapter 4

Gyrotaxis in Chlamydomonas reinhardtii

The ability to navigate in response to physical stimuli is known as taxis, with specific forms including phototaxis (light), chemotaxis (chemical gradients), gravitaxis (gravity), and rheotaxis (flow fields). Phytoplankton motility, combined with ambient hydrodynamic conditions, can improve the formation of thin layers. One mechanism which has been proposed is *gyrotactic trapping*, wherein hydrodynamic shear disturbs the vertical migration of motile cells. When cells encounter regions with a sufficiently intense shear rate, they experience tumbling induced by the flow, confining them to specific depths. *Gyrotaxis* is a combination of fluid velocity gradients effects and *gravitaxis* which is the capability of some cells to exerts directional movement in response to gravity. Gravitaxis can result from a purely physical mechanism: an example is given by *Chlamydomonas reinhardtii* with a centre of mass that is shifted to one end of the organism and produce a natural buoyant torque as shown in figure 4.1(a) [65].

Chlamydomonas reinhardtii is a unicellular green alga. It is widely used as a model organism in various fields of biological research, including photosynthesis, flagellar motility, and cellular responses to environmental stimuli. This microorganism has a simple cellular structure, featuring two anterior flagella that enable motility, a single large chloroplast for photosynthetic activity, and a well-defined cell wall. Its motility is primarily driven by the coordinated beating of its two anterior flagella, which generate a breaststroke-like motion (see Fig. 2.6(c)).

As shown in Figure 4.1(b), *C. reinhardtii* exhibits a particular internal distribution due to the posterior location of relatively heavy organelles, such as the chloroplast. This results in the formation of a ”heavy bottom particle” that is subjected to gravitational torque [46].

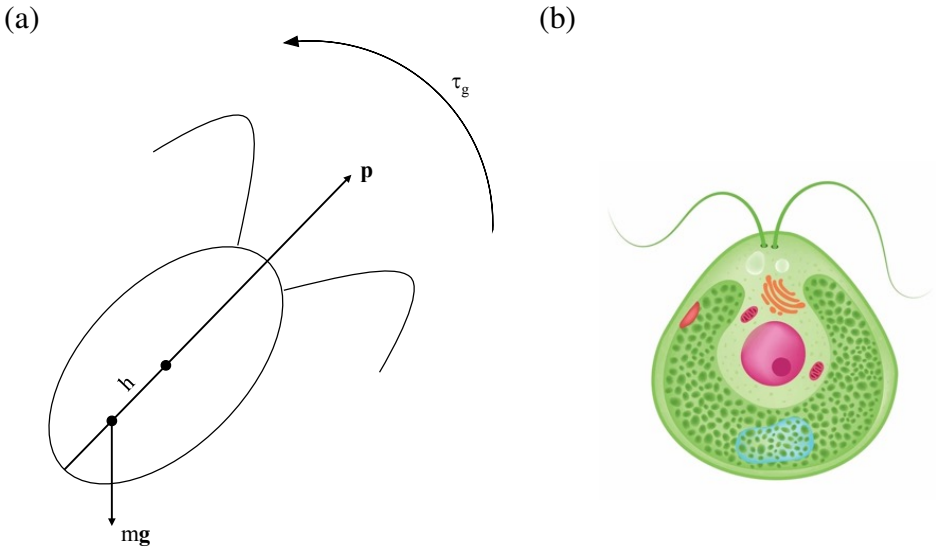

Figure 4.1: (a) Rotational torque exerted by gravity. The weight force is applied in the shifted centre of mass and the buoyancy one is in the geometric centre of the cell. The coupling will produce a rotation with respect to the geometric centre until the vertical alignment is reached. (b) Schematic representation of the internal distribution of organelles in *Chlamydomonas reinhardtii*. Notably, the chloroplast is predominantly located in the posterior region of the cell.

Let us briefly introduce the mathematical formulation of this phenomenon, which will be extensively used later for theoretical analysis.

The torque due to gravity is given by

$$\boldsymbol{\tau}_g = mgh(\mathbf{p} \times \mathbf{k}) \tag{4.1}$$

where $\mathbf{p}$ is the orientation unit vector, $\mathbf{k}$ is the vertical unit vector, mg is the weight force magnitude, and h is the displacement of the centre of mass relative to the geometric centre of the cell. For simplicity, we consider a spherical cell with radius R. The viscous torque opposing the gravitational torque is given by:

$$\boldsymbol{\tau}_\mu = 8\pi\mu R^3\boldsymbol{\omega}, \tag{4.2}$$

where μ is the dynamic viscosity and $\boldsymbol{\omega}$ is the angular velocity [1]. In the steady state, the sum of these two torques is zero, leading to

$$\boldsymbol{\tau}_g = \boldsymbol{\tau}_\mu \quad \Rightarrow \quad \boldsymbol{\omega} = 2B(\mathbf{p} \times \mathbf{k}), \tag{4.3}$$

where $B = \frac{4\pi R^3 \mu}{mgh}$ has the dimension of time [47].

The rotation induces a time variation of the orientation given by

$$\dot{\mathbf{p}} = \boldsymbol{\omega} \times \mathbf{p} = 2B(\mathbf{p} \times \mathbf{k}) \times \mathbf{p}. \tag{4.4}$$

Using the vector identity $\mathbf{a} \times (\mathbf{b} \times \mathbf{c}) = (\mathbf{a} \cdot \mathbf{c})\mathbf{b} - (\mathbf{a} \cdot \mathbf{b})\mathbf{c}$ and the fact that $\mathbf{p}$ is a unit vector (i.e., $\mathbf{p} \cdot \mathbf{p} = 1$), we obtain

$$\dot{\mathbf{p}} = \frac{1}{2B} \left[\mathbf{k} - (\mathbf{p} \cdot \mathbf{k})\mathbf{p}\right]. \tag{4.5}$$

The right-hand side introduces an alignment to the vertical direction when $\mathbf{p}$ is not parallel to $\mathbf{k}$, and it vanishes when the two vectors are parallel. Furthermore, it is important to note that B governs the time scale of vertical alignment and is derived for a spherical particle. However, it can be shown that eq. (4.5) also holds for non-spherical particles, with

$$B = \frac{4\pi R^3 \mu \alpha_\perp}{mgh}, \tag{4.6}$$

where $\alpha_\perp$ represents the resistance to cell rotation about axes perpendicular to $\mathbf{p}$ and it could be computed with geometrical considerations [47, 46, 66].

Chapter 5

Ocean dynamics: Surface Gravity Waves

Ocean waves directly influence the distribution and dynamics of marine biomass. Waves contribute to the mixing of surface ocean layers, promoting the upward transport of nutrients from deeper waters to the surface, where phytoplankton can utilize them for photosynthesis. Turbulence generated by waves also impacts the spatial distribution of marine organisms, promoting the aggregation of species in specific habitats [67].

There are many types of waves commonly encountered in fluid mechanics such as surface waves and internal waves. These are generated by oscillations, impulses, or pressure changes that break a static equilibrium. Such perturbations can create wave motion when coupled with restoring forces or pressure imbalances that allow oscillation of the material, in an attempt to return the system to the equilibrium [68]. This chapter focuses on the study of surface waves, with particular attention to the role of gravity as the restoring force, from which the term *gravity waves*.

The simplest and most common gravity waves observed in nature are those that form at the interface between two fluids with different densities, such as water and air. These involve the motion of fluid particles both perpendicular and longitudinal with respect to the propagation direction. In this analysis, Coriolis forces will be neglected due to the small scales considered, and the wave amplitude will be assumed small enough to treat the problem as linear [68].

In bidimensional coordinate, where x represents the horizontal axis and z the vertical

axis, a monochromatic sinusoidal wave is described as follows:

$$\eta(x,t) = a\cos(kx - \omega t) \tag{5.1}$$

where η is the elevation of the fluid surface relative to equilibrium, a represents the wave amplitude, $k = 2\pi/\lambda$ is the wavenumber, λ is the wavelength, $\omega = 2\pi f$, given f as the frequency, is the angular frequency (see Fig.5.1).

5.1 Linear Theory

The fundamental relations for gravity waves can be derived starting from the equations for an ideal fluid. Consider the action of wind on the free surface between two fluids of different densities, for example, air and water. When a fluid element, initially at rest, is subjected to a disturbance, gravity tends to restore equilibrium. This generates the first wave, which begins to propagate in the same direction as the wind. The continued action of the wind can create a train of waves propagating in the same direction [69].

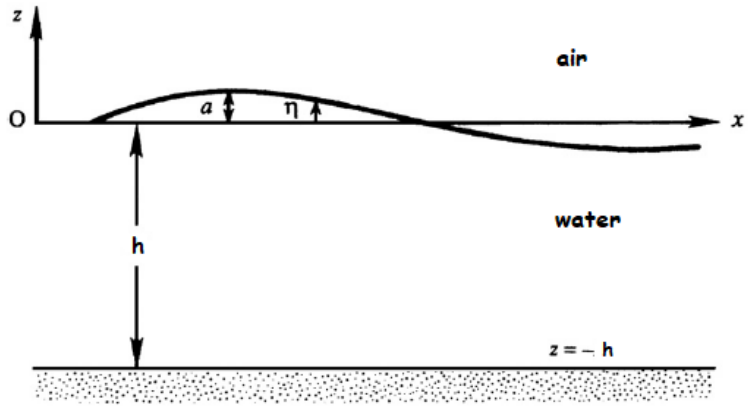

Figure 5.1: Diagram of a gravity wave on a fluid layer of depth h. The quantity η represents the elevation of the fluid surface relative to the equilibrium condition $z = 0$. Image from [68].

Referring to figure 5.1, let the seabed depth h be constant. Small amplitude waves will be considered: thus, we assume $a/h \ll 1$.

The mathematical-physical study of this type of phenomenon is generally very complex, so it is convenient to make some additional assumptions.

We assume that surface tension, which could act as a restoring force, is negligible, as it is estimated to be relevant only for $\lambda < 5$ cm [68].

The fluid is also assumed to be incompressible, thus with a constant density $\rho = const.$ Due to this approximation, the continuity equation describes a solenoidal velocity field:

$$\frac{d\rho}{dt} + \nabla \cdot (\rho \mathbf{u}) \quad \Rightarrow \quad \nabla \cdot \mathbf{u} = 0 \tag{5.2}$$

where $\mathbf{u} = (u, v, w)$ is the velocity field [69].

We further assume the fluid viscosity to be zero, $\mu = 0$. While this condition is typically unrealistic, it applies when the water is sufficiently deep. Only fluid portions near the bottom experience friction with the seabed. The upper layers, in contrast, are unaffected, making it reasonable to consider the fluid inviscid [68]. Finally, we assume the fluid to be irrotational: $\nabla \times \mathbf{u} = 0$. This last assumption allows for the definition of a velocity potential $\phi(x, y, z, t)$ such that

$$\mathbf{u} = \nabla\phi \quad \Rightarrow \quad u = \frac{\partial\phi}{\partial x}\,;\; w = \frac{\partial\phi}{\partial z}. \tag{5.3}$$

Equation (5.2) implies that

$$\nabla \cdot \mathbf{u} = \nabla \cdot \nabla\phi = \nabla^2\phi = 0 \tag{5.4}$$

This is known as the Laplace equation and is valid in all the space, both in air and in water. To solve it, boundary conditions must be applied:

- The vertical velocity at the seabed is zero:

$$w = \frac{\partial\phi}{\partial z} = 0 \quad \text{for} \quad z = -h \tag{5.5}$$

- A condition known as the *kinematic* boundary condition applies to the free surface [69]. This condition requires that individual fluid particles cannot separate from the bulk under wave motion. This implies that the particle velocity $w = \partial\phi/\partial z$ must equal the temporal variation of the free surface η:

$$\frac{D\eta}{Dt} = \frac{\partial\eta}{\partial t} + \mathbf{u} \cdot \nabla\eta = \frac{\partial\eta}{\partial t} + \nabla\phi \cdot \nabla\eta \equiv \frac{\partial\phi}{\partial z} \quad \text{for} \quad z = \eta(x, t) \tag{5.6}$$

  where the definition of the convective derivative and the velocity potential are used.

- The last condition is the *dynamic* boundary condition, which involves continuity of stress on the separating surface between the two fluids [68]. It is known that stresses are divided into shear and normal stresses or pressures [69]. The former are zero, as the fluid is inviscid, while the latter require that the water pressure equals the air pressure near the free surface. By algebraically manipulating the Navier-Stokes equation with the velocity potential [70], we get:

$$\frac{\partial \phi}{\partial t} + \frac{1}{2}(\nabla \phi)^2 + g\eta = 0 \quad \text{for} \quad z = \eta(x,t) \tag{5.7}$$

  where in (1.2) the forcing term **f** is here substitute with the gravitational acceleration **g** that is always along vertical direction.

The Cauchy problem for the Laplace equation is obtained:

$$\begin{cases} \nabla^2 \phi = 0 & for - h \leq z \leq \eta(x,t) \\ \dfrac{\partial \phi}{\partial z} = 0 & for \quad z = -h \\ \dfrac{\partial \eta}{\partial t} + \nabla \phi \cdot \nabla \eta = \dfrac{\partial \phi}{\partial z} & for \quad z = \eta(x,t) \\ \dfrac{\partial \phi}{\partial t} + \dfrac{1}{2}(\nabla \phi)^2 + g\eta = 0 & for \quad z = \eta(x,t). \end{cases} \tag{5.8}$$

A useful strategy for the study of the problem is to introduce a series of dimensionless parameters [71]. Without going into the details, two particularly relevant parameters can be distinguished:

- The *steepness* parameter, defined as the product of the wave amplitude and wavenumber: $\alpha = ak$. This parameter estimates the steepness of the wave profile. Algebraically the steepness multiplies the nonlinear term of the equation: to achieve a linear approximation of the system, it is necessary to minimize steepness. The most effective way to do this is by reducing wave amplitude.

- The parameter kh, called the shallow-water parameter which estimates the ratio between depth and wavelength: $kh \to \infty$ refers *deep water* and to the contrary $kh \to 0$ refers to *shallow water*.

The aim is to solve the Cauchy problem in (5.8) to obtain an analytical expression for the potential ϕ and compute the eulerian velocity field by solving (5.3). The full theoretical derivation is outside of the scope of this work (for further detail see [68, 69, 70, 71]). The velocity potential then becomes:

$$\phi = \frac{a\omega}{k}\frac{\cosh(k(z+h))}{\sinh(kh)}\sin(kx-\omega t) \tag{5.9}$$

from which the fluid velocity components are found as:

$$u = a\omega\frac{\cosh(k(z+h))}{\sinh(kh)}\cos(kx-\omega t) \tag{5.10}$$

$$w = a\omega\frac{\sinh(k(z+h))}{\sinh(kh)}\sin(kx-\omega t). \tag{5.11}$$

This results are applicable for any value of kh. However, interesting simplifications are provided for deep water $kh \to \infty$. The water depth on a typical continental shelf is around $100m$ and in the open ocean it is $4km$. Thus, the dominant wind waves in the ocean act as deep-water waves and do not feel the effects of the ocean bottom until they arrive near a coastline [68]. In the deep-water limit ($kh \to \infty$) the first term of the velocity field could be rewritten:

$$\frac{\cosh(k(z+h))}{\sinh(kh)} \approx \frac{\sinh(k(z+h))}{\sinh(kh)} \approx e^{kz} \tag{5.12}$$

so the fluid velocity components for deep-water waves are:

$$u = a\omega e^{kz}\cos(kx-\omega t) \quad \text{and} \quad w = a\omega e^{kz}\sin(kx-\omega t). \tag{5.13}$$

5.2 Particle Transport: the Stokes drift

Another interesting feature of linear surface waves (i.e. small amplitude approximation) is the fact that they are able to produce a net transport effect on free particles. Evidence of this phenomenon can be observed along coastlines after a storm, where accumulations of organic and inorganic material transported by the strong waves generated by the wind can be found. To focus on what happens when a linear surface wave passes, consider the fluid element that follows a path

$$\mathbf{x}_p(t) = x_p(t)\,\mathbf{e}_x + z_p(t)\,\mathbf{e}_z,$$

where $\mathbf{e}_x$ and $\mathbf{e}_z$ are directional unit vectors. The path-line equations for this fluid element are described as follows:

$$\frac{dx_p(t)}{dt} = u(x_p, z_p, t) = a\omega e^{kz_p} \cos(kx_p - \omega t), \tag{5.14}$$

$$\frac{dz_p(t)}{dt} = w(x_p, z_p, t) = a\omega e^{kz_p} \sin(kx_p - \omega t). \tag{5.15}$$

The particle position could be described in a Lagrangian framework setting the follow decomposition:

$$x_p(t) = x_0 + \xi(t), \quad z_p(t) = z_0 + \zeta(t),$$

where (x_0, z_0) is the average fluid element location and the element excursion vector (ξ, ζ) (see Fig.5.2(a)) is assumed to be small compared to the wavelength. This allows for a Taylor expansion of the r.h.s:

$$\frac{dx_p(t)}{dt} = u(x_p, z_p, t) = u(x_0, z_0, t) + \xi \left(\frac{\partial u}{\partial x}\right)_{x_0,z_0} + \zeta \left(\frac{\partial u}{\partial z}\right)_{x_0,z_0} + \ldots, \tag{5.16}$$

$$\frac{dz_p(t)}{dt} = w(x_p, z_p, t) = w(x_0, z_0, t) + \xi \left(\frac{\partial w}{\partial x}\right)_{x_0,z_0} + \zeta \left(\frac{\partial w}{\partial z}\right)_{x_0,z_0} + \ldots \tag{5.17}$$

Thus, the linearized versions are obtained by evaluating the limit $\xi \to 0$ and $\zeta \to 0$, if we assume a small amplitude, this implies small fluctuations of the particle with respect to (x_0, z_0):

$$\frac{d\xi}{dt} \equiv a\omega e^{kz_0} \cos(kx_0 - \omega t),$$

$$\frac{d\zeta}{dt} \equiv a\omega e^{kz_0} \sin(kx_0 - \omega t),$$

where x_0 and z_0 have been assumed independent of time. The two equations are easily integrated:

$$\xi = -ae^{kz_0} \sin(kx_0 - \omega t),$$

$$\zeta = ae^{kz_0} \cos(kx_0 - \omega t). \tag{5.18}$$

This linearization is valid when the velocity of the fluid element along its path is nearly equal to the fluid velocity at (x_0, z_0) at that instant. Here we note that $\xi(t)$ and $\zeta(t)$ are entirely oscillatory and describe a closed circular orbit. When finite amplitude waves are present and the limit for small $\xi(t)$ and $\zeta(t)$ is no longer valid, fluid particles do not trace closed orbits, but undergo a slow drift in the direction of wave propagation. This

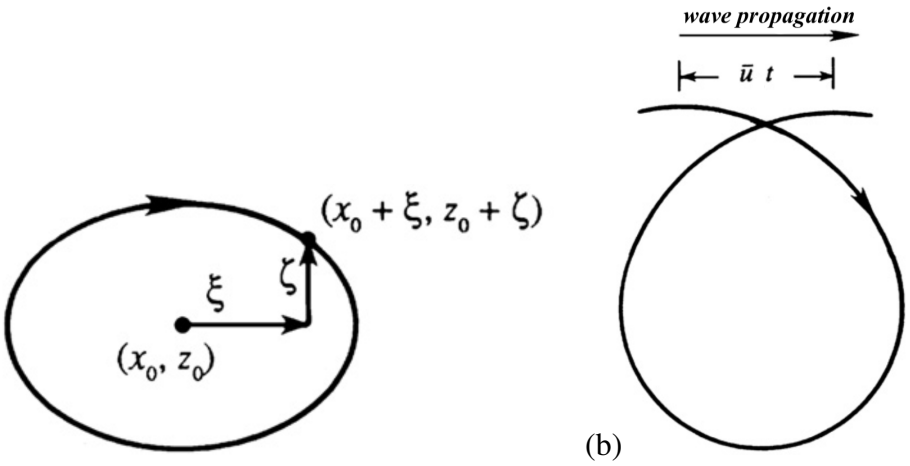

Figure 5.2: (a) The average position of the particle is (x_0, z_0), and ξ and ζ are small time-dependent displacements in the horizontal and vertical directions, respectively. (b) The Stokes drift. The drift velocity $\bar{u}$ is a finite-amplitude effect and occurs because near-surface fluid particle paths are no longer closed orbits. The mean position of an initially vertical line of fluid particles extending downward from the liquid surface will increasingly bend in the direction of wave propagation with in- creasing time.

phenomenon is called Stokes drift. It is finite-amplitude effect that causes fluid particle orbits to take a shape like that shown in figure 5.2(b). The mean velocity of a fluid particle is therefore not zero, although the mean velocity at a fixed point in space must be zero if the wave motion is periodic. The drift occurs because the particle moves forward faster when at the top of its trajectory than it does backward when at the bottom of its trajectory (see eq. (5.13)). To find an expression for the Stokes drift, we start from the path-line equations (5.16) taking into account the two terms in ξ and ζ:

$$\begin{aligned}\frac{dx_p(t)}{dt} &= u(x_0, z_0, t) + a^2\omega k e^{-2kz_0}\sin^2(kx_0 - \omega t) + a^2\omega k e^{-2kz_0}\cos^2(kx_0 - \omega t) \\ &= u(x_0, z_0, t) + a^2\omega k e^{-2kz_0} \qquad (5.19)\end{aligned}$$

in which the last two terms come from eq. (5.18) and (5.13). The Stokes drift is the time average of (5.19). However, the time average of $u(x_0, z_0, t)$ is zero. Thus, for a generic quote, the Stokes drift is given by :

$$\bar{u} = a^2\omega k e^{-2kz}.$$

Its surface value is $a^2\omega k$, and the vertical decay rate is twice that for the fluid velocity

components. Therefore, the Stokes drift is confined very close to the sea surface and it is strongly affected by the amplitude and thus by the non linearity.

Chapter 6

Microswimmer trapping in surface waves with shear

Here, we explore the behavior of microswimmers in ocean, highlighting effects that are crucial for light-seeking phytoplankton [72, 73, 74]. This parallels recent works on passive particle transport in surface gravity waves [75, 76, 77, 78, 79]. In particular, the aim of this section is to extend previous work in [74], which examined how microswimmers interact with a wavy background flow, to also consider gyrotactic and settling microswimmers within a more general flow configuration that includes a wind-driven shear superimposed on surface waves, a situation typically encountered in oceans [80]. The multiscale approach is used to analyse the most general system of negatively buoyant non-spherical gyrotactic swimmers in surface gravity waves with a wind-driven shear, followed by specific sub-cases that neglect certain aspects. In general, both gyrotaxis and shear introduce new orientation effects that change the topology of microswimmer trajectories. Specifically, there are particular trajectories in which microswimmers are confined to a particular depth. By considering stability and observability of the trapping behaviour, we show how the depth at which microswimmers are trapped depends on the balance of different effects. Overall, these trapping features of the system present new mechanisms that may contribute to the formation of thin phytoplankton layers in the ocean [58].

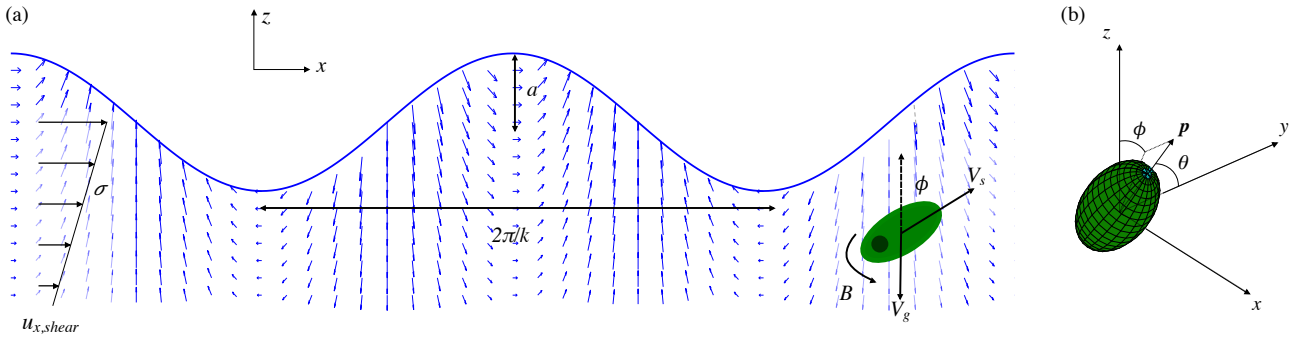

Figure 6.1: Definition sketch of the problem. (a) A prolate gyrotactic microswimmer swims with velocity V_s along its symmetry axis; settles with velocity V_g; and re-orients against gravity with characteristic timescale B. It interacts with a flow field induced by surface waves of amplitude a and wavenumber k, superposed on a linear shear with shear rate σ. (b) Definition of the orientation vector $\mathbf{p}$ and associated angles ϕ and θ.

6.1 Mathematical model and multiple-scale analysis

Let's consider axisymmetric ellipsoidal microswimmers whose dynamics of position and orientation are described by (see figure 6.1):

$$\dot{\mathbf{x}} = \mathbf{u} + V_s\mathbf{p} - V_g\mathbf{k} \tag{6.1a}$$

$$\dot{\mathbf{p}} = \boldsymbol{\Omega}\,\mathbf{p} + \lambda[\mathbf{S}\,\mathbf{p} - (\mathbf{p}^T\mathbf{S}\,\mathbf{p})\mathbf{p}] + \frac{1}{2B}[\mathbf{k} - (\mathbf{k}\cdot\mathbf{p})\mathbf{p}]. \tag{6.1b}$$

In the first equation, which describes the microswimmer's velocity, there are three terms on the right-hand side: fluid transport, swimming, and settling, respectively. The microswimmer moves with a constant swimming velocity V_s in the direction of its symmetry axis $\mathbf{p}$. The effect of negative buoyancy is taken into account by adding a constant vertical sinking velocity $\mathbf{v}_g = -V_g\mathbf{k}$, with $\mathbf{k}$ being the unit vector in the vertical (z) direction. For the main body of this work, we assume this simplified form of the settling velocity, neglecting the dependency of the settling velocity vector on the microswimmer orientation (see Appendix A.2 for details). In the second equation, the first term is the Jeffery equation and describes the evolution of the particle's orientation (as explained in section 1.3) and the second one is the gyrotactic term describing bottom-heavy microorganisms [47, 49], which, in the absence of a flow, orient themselves against gravity with the characteristic

re-orientation time B (see section 4 for details). For the sake of brevity and because it captures the main phenomenology, only 2D dynamics is considered. Thus the microswimmer axis $\mathbf{p}$ is restricted to the x-z plane and orientation is denoted by the angle measured relative to the vertical direction ($p_x = \sin\phi\,;\ p_z = \cos\phi$) as shown in figure 6.1.

The fluid velocity field here considered is a monochromatic surface gravity wave travelling in the x direction. Under the assumption of small wave amplitudes and deep water, the velocity field, which is incompressible and irrotational (i.e. $\mathbf{\Omega} = 0$), is a solution of the Euler equations and given by

$$u_x = a\omega e^{kz}\cos(kx - \omega t) \tag{6.2a}$$

$$u_z = a\omega e^{kz}\sin(kx - \omega t), \tag{6.2b}$$

where $z \leq 0$ is the vertical domain (where $z = 0$ denotes the average surface position), a is the wave amplitude, k is the wavenumber, and $\omega = \sqrt{gk}$ is the angular frequency.

As a generalization of the simple monochromatic gravity wave, we introduce an additional shear velocity that represents the effect of wind on the surface velocity and, consequently, on the underlying fluid layers [80]. A simple model for the shear is given by an exponentially decaying velocity $u_{x,\text{shear}} = u_0\exp(z/\beta)$ where β represents a characteristic depth. In order to simplify the analytical treatment we linearize the shear profile (for $z \geq -\beta$) as

$$u_{x,\text{shear}} = \sigma(\beta + z), \tag{6.3}$$

with $\sigma = u_0/\beta$ being the shear rate.

In what follows all lengths and times are made dimensionless using k and ω, respectively. The resulting non-dimensional parameters are the *wave steepness* $\alpha = ak$, the *dimensionless shear rate* $\sigma' = \sigma/\omega$, the *dimensionless shear depth* $\beta' = \beta k$, the *swimming number* $\upsilon = kV_s/\omega$, the *settling number* $\upsilon_g = V_g k/\omega$ and the *stability number* $\Psi = B\omega$. Hereafter, the primes are removed for the sake of notational simplicity. Equation (6.1) takes the 2D dimensionless form

$$\dot{x} = \alpha e^z\cos(x - t) + \upsilon\sin\phi + \sigma(\beta + z) \tag{6.4a}$$

$$\dot{z} = \alpha e^z\sin(x - t) + \upsilon\cos\phi - \upsilon_g \tag{6.4b}$$

$$\dot{\phi} = \lambda\alpha e^z\cos(x - t + 2\phi) - \frac{1}{2\Psi}\sin\phi + \frac{\sigma}{2}(1 + \lambda\cos 2\phi). \tag{6.4c}$$

The range of validity of the model in equation (6.4) is $-\beta \leq z \leq 0$, where the lower limit is determined by the linearization of the shear and the upper limit is determined by the requirement that the swimmer remains below the average surface position. In numerical simulations of (6.4), trajectories are stopped when z is outside the range $[-\beta, 0]$.

The dynamics of swimmers is characterized by fast oscillations at the surface wave frequency superposed with a slower trend at a longer timescale. Following the approach of [74], we implement a multiple timescale expansion to remove the fast oscillations by introducing the slow timescale $T = \epsilon^2 t$. The magnitude of the parameters are assumed to scale as follows:

$$\alpha \to \epsilon\alpha; \quad \upsilon \to \epsilon^2\upsilon; \quad \Psi^{-1} \to \epsilon^2\,\Psi^{-1}; \quad \upsilon_g \to \epsilon^2\upsilon_g; \quad \sigma \to \epsilon^2\sigma. \tag{6.5}$$

From the multiple timescale expansion [81], it is possible to obtain the following differential equations for the T-dependent slow variables (represented by capital letters) as a solvability condition at order ϵ^2 (see Appendix A.1 for details):

$$\partial_T X = \alpha^2 e^{2Z} + \upsilon \sin\Phi + \sigma(\beta + Z) \tag{6.6a}$$

$$\partial_T Z = \upsilon\cos\Phi - \upsilon_g \tag{6.6b}$$

$$\partial_T \Phi = \lambda\alpha^2 e^{2Z}[\cos(2\Phi) + \lambda] - \frac{1}{2\Psi}\sin\Phi + \frac{\sigma}{2}(1 + \lambda\cos(2\Phi)). \tag{6.6c}$$

The first equation in (6.6) describes the horizontal motion and the first term represents the Stokes drift [82, 83] which is always positive (in the direction of the waves) and can be enhanced or reduced by the other terms, as will be discussed in the following.

Remarkably, the dynamics of Z and Φ is independent of X, so we can study the two-dimensional system (Z, Φ) separately. In the plane (Z, Φ) we find two fixed points (Z^+, Φ^+) and (Z^-, Φ^-) given by

$$\Phi^\pm = \pm\arccos(r) \tag{6.7}$$

where $r = \upsilon_g/\upsilon \geq 0$ is the ratio of the swimming speed to the sinking velocity, and

$$Z^\pm = \tfrac{1}{2}\ln\left[\frac{\pm\sqrt{1-r^2} - \Psi\sigma\left(1 + \lambda\left(2r^2 - 1\right)\right)}{2\Psi\lambda\alpha^2\left(\lambda + 2r^2 - 1\right)}\right]. \tag{6.8}$$

The existence of the fixed points requires $r \leq 1$. Indeed the physical interpretation is that if $r > 1$ (i.e. $\upsilon_g > \upsilon$) the swimmers sink and no fixed point can be reached. Depending

on the stability of the corresponding solution, the existence of a fixed point can result in an effective trapping of some swimmer trajectories within a finite depth from the surface. This is the main finding of this work and it will be discussed in detail in the following sections.

6.2 Analysis of the fixed points and their stability

To clarify the results, this section provides a detailed study of the existence and nature of the fixed points in the (Z, Φ) space with three different limits in which one or more ingredients of the model is disregarded.

6.2.1 Pure Gyrotaxis

Let's start by considering the case of a neutrally buoyant ($v_s = 0$, i.e. $r = 0$), gyrotactic swimmer ($\Psi < +\infty$) in the absence of shear ($\sigma = 0$). In this limit equations (6.6) simplify to

$$\partial_T X = \alpha^2 e^{2Z} + v \sin\Phi \tag{6.9a}$$

$$\partial_T Z = v \cos\Phi \tag{6.9b}$$

$$\partial_T \Phi = \lambda\alpha^2 e^{2Z}[\cos(2\Phi) + \lambda] - \frac{1}{2\Psi}\sin\Phi. \tag{6.9c}$$

The fixed points (6.7, 6.8) then become

$$\Phi^{\pm} = \pm\pi/2, \quad Z^{\pm} = \tfrac{1}{2}\ln\left[\frac{\pm 1}{2\Psi\lambda\alpha^2(\lambda-1)}\right], \tag{6.10}$$

and therefore we have only one real fixed point (Z^-, Φ^-). The stability analysis of this fixed point gives the eigenvalues $\eta_{1,2} = \pm i\sqrt{v/\Psi}$, meaning that the fixed point is neutrally stable. For the fixed point to be of physical relevance, i.e. to be below the water surface ($Z < 0$), the argument of the logarithm in equation (6.10) must be smaller than one, implying the observability condition

$$\Psi > \frac{1}{2\lambda(1-\lambda)\alpha^2}\,. \tag{6.11}$$

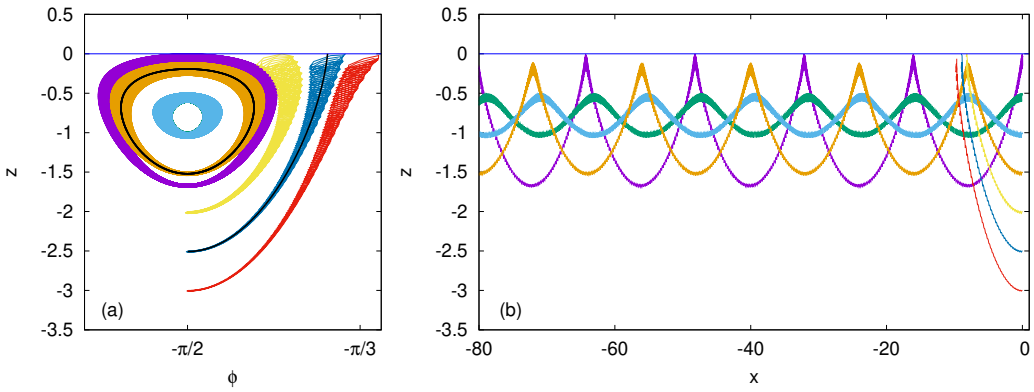

Figure 6.2: Numerical simulations for the pure gyrotactic case with $\lambda = 0.6$, $\alpha = 0.1$, $\Psi = 10^3$ and $\upsilon = 0.01$. Lines with different colours represent trajectories starting from $x = 0$ at different depths z and at a fixed initial orientation $\phi = -\pi/2$. The blue horizontal line is the average surface of the fluid. (a) Representation of the neutral fixed point ($\Phi^- = -\pi/2$, $Z^- = -0.7843$) in phase space. Black lines represent two examples of slow dynamics as average of fast oscillations. (b) Real space representation of the same trajectories. Waves propagate from left to right, while the swimmers swim in the opposite direction. The closed orbits in panel (a) correspond to swimmers trapped between two depths below the sea level.

Since $\lambda = O(1)$ and, for linear waves, $\alpha \lesssim 0.1$ the above expression requires that $\Psi = B\omega = O(10^2)$. Therefore, depending on the wave frequency, the existence of a fixed point below the water surface may require a very long gyrotactic relaxation time B. Such large values of B have been observed for chains of gyrotactic cells, see e.g. [84]. In figure 6.2 the prediction of the multiple-scale analysis is shown and it accurately predict the behavior of the full dynamics obtained by numerical simulation of the original equations (6.4) with $\lambda = 0.6$, $\alpha = 0.1$, $\Psi = 10^3$ and $\upsilon = 0.01$. Indeed, we observe a family of trajectories centred on the fixed point, the outermost of which extend roughly from the surface to a few times Z^- in depth. The orbits starting further away from the fixed point end up crossing the surface and cannot be consistently treated within our model.

Let's focus on the horizontal (X) dynamics. The first equation in (6.9) evaluated at the fixed point (6.10) gives the horizontal velocity

$$\partial_T X = \frac{1}{2\Psi\lambda(1-\lambda)} - \upsilon. \tag{6.12}$$

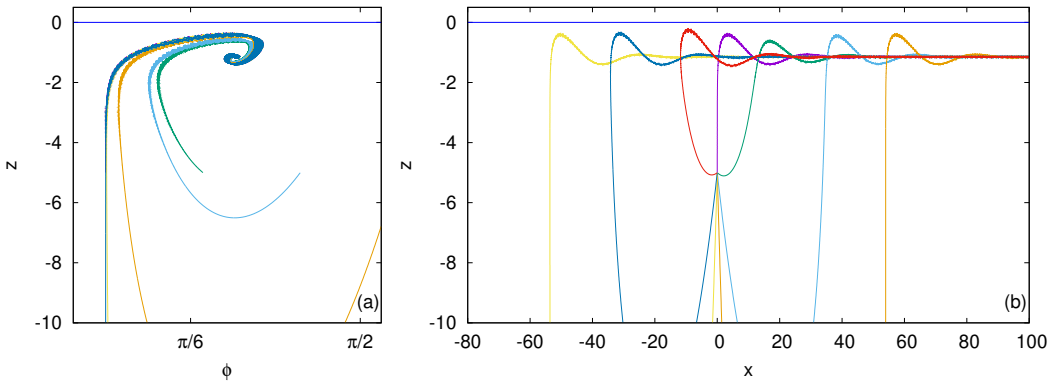

Figure 6.3: Attractive fixed point in the gyrotactic case with a settling velocity. The parameter values $\lambda = 0.6, \Psi = 10^3$, $r = 0.7$ (i.e. $v = 0.01$ and $v_g = 0.007$), and $\alpha = 0.1$ result in $Z^+ = -1.14$. Lines with different colours represent trajectories starting from $x = 0$ at a fixed depth $z = -5$ and different orientations in $\phi \in [0, 2\pi]$. All trajectories converge to each other. (a) Dynamics around the fixed point in phase space. (b) Corresponding real space representation. Both the waves' propagation and swimming are from left to right.

In general, the swimming direction (with speed v) is opposite to the Stokes drift (given by the first term in (6.12)). In the limit of large Ψ, the fixed point moves to large negative Z: the Stokes drift is negligible and the horizontal motion is dominated by the swimming term. Under the observability condition (6.11), one can show that swimming term in (6.12) dominates also when $v \geq \alpha^2$, as in the example shown in figure 6.2.

6.2.2 Gyrotaxis combined with Settling

The second discussed is the case of negatively buoyant ($v_g > 0$) gyrotactic swimmers ($\Psi < +\infty$), still in the absence of shear ($\sigma = 0$). The equations for the slow variables are still given by (6.9) with the equation for Z modified to $\partial_T Z = v \cos\Phi - v_g$, so that the fixed points become $\Phi^\pm = \pm \arccos r$ (as in (6.7)) and

$$Z^\pm = \frac{1}{2} \ln \left[\frac{\pm\sqrt{1-r^2}}{2\Psi\lambda\alpha^2(\lambda + 2r^2 - 1)} \right], \tag{6.13}$$

as easily derived from (6.8) for $\sigma = 0$. The domain of existence of the fixed points is

$$(\Phi^-, Z^-) \in \mathbb{R} \Leftrightarrow 0 < r < \sqrt{\tfrac{1}{2}(1-\lambda)} \tag{6.14a}$$

$$(\Phi^+, Z^+) \in \mathbb{R} \Leftrightarrow \sqrt{\tfrac{1}{2}(1-\lambda)} < r < 1. \tag{6.14b}$$

The eigenvalues associated to the fixed points (Φ^-, Z^-) are

$$\eta_{1,2} = -\frac{r(3-2r^2+\lambda) \pm \sqrt{r^2(3-2r^2+\lambda)^2 - 16\Psi(1-r^2)(2r^2-1+\lambda)^2}}{4\Psi(2r^2-1+\lambda)}. \tag{6.15}$$

It is easily checked that the eigenvalues always have a positive real part and therefore the fixed point (Φ^-, Z^-) is unstable. Clearly, in the limit $r = 0$ the eigenvalues become imaginary and recovers the results of the previous section 6.2.1.

The eigenvalues associated to the fixed point (Φ^+, Z^+) are still given by (6.15) but, in this case, in the domain of existence the real part of the eigenvalues is negative and therefore (Φ^+, Z^+) is stable. The observability condition (i.e. $Z^+ < 0$) is more complicated than in the previous case since it involves a combination of the parameters Ψ and r, and will be discussed in the context of numerical simulations below. Figure 6.3 shows how several trajectories converge, asymptotically oscillating around a mean depth Z^+.

As for the horizontal dynamics, once the attractive fixed point (Φ^+, Z^+) is reached, the motion is given by

$$\partial_T X = \frac{\sqrt{1-r^2}}{2\Psi\lambda\left(\lambda - 1 + 2r^2\right)} + \upsilon\sqrt{1-r^2}. \tag{6.16}$$

In the domain of existence of the fixed point, both terms in (6.16) are positive, and therefore in this case the Stokes drift is enhanced by swimming.

6.2.3 Pure Shear

The last case considered is the one with a neutrally buoyant ($\upsilon_g = 0$), non-gyrotactic swimmer ($\Psi \to \infty$) in a velocity field characterized by waves with a linear shear ($\sigma \neq 0$). From (6.6) the equations are

$$\partial_T X = \alpha^2 e^{2Z} + \upsilon \sin\Phi + \sigma(\beta + Z) \tag{6.17a}$$

$$\partial_T Z = \upsilon \cos\Phi \tag{6.17b}$$

$$\partial_T \Phi = \lambda\alpha^2 e^{2Z}[\cos(2\Phi) + \lambda] + \frac{\sigma}{2}(1 + \lambda\cos 2\Phi). \tag{6.17c}$$

The system has two fixed points, which can be obtained from (6.8) for $r = 0$ after taking the limit $\Psi \to \infty$, given by $\Phi^{\pm} = \pm\pi/2$ and

$$Z^* = \frac{1}{2}\ln\left[\frac{\sigma}{2\lambda\alpha^2}\right]. \tag{6.18}$$

The observability condition $Z^* < 0$ in the existence domain requires that

$$0 < \sigma \leq 2\lambda\alpha^2\,. \tag{6.19}$$

The stability analysis for the fixed point $(-\pi/2, Z^*)$ leads to the eigenvalues $\eta_{1,2} = \pm i\sqrt{\upsilon\sigma(1-\lambda)}$ for $(-\pi/2, Z)$, i.e. a neutral fixed point, while $(\pi/2, Z^*)$ is unstable since $\eta_{1,2} = \pm\sqrt{\upsilon\sigma(1-\lambda)}$. Thus, the dynamics in the plane (Φ, Z) is qualitatively similar to the case of pure gyrotaxis discussed in section 6.2.1, as shown in figure 6.4 (to be compared with figure 6.2). We remark that for typical values $\lambda = 0.6$ and $\alpha = 0.1$, the observability condition becomes $\sigma \leq 0.012$ which, as we will see, is a number compatible with values observed in the ocean.

The horizontal dynamics at the neutral fixed point is in this case given by

$$\partial_T X = \frac{\sigma}{2\lambda} - \upsilon + \sigma\,(\beta + Z^*) \tag{6.20}$$

with Z^* given by (6.18). The Stokes drift (first term in (6.20) is proportional to the shear. Since in the model of the shear we assume $|Z| \leq \beta$, the last term is also positive, while the swimming contribution is negative, i.e. opposite to the direction of waves and the shear. The resulting horizontal motion depends on the parameters and can be either upstream or downstream as in figure 6.4. We remark that this result is consistent with the multiple scale analysis in which υ and σ are both second order terms: their relative magnitude controls the sign of the horizontal velocity.

6.3 Discussion

The analysis in the previous sections has been carried out in dimensionless variables. The applicability of the results is now discussed in the context of realistic values for the dimensional parameters. Figure 6.5 summarizes the different cases discussed in the chapter. The wave steepness and the particle elongation are fixed respectively to $\alpha = 0.1$,

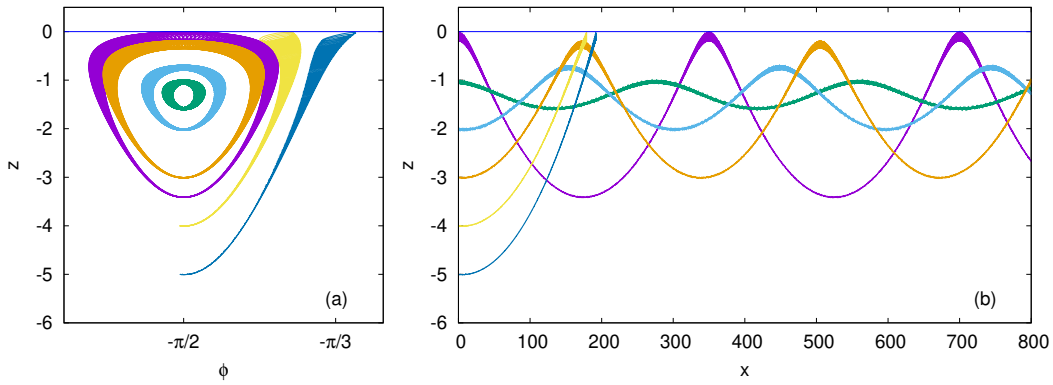

Figure 6.4: Fixed point in the case with shear only. Parameters are $\sigma = 10^{-3}$, $\beta = 100$, $\lambda = 0.6$, $\alpha = 0.1$, and $\upsilon = 0.01$, which results in $Z \simeq -1.24$. Lines with different colours represent trajectories starting from $x = 0$ at different depths with a fixed initial orientation $\phi = -\pi/2$. (a) Dynamics around the fixed point in the phase space representation. (b) Corresponding trajectories in real space. The waves' direction is from left to right. The mean velocity is left to right despite the swimmer's upstream orientation, as in this particular case transport is dominated by shear.

which is a reasonable value for linear waves as used in our model, and $\lambda = 0.6$ that is in the range of typical values for gyrotactic microorganisms [57]. All plots refer to the analytical solutions for the depth Z^* of the fixed point (stable or neutral) varying one or more parameters in the different limits discussed in section 6.2. The range of wavenumbers k is chosen to be in the range of values typical of wavelengths encountered in the ocean [85]. Recall that physically one must have $Z^* < 0$, which corresponds to the observability condition $z^* < -a$ in dimensional form with an oscillating surface.

The pure gyrotactic case is described in figure 6.5(a), where the depth of the fixed point equation (6.10) is plotted as a function of the wavenumber and the gyrotactic orientation time B. The plot shows that, for typical values of k, negative values of z^* are obtained for large values of B, outside the the typical range (of a few seconds) cited in the literature [86, 42]. For example, the case discussed in figure 6.2 with $k = 1\,\mathrm{m}^{-1}$ corresponds to $B \simeq 300\,\mathrm{s}$ and a depth of the fixed point $z^* \simeq -0.8\,\mathrm{m}$. In this case, the Stokes drift velocity in (6.12) is $O(1)\,\mathrm{cm\,s}^{-1}$, much larger than typical swimming velocities. Thus, there is no trapping behaviour for neutrally buoyant gyrotactic organisms swimming in waves without shear with realistic re-orientation times.

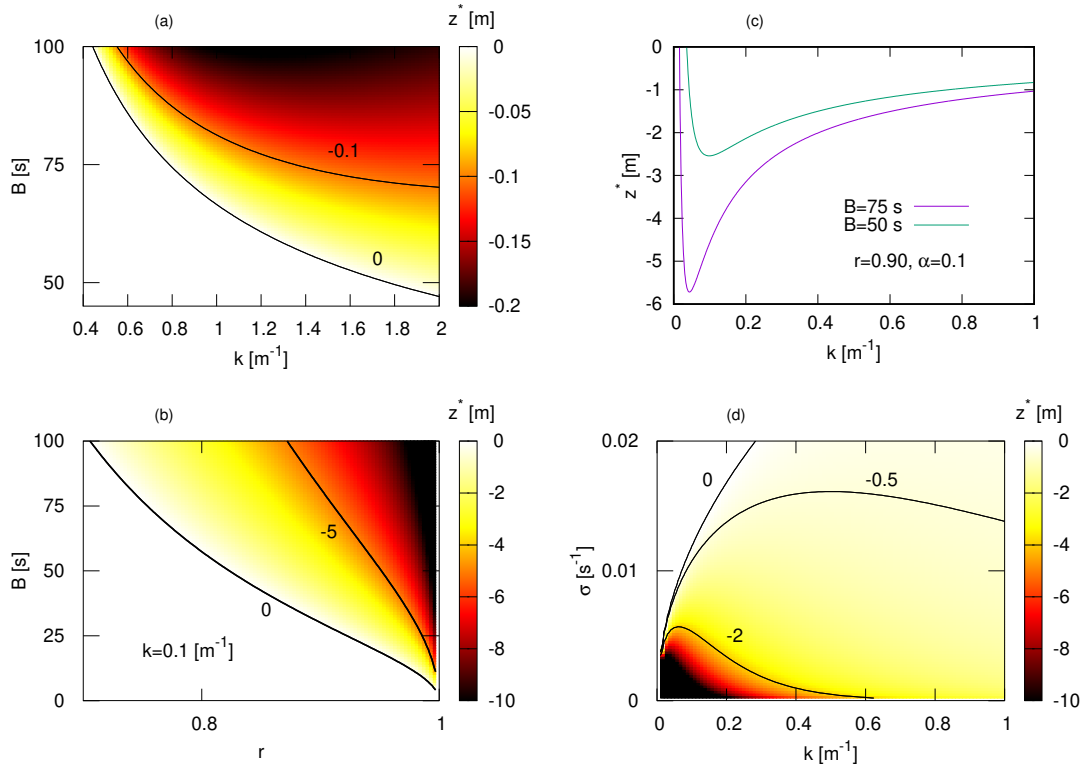

Figure 6.5: Depth of the fixed points as a function of the parameters in the different regimes for $\alpha = 0.1$ and $\lambda = 0.6$. (a) Pure gyrotactic case (Sec. 6.2.1). Negative values of z^* requires large values of B. (b) Gyrotactic and settling case (Sec. 6.2.2) with wavenumber $k = 0.1\text{m}^{-1}$. Large negative values of z^* are obtained for large values of B and r close to one. (c) Gyrotactic and settling case (as in (b)) with $r = 0.9$ as a function of k. The depth is a non-monotonic function of k with a absolute minimum (maximum depth) that is dependent on B: greater B implies deeper depth. (d) Shear case (Sec. 6.2.3) as a function of wavenumber and shear intensity.

Let's consider the case of sinking gyrotactic microswimmers. Figure 6.5(b) displays the depth z^* of the fixed point as a function of B and $r = V_g/V_s$ at fixed wavenumber $k = 0.1\ \text{m}^{-1}$. Even considering large values of B, a negative value of z^* requires $r = O(1)$, i.e. a settling velocity V_g close to the swimming speed V_s. This is not common in swimming microorganisms, since motility is often assumed to evolve as a way to escape sinking through the water column. For example, *Chlamydomonas reinhardtii* swims with speed $50-70\ \mu\text{m/s}^{-1}$ while its sedimentation speed is only $2.5\ \mu\text{m/s}^{-1}$ [86]. Figure 6.5(c) shows the depth of the fixed point as a function of k for two values of B (at fixed $r = 0.9$).

Remarkably, the position of the fixed point is non-monotonic in k and the position of the minimum value depends on the value of B.

Finally, here is explained the case of swimmers in waves with a shear, in the absence of gyrotaxis and sedimentation. Figure 6.5(d) shows the depth of the fixed point z^* as a function of the wavenumber k and the shear rate σ. The observability condition in this case requires small values of the shear rate $\sigma \lesssim 10^{-2}\mathrm{s}^{-1}$ which are common in the ocean [87]. In this case, confinement at a few meters below the surface is compatible with realistic values of the parameters. Using the parameters of figure 6.4, with a wavenumber $k = 0.2\,\mathrm{m}^{-1}$, the horizontal motion (6.20) is dominated by the shear term and the swimmer moves downstream.

Part III

A Minimal Numerical Model for an Active Swimmer

The study of motility in swimming animals and microorganisms is a captivating subject in the biological realm, covering various aspects such as feeding, reproduction and prey-predator interactions [88, 89] with potential applications to biomedicine [90]. Additionally, it extends to the field of biological-inspired intelligent navigation [91, 92]. Moreover, in recent years, a growing amount of research has focused on wet active matter [93], i.e. dense suspensions of swimmers moving in a viscous fluid where the hydrodynamic disturbances are a key mode of interaction. Consequently, the dynamics of a single swimmer becomes the focal point of numerous experimental [94, 95, 96, 97], theoretical [98, 112], and numerical investigations [99, 100, 101, 102, 103]. The overarching goal is to model the dynamics of a single swimmer in its environment and understand how the interaction of these organisms influences global behavior and the background flow field, leading to collective organized motion [104, 105, 103, 106, 107].

The modelling of microswimmer locomotion encompasses theoretical frameworks such as the waving sheet model and the squirmer model (see §2.3), as well as simplified models designed for numerical simulations. The latter focus not on the mechanisms driving locomotion, such as cilia or flagella, but rather on the effects that the motion of the swimmer induces in the surrounding fluid. These effects are formally analysed as perturbations of the velocity field, which consequently modify the flow structure around the swimmer body.

Chapter 7

Introduction to simple swimmer models

In the context of studying collective motion of microswimmers, it is important to understand how the swimmers perturb the fluid itself and influence the motion of nearby swimmers. To this end, we will not approach numerical simulations with the primer aim to resolve the boundary condition problem around an individual swimmer. Thus, we will instead shift our analysis to the far-field, assuming the swimmers' bodies as rigid and non-deformable. Such assumption allows for some analytical treatment, as shown in previous chapters, facilitating insights into the pairwise interactions. In this section, a brief overview of the models that have inspired this work will be presented.

The behaviour of a swimmer can be described by considering two opposite forces exerted on the fluid, as illustrated in paragraph 2.2. This idea can be implemented by conceptually dividing the swimmer into two halves: one responsible for propulsion and the other subjected to the no-slip condition which governs the interaction between the fluid and the swimmer's body [108]. This division is not overly abstract considering that in many organisms the locomotory apparatus is located far from the main body, as observed in sperm cells or *Chlamydomonas reinhardtii*. It is therefore a natural minimal assumption to model the swimmer using a *dumbbell model* [109, 110]. Such a minimal swimmer model, frequently found in literature, captures the leading-order far-field effects without specifying in detail the swimmer's shape or its propulsion mechanism. Each swimmer is modelled as a rigid, neutrally buoyant dumbbell composed of two beads connected by a rigid rod of fixed length. Each spherical bead is the support of a volume force: all drag on the swimmer is concentrated on the two beads and propulsion force involve only

on one of the two. Conservation of momentum is achieved applying a constant point force on one of the beads and an equal and opposite force to the surrounding fluid (see Fig.7.1(a)). In this framework, the force balance on bead 1 of each swimmer (neglecting inertia) is $\mathbf{F}_p + \mathbf{F}_c + \mathbf{F}_D = 0$ and the same for bead 2 without the propulsion. Here $\mathbf{F}_p$ is the force exerted by the flagellum on the bead and $\mathbf{F}_c$ is the force that enforces the rigid rod constrain. The drag force $\mathbf{F}_D$ is implemented via a no-slip condition. In practice the flagellum is described by a phantom particle whose propulsive contribution is applied on one of the beads along the rectilinear swimming direction.

The natural evolution of this model involves the introduction of a third bead to represent flagellum and allow for a finite body length defined by the two rods connecting the beads [111, 112]. The length of rods is kept constant using various strategies, and the position of the flagellum-bead is determined a posteriori, in the direction of the dumbbell, following the dynamics of the body-beads. In this formulation the propulsive force is applied on the third bead and the propulsion is transferred to the main body thanks to the rigidity of the rod (see Fig.7.1(b)). The introduction of a third bead increases the swimmer's degrees of freedom. It is possible to define an angle between the flagellum and the body. Indeed, the flagellum (hence the propulsion) describe an arbitrary angle with respect to the body, resulting in a curved trajectory. If the angle of the flagellum is kept constant, the resulting trajectory of an isolated bent swimmer is circular. For this reason, this configuration is commonly known in the literature as *circle swimmer* [129]. This motion is therefore planar due to the presence of a single angle in the swimmer geometry.

Furthermore, it is important to note that the number of spheres could be increased. It is possible to have a denser distribution of beads to achieve, for example, a more precise description of the interaction with the fluid [113, 114] or increase the swimmer's degrees of freedom with the introduction of more bending angles that allow non planar motion [115, 116].

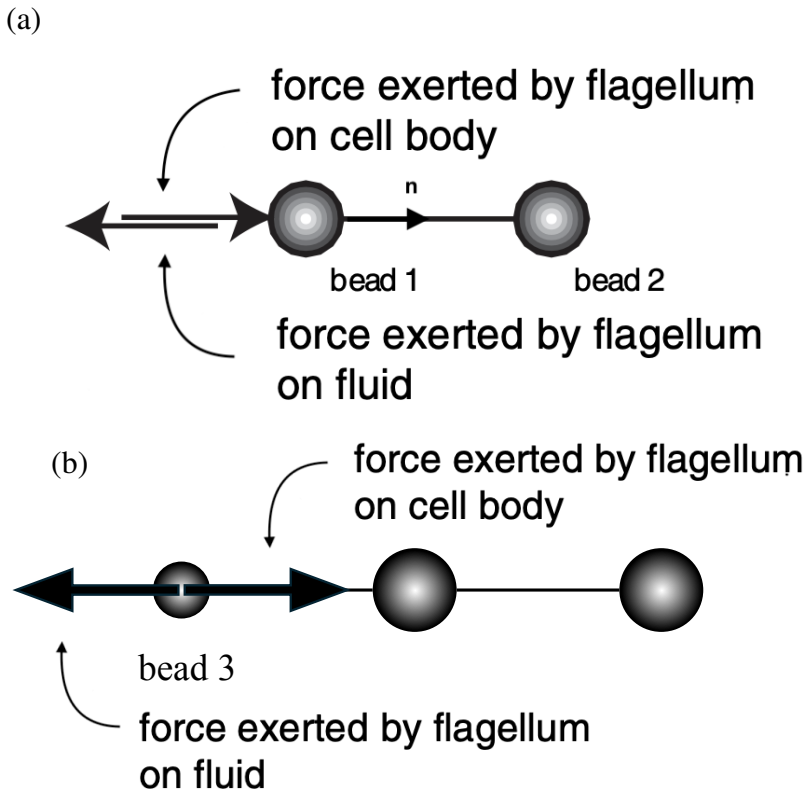

Figure 7.1: (a) Bead-rod-dumbbell model of a swimmer. The flagellum is represented by a force exerted on one of the beads of the dumbbell, and a force in the opposite direction exerted by the dumbbell on the fluid. Image from [109]. (b) 3-beads model: the flagellum is modelled with a third sphere physically separated from the body.

Chapter 8

Modelling straight and circle swimmers

This chapter aims to propose a swimmer model based on immersed boundary methods. The IB method [117], initially developed to simulate blood flows into the heart and vessels, has found applications in various biological fluid dynamics problems [118, 119, 120, 121, 122], including animal locomotion [123, 124]. In essence, the method treats the elastic material as part of the fluid: body motion is obtained by interpolating the forces due to fluid stress onto a set of points representing the surface of the immersed body, and the body feedback on the fluid is applied by using the same interpolation method. This allows the straightforward application of Navier-Stokes (NS) solvers to complex flow geometries without the constraint of a boundary-conforming grid, which is valuable especially in the case of biological problems, where non-static walls or bodies are the norm. In this framework, the NS equations are solved using a standard pseudo-spectral solver [125, 126, 127, 128] on a regular, triple-periodic grid, while each swimmer is represented by as few as three Lagrangian points whose geometry is prescribed by the internal forces. Two kinds of swimmer will be considered: a straight-swimming model in which the beads are in a line and, in a still fluid, move in a straight line with a stationary velocity proportional to a fixed propulsion force, also parallel to the swimmer itself; a model in which the flagellum and the body are at a constant angle, which at stationarity swims in a closed, circular trajectory. Based on previous literature this is called *circle swimmer* [129, 130, 131, 132, 133].

8.1 The immersed boundary method for a microswimmer

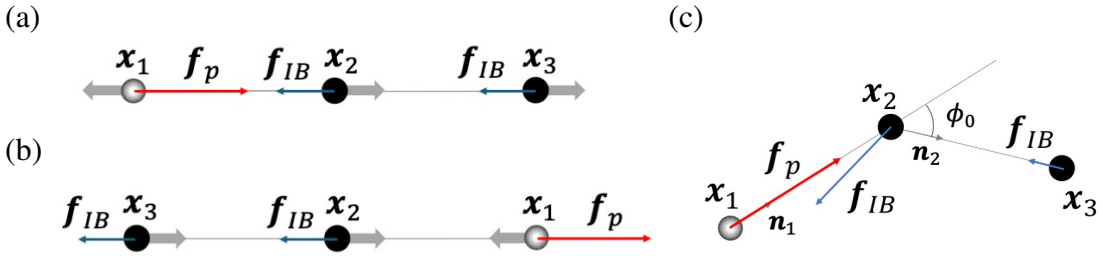

Figure 8.1: Schematic view of the model swimmer. (a) Three-sphere model for a pusher. The red vector $\mathbf{f}_p$ is the propulsion force per unit of mass (i.e. acceleration) that allows the motion. The blue vector is the acceleration due to the no-slip condition. The grey arrows are the forces exerted by the pusher on the fluid. (b) Three-sphere model for a puller. Notice that the position of beads $1, 3$ is exchanged with respect to panel (a). In both cases the swimming direction is from left to right. (c) A generic configuration for a pusher with a non zero angle ϕ_0 between the body and the flagellum.

It is reasonable to split the swimmer in two parts: a body and a flagellum. Following [113, 114] both the body and the flagellum are represented via a linear distribution of spherical beads connected by inextensible rods. Flagellum dynamics is not directly modelled (as shown in section 2.3.1) and the effects of propulsion are taken into account via localized forces applied to the fluid. The swimmer's body and flagellum are connected by inextensible rods whose configuration is held constant by internal forces, making the swimmer's shape rigid and inextensible. At each bead, a point force acts on the fluid. The nature of the forces acting along the body differs from those along the flagellum [108]. The body is considered as a rigid structure immersed in the fluid, along which no-slip conditions are assumed for the fluid velocity. The no-slip conditions are numerically enforced with a strategy derived from the IB methods, which will be described shortly. As a consequence, the body exchanges momentum with the fluid through viscous interaction, with no further modelling needed. On the contrary, the flagellum beads are not subject to no-slip conditions: they are instead used to apply the propulsive force onto the fluid,

while momentum conservation is guaranteed by applying an opposite force on the beads themselves and, thanks to rigidity of the rods, to the whole swimmer.

The simplest, bead-based swimmers proposed are made of two beads, i.e. one for the body and one for the flagellum [113]. As discussed above, the flagellum bead is not directly influenced by fluid velocity. It follows that a two-beads swimmer, with only one affected by the flow, is unaffected by velocity gradients along its body and, consequently, cannot behave as a passive rod in limit of vanishing propulsion. The minimal swimmer must therefore have at least two beads with no-slip boundary condition to describe the body. In principle, one bead is sufficient to describe the flagellum. It was shown that, if the same number of beads are used for the body and the flagellum, the velocity field surrounding the swimmer in steady motion is qualitatively similar to that produced by a force doublet [113]. In the following we will consider the simpler three-bead swimmer model, in analogy to previous theoretical [112] and numerical works [109, 111], which studied similar models with slightly different approaches. One of the novelties of the present approach is the possibility to have curved trajectories, when the three beads are not collinear. In perspective, one can dynamically change the body-flagellum geometry allowing for controlling the swimming direction. The latter property can be exploited to model the dynamics of microrobots to be employed, eg., in biomedical applications [90, 134].

Figure 8.1(a) represents a sketch of the three-sphere model for a pusher. The flagellum bead is labelled as 1. The force acting on it is the propulsion force per unit mass $\mathbf{f}_p$. This force is considered as fixed in modulus and parallel to the flagellum rod connecting beads 1 and 2. The inextensibility of the connecting rods implies that a similar force is applied to the body beads so that, in an otherwise still fluid, the resulting movement relative to the fluid produces on the body beads two drag forces, denoted as $\mathbf{f}_{IB}$ in the figure, in the opposite direction. Equal and opposite forces (indicated in gray) are applied to the fluid in the corresponding positions and guarantee momentum conservation. The model for pullers (Fig. 8.1(b)) is obtained by reversing $\mathbf{f}_p$ relative to the body. A generic, non-collinear configuration is shown in figure 8.1(c). When the flagellum is at a fixed non-zero angle with the body, the swimmer moves on a circular trajectory. For this reason the common name used for this configuration is circle swimmer [129, 130, 131, 132, 133].

8.2 The numerical implementation

As outlined above, the swimmer is described in terms of N spheres with centres at the points $\mathbf{x}_i$, with $i = 1, .., N$. In what follows the cases $N = 2$ and $N = 3$ are shown and let's assume that the 3D Eulerian problem of the evolution of the velocity field $\mathbf{u}(\mathbf{x}, t)$ is discretized in space on a uniform grid with grid spacing $h_x = h_y = h_z = h$ equal along all the axes. If the radius of the particles is comparable with h the 3D Navier-Stokes equations take the form

$$\frac{D\mathbf{u}}{Dt} = -\frac{\nabla p}{\rho_0} + \nu\Delta\mathbf{u} + \sum_{i=1}^{N} \frac{\mathbf{F}_i}{\rho_0 h^3}\Phi(\mathbf{x} - \mathbf{x}_i), \tag{8.1}$$

where ρ_0 is the fluid density, ν the kinematic viscosity, $\mathbf{F}_i$ is the force applied on the fluid by the sphere in $\mathbf{x}_i$. As typical with immersed boundary methods, the forces are regularized by spreading their effects on the nearby grid points with the function $\Phi(\mathbf{x})$, which has the following properties: $\Phi(\mathbf{x}) \geq 0$; $\Phi(\mathbf{x}) = 0$ for $|\mathbf{x}| > nh$, with n not necessarily integer, i.e. it has support over a finite stencil surrounding the particle; normalization, i.e. $\sum_{\mathbf{x}\in grid} \Phi(\mathbf{x}) = 1$ (sum over the points $\mathbf{x}$ of the numerical discretized domain) [119, 121]. The definition of $\Phi(\mathbf{x})$ has been chosen following [135]:

$$\Phi(\mathbf{x}) = \begin{cases} \frac{1}{3}\left(1 + \sqrt{-3|\mathbf{x}|^2 + 1}\right), & |\mathbf{x}| \leq 0.5h \\ \frac{1}{6}\left(5 - 3|\mathbf{x}| - \sqrt{-3(1 - |\mathbf{x}|)^2 + 1}\right), & 0.5h \leq |\mathbf{x}| \leq 1.5h \\ 0, & \text{otherwise.} \end{cases} \tag{8.2}$$

The Lagrangian problem associated with the motion of the swimmer requires the knowledge of the fluid velocity $\mathbf{u}(\mathbf{x}_i)$ at the position of each bead, which is defined as a weighted average of the fluid velocity surrounding the bead

$$\mathbf{u}(\mathbf{x}_i) = \sum_{\mathbf{x}\in grid} \mathbf{u}(\mathbf{x})\Phi(\mathbf{x} - \mathbf{x}_i). \tag{8.3}$$

For what concerns the forces, as discussed above, the flagellum and the body are treated differently. A flagellum bead is characterized by a constant propulsion force contributing an acceleration $\mathbf{f}_p$ applied on the bead along the flagellum. An equal and opposite force is applied on the fluid to guarantee conservation of momentum. A body bead is instead

part of a material boundary along which the natural no-slip condition applies. In line with the IB strategy, each body bead is subjected to the acceleration $\mathbf{f}_{IB} = \beta(\mathbf{u}(\mathbf{x}_i) - \mathbf{v}_i)$, where $\mathbf{v}_i$ is the velocity of the $i-$th bead and β is a large, positive numerical parameter. Also in this case a force of opposite sign is applied to the fluid. Such IB forces lead to the reciprocal relaxation, with a characteristic time β^{-1} of bead and fluid velocities to the same values, thus enforcing the no-slip condition. Clearly β affects the relative error on the implementation of the no-slip condition. If the swimmer moves with a constant swimming velocity v_s in a still fluid the IB forces are the equivalent of the viscous drag forces so one must have $f_{IB} \simeq \mathrm{v}_s/\tau_S$, with τ_S an effective Stokes time of a bead which can be estimated from the parameters obtained with the fitting procedure described below. This implies that $|\mathbf{u}(\mathbf{x}_i) - \mathbf{v}_i|/\mathrm{v}_s \simeq (\tau_S\beta)^{-1}$.

The resulting equations of motion for a 3-bead swimmer are:

$$\begin{cases} \dot{\mathbf{v}}_1 = f_p\mathbf{n}_1 + \Lambda_{12}\mathbf{n}_1 + g\mathbf{t}_1 \\ \dot{\mathbf{v}}_2 = -\Lambda_{12}\mathbf{n}_1 + \Lambda_{23}\mathbf{n}_2 - \beta\left(\mathbf{v}_2 - \mathbf{u}(\mathbf{x}_2)\right) + g\mathbf{t}_2 \\ \dot{\mathbf{v}}_3 = -\Lambda_{23}\mathbf{n}_2 - \beta\left(\mathbf{v}_3 - \mathbf{u}(\mathbf{x}_3)\right) + g\mathbf{t}_3 \end{cases} \tag{8.4}$$

In these equations Λ_{ij} denotes the Lagrange multiplier associated with the inextensibility of the rod connecting beads i and j, $\mathbf{n}_1$ and $\mathbf{n}_2$ are unit vectors parallel to the rods and $g\mathbf{t}_i$ are stiff elastic forces acting normal to the rods and implementing the constraint of fixed angle ϕ_0 (see Fig. 8.2). Thus the magnitude g is computed in dependence to the difference between ϕ_0 and ϕ as follows:

$$g = -a(\phi - \phi_0), \tag{8.5}$$

where a is a constant setting the stiffness of the spring which keeps ϕ close to ϕ_0. The individual terms and the geometrical description are discussed in details in Appendix B.2.

The evolution of the Eulerian velocity field is realized by means of a standard, fully de-aliased, pseudo-spectral code [127, 128]. Although both the model and its integration are fully three-dimensional, in the following, for the sake of simplicity in visualizing the results, the problem is restricted to the (x, y) plane by a suitable choice of the initial conditions for the swimmers.

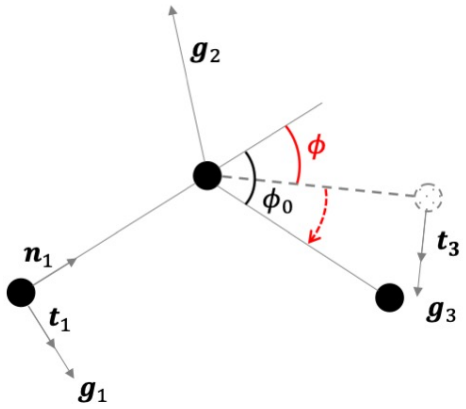

Figure 8.2: Schematic view of the model swimmer. The internal forces $\mathbf{g}_1, \mathbf{g}_2$ and $\mathbf{g}_3$ allow to control the angle or keep it fixed.

The rhs of both (8.1) and (8.4) have the dimension of forces per unit mass. As detailed above, each force $\mathbf{F}_i$ in the last term of (8.1) is due to conservation of momentum and is the opposite of forces acting on the beads and causing the propulsion acceleration or the relaxation to fluid velocity. Denoting one of the Lagrangian accelerations as $\mathbf{f}_i$ in (8.4), one must have $\mathbf{F}_i = -m\mathbf{f}_i$ where m is the bead's mass. For a spherical bead we can write

$$\frac{\mathbf{F}_i}{\rho_0 h^3} = -\mathbf{f}_i \frac{\rho}{\rho_0 h^3} \frac{4}{3}\pi R^3 \equiv -\mathbf{f}_i c, \tag{8.6}$$

where ρ and R are the bead's density and radius, respectively and $c = \frac{4}{3}\pi \frac{\rho}{\rho_0} \left(\frac{R}{h}\right)^3$ determines the relative intensity of Lagrangian acceleration and feed-back on the fluid. For simplicity, in the following, only neutrally buoyant swimmers are considered ($\rho = \rho_0$).

8.2.1 Fixing the numerical parameters

At Re $\ll 1$ an approximate analytical solution for the creeping flow can be easily obtained and used to fix the numerical parameters. This is achieved by analysing the simpler case of a pusher consisting of two beads connected by a rigid, inextensible rod (see Fig. 8.3(a)). One of those beads represents the flagellum and one the body and this configuration produces two opposite forces on the flow and, therefore, an approximate force dipole field which decays as r^{-2} in space [94]. Let 1 and 2 be the index of the flagellum and body

beads respectively, in this case the equations of motion (8.4) simplify to

$$\begin{cases} \dot{\mathbf{v}}_1 = f_p \mathbf{n} + \Lambda \mathbf{n} \\ \dot{\mathbf{v}}_2 = -\Lambda \mathbf{n} - \beta(\mathbf{v}_2 - \mathbf{u}(\mathbf{x}_2)), \end{cases} \tag{8.7}$$

where $\mathbf{n} = (\mathbf{x}_2 - \mathbf{x}_1)/|\mathbf{x}_2 - \mathbf{x}_1|$ and Λ is the Lagrange multiplier associated with inextensibility.

The value of c in (8.6) can be fixed by using the (approximate) analytical solution of the Stokes flow around the two spheres, i.e. equation (1.7). Let L represent the distance between the spheres moving at velocity v_s. The swimmer Reynolds number is taken as $\mathrm{Re} = \mathrm{v}_s L/\nu = 10^{-2}$, and the longitudinal component of the fluid velocity along the swimmer's axis is then computed. Periodicity of the domain is taken into account by considering the images in the three directions. Figure 8.3(b) shows the comparison between the analytical (discussed in Appendix B.1) and numerical results, which gives the fit $c \simeq 5.58$, corresponding to $R \simeq 1.1h$. The analytical solution in the regions within the effective radius of the beads (the gray regions in Fig. 8.3(b)) is excluded from the comparison since it is singular and unphysical. The numerical solution, on the other hand, is well behaved also in those regions. The consistency of the definition of c has been tested by verifying that it is not affected by the resolution of the grid (up to 256^3 points) and is also independent of Re when $\mathrm{Re} \lesssim 1$.

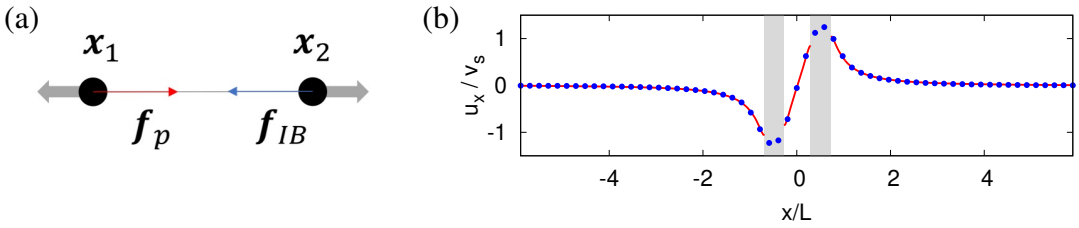

Figure 8.3: (a) Scheme of a two-sphere pusher. The gray arrows are the forces exerted by the pusher on the fluid. (b) x-component of the velocity field along the swimming direction produced by the two-sphere pusher with $\mathrm{Re} = 10^{-2}$. The red line represents the analytical Stokes solution, blue points are the numerical values computed with $c = 5.58$ with resolution 64^3.

8.3 Numerical results for rectilinear swimmers

Now we consider the case of rectilinear swimmers composed of three spheres connected by two rods of length L. In Fig. 8.1 bead 1 represents the flagellum, while beads 2 and 3 define the body. The whole system is considered rigid and inextensible. Inextensibility is enforced via Lagrange multipliers while bending rigidity is guaranteed via stiff springs, which is sufficient to prevent oscillations. The length of the swimmer is defined as the distance L between the two body-beads, thus neglecting the presence of the flagellum. Therefore, the Reynolds number is defined as in the case of two-sphere model $\mathrm{Re} = \mathrm{v}_s L/\nu$.

8.3.1 Single swimmer

The results of a numerical simulation of a single 3-bead swimmer moving with constant velocity, at $\mathrm{Re} = 10^{-2}$, in an otherwise quiescent fluid are shown in figure 8.4. In figure 8.4(a), a 2D section of the 3D domain containing the pusher is shown. At the stationary state, from eq. (8.4) one must have $\mathbf{f}_p = -\beta(\mathbf{v}_2 - \mathbf{u}(\mathbf{x}_2)) - \beta(\mathbf{v}_3 - \mathbf{u}(\mathbf{x}_3))$. In this case the distribution of forces among the three spheres is less trivial than the completely symmetric case of the 2-sphere model. Figure 8.4(a) shows that the velocity produced by propulsion around the flagellum bead is, in agreement with the above relation, larger in magnitude than the disturbance produced by viscous drag around each of the body beads and it is comparable with the sum of the velocity field produced by the others, according to the rigidity condition and to the conservation of momentum. While the far field properties of the flow are dominate by the pusher/puller nature of the swimmer, the differences between our three beads model and other models like the dipole swimmers or squirmers are particularly relevant close to the swimmer itself and therefore can affect short-range hydrodynamic interactions [136].

In figure 8.4(c-d) the puller dynamics is shown. The results are symmetric with respect to the pusher case, as expected in the very low Re regime. In the case of higher Re, the pusher and puller dynamics should present substantial differences. Indeed this is observed in simulations of our model for $\mathrm{Re} = \mathrm{O}(1)$. Figure 8.5 shows the velocity fields produced by a pusher and a puller at $\mathrm{Re} \simeq 1.6$. In this case the asymmetry between the two configurations is apparent. It should also be noted that the force applied to the

pusher attains the same velocity with a force that is smaller (about 0.7 times) than the one applied to the puller. In other words, at finite Re a pusher swims *faster* than a puller with the same propulsion, at least in this regime. This is consistent with results obtained with other models [137, 113]. It is important to stress that the absence of an analytical benchmark for such values of Re does not allow a quantitative validation of the model in this regime.

8.3.2 Non-motile swimmer

As a preliminary test for the dynamics of the model we consider the case of a swimmer without any propulsive force, i.e. $\mathbf{f}_p = 0$, immersed in a steady shear flow. As a model flow we chose, for numerical convenience, a Kolmogorov flow $\mathbf{u} = (\cos(z), 0, 0)$ [25, 138]. We consider a non-motile swimmer initially resting in the (x, z) plane and oriented perpendicular to the flow at $z = 3\pi/2$, i.e., at the flexus of the flow. As detailed in Appendix B.3, in the absence of propulsion, i.e. when the flagellum does not play any role, the body of the swimmer should behave as an infinitely thin rod and its dynamics is ruled by Jeffery's equation as illustrated in section 1.3. In the configuration described, the flow can be approximated as a homogeneous shear with shear rate $\sigma = du_x/dz$. Using a 2D reference system in which the swimming angle is measured from the horizontal direction ($n_x = \cos\theta$, $n_y = \sin\theta$), one can rewrite the equation as:

$$\dot{\theta} = -\frac{\sigma}{2}[1 + \lambda(1 - 2\cos^2\theta)]\,, \tag{8.8}$$

where, in our case, $\sigma = 1$. If $\lambda = 1$, i.e. a thin rod, $\theta = 0$ is a marginally stable fixed point. The solution for a rod that starts perpendicular to the shear direction is given by

$$\begin{cases} \theta(t) = \operatorname{arccot}(\sigma t) \\ \theta(0) = \pi/2. \end{cases} \tag{8.9}$$

The eq. (8.9) will describe the motion of a three-bead swimmer in a linear shear when the propulsion is switched off. We stress that the flagellum bead can be completely disregarded in this regime.

Figure 8.6 shows the time evolution of the orientation of a non-motile swimmer compared with the analytical solution (8.9). The numerical solution is obtained by the

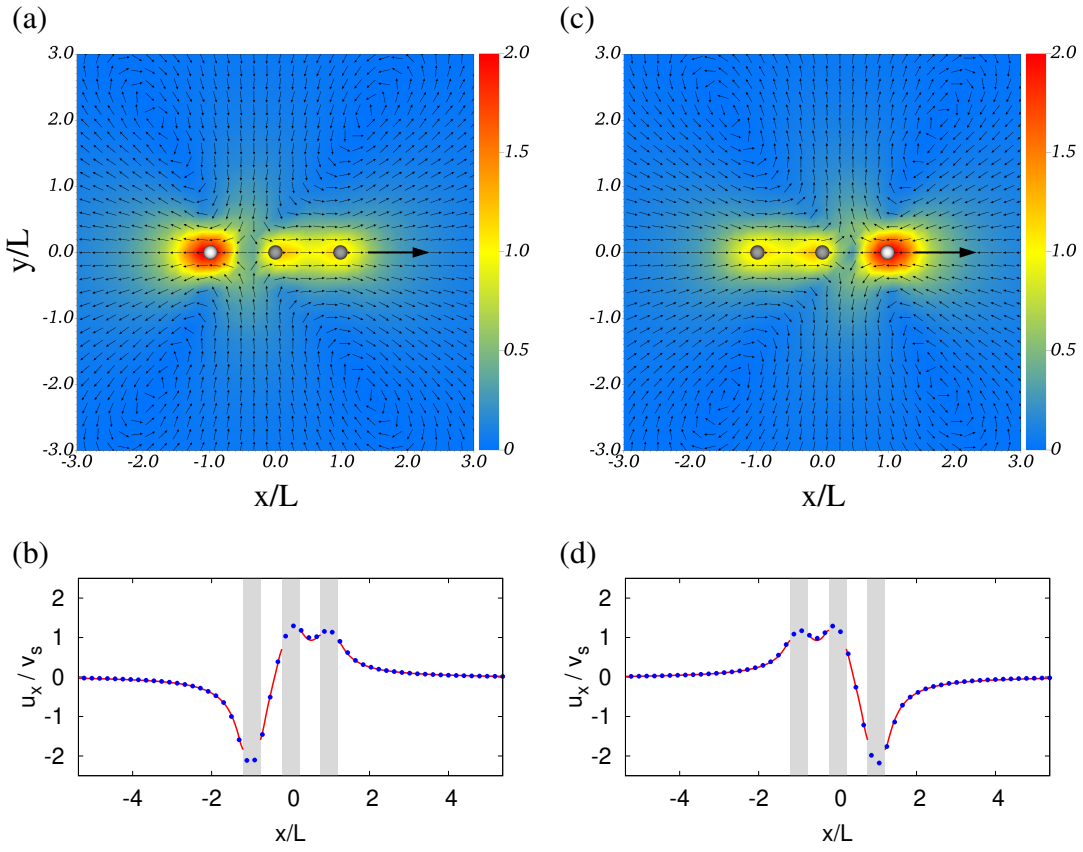

Figure 8.4: Velocity field surrounding a 3-bead pusher (a-b) and puller (c-d) at the stationary state for Re = 0.01. Velocities are rescaled with the constant swimming speed. (a) The colour map indicates the amplitude of the velocity, while the arrows (not scaled with amplitude) indicate the local velocity direction. The typical *pusher* configuration (outwards streamlines along the swimmer axis, inwards in the normal direction) can be clearly appreciated. The swimmer is moving to the right. The leftmost white bead represents the flagellum, where propulsion is applied. The corresponding reaction force on the fluid produces an intense velocity perturbation (red region). The black arrow on the right indicates the swimming direction. (b) Plot of the x-component of the velocity field along the swimming direction of a 3-beads swimmer. The numerical solution (blue dots) is compared with the approximate analytical solution (continuous line, see text). Note that, as expected, the fluid field on the tail beads (on the left) is comparable with the sum of the velocity field produced by the others, as a consequence of inextensibility and conservation of momentum. (c-d) Same as panels (a-b) but for a puller. Notice the leading (white) flagellum bead. The clear specular symmetry between the two configurations is due to the time-reversal invariance of the equations at low Re.

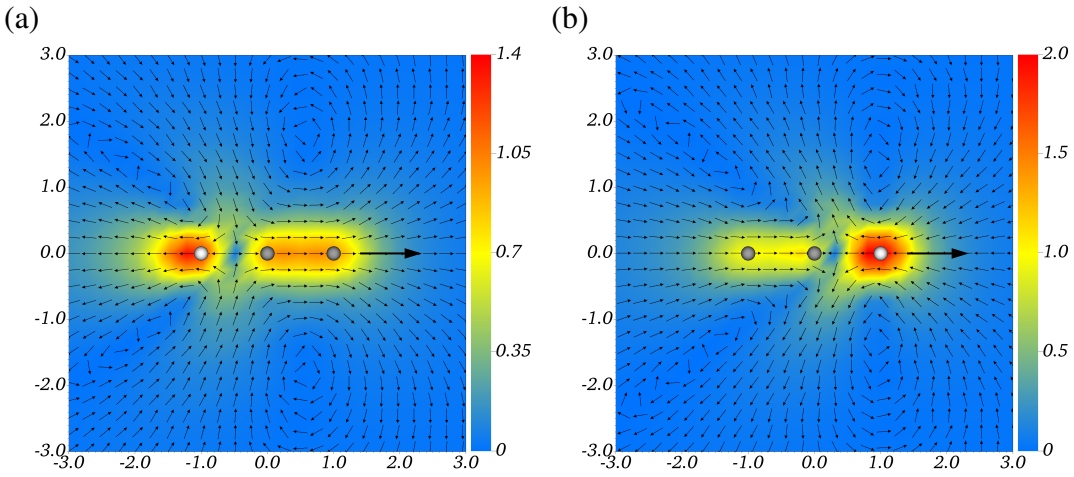

Figure 8.5: Velocity field produced by (a) a pusher and (b) a puller at Re $\simeq$ 1.6. In contrast to Fig. 8.4 the two configurations show no clear reflection symmetry, due to the breaking of time reversal symmetry at finite Re.

integration of a three-bead swimmer placed in the inflection point at $z = 3\pi/2$. The numerical result in figure 8.6 is compared with the analytical expression (8.9) valid for an ideal rod-like particle. The deviations can be quantified by observing that the time it takes for the numerical swimmer to reach 0.1rad is only 10% larger than the theoretical prediction. Such a small difference should be irrelevant when time dependent flows are considered. It is possible to conclude that for this model swimmer, a linear shear in a creeping flow regime gives rise to a dynamics that can be described by Jeffery's equation (1.14) with $\lambda = 1$. This suggests that, for an isolated swimmer in flow that varies on a scale sufficiently larger than the swimmer's body, this model could be substituted with a kinematic model obtained from Jeffery's equations for a rod with a superposed swimming velocity. However, when more than one swimmer is considered, hydrodynamic interactions would not be accounted for by such model. Moreover, if many swimmers are considered, the flow itself would strongly affected by the swimmers, which could be the main forcing in the fluid as in the case of active turbulence.

8.3.3 Swimmers interaction

The problem could be increased in complexity considering the interaction between two swimmers and the resulting trajectories. We consider the effects of hydrodynamic in-

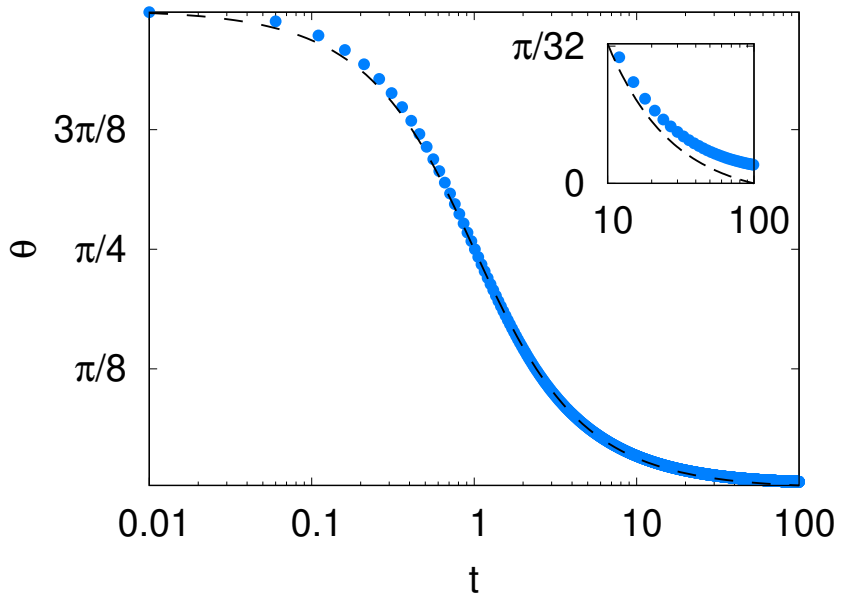

Figure 8.6: Comparison between the solution (8.9) of Jeffery's equation for a rod (formally, an ellipsoid with $\lambda = 1$, dashed line) and numerical data from the 3-beads model (blue dots) without propulsion in a Kolmogorov flow. Numerical simulations are done at resolution $N = 64^3$ grid points in a cube of size 2π for a swimmers of length $L = 0.5$ with initial orientation $\theta = \pi/2$. Inset: zoom of the long time behavior, see text for a discussion.

teractions without incorporating any additional repulsive potential to account for steric interactions. The latter can be anyway added to the model in straightforward ways. Let's remark that in this model swimmer there are no physical rods connecting the beads. Therefore, in principle, swimmers can overlap with crossing trajectories. Nevertheless, It has been observed that, if the beads are not too far apart, swimmers feel each others as effective *continuous* bodies, thanks to the flow produced in their motion and overlaps are observed only in very special conditions.

The first step is to consider the scattering of two identical swimmers, moving at the same speed, with an incident angle θ_i. One example is shown in figure 8.7(a) with $\theta_i = \pi/4$. The scattering is a complex process during which the two swimmers orient temporarily in a parallel direction and finally emerge with a different output angle θ_o. In the case of pusher swimmers, the velocity field (see Fig. 8.4(a)) causes the flagella to come

closer together, turning the swimmers and leading first to the alignment of the swimmers and subsequently to a separation of the directions. The above described phenomenology is consistent to what found in [112, 111] starting from parallel swimmers. For a pair of pullers, the kinematics is qualitatively very similar, except that the hydrodynamics which produces it is opposite to that of pushers (see Fig. 8.4(c)). The flagella, which in this case are the first to interact, tend to repel each other, leading to the same kinematics of alignment and subsequent divergence of the trajectories. The exit angle is consequently different in the two cases, as evident from comparing figures 8.7(a) and (b). Let's remark again that the model does not exclude the possibility of observing the overlap between swimmers under certain conditions (for example, in the case of high Reynolds numbers or very large collision angle). The most common case is a superposition of the flagella. This event is not per se problematic because in our model the flagella are not affected by hydrodynamic interactions. In this approach (and at variance with other approaches [111] where the particles have a finite volume which behaves as a second fluid with a large viscosity) the beads are effectively represented as regularized point forces whose effective radius is a numerical parameter used to fit the resulting velocity field. The occasional partial overlap of the force stencils can therefore cause numerical stiffness, by introducing large local forces, but is not necessarily physically inconsistent. The cases in which also the bodies overlap can be avoided with an effective, short-range repulsion potential. Such potential can take different forms essentially corresponding to steric interactions between the beads or between the bodies (through the definition of an effective shape). Only the effects of hydrodynamic interactions are here considered and no numerical instability was observed as a result of the overlap of the tails or the bodies in the case of binary collisions.

8.4 Circle swimmer dynamics

The 3-beads model allows to control the swimming direction in a simple and natural way. Indeed, when the three beads are not in a collinear configuration, the drag on the body together with the propulsion from the flagellum produce a torque that rotates the swimmer. In the following we show only results concerning circle pushers, where the flagellum bead is the trailing one. As previously discussed, puller-like circle swimmers

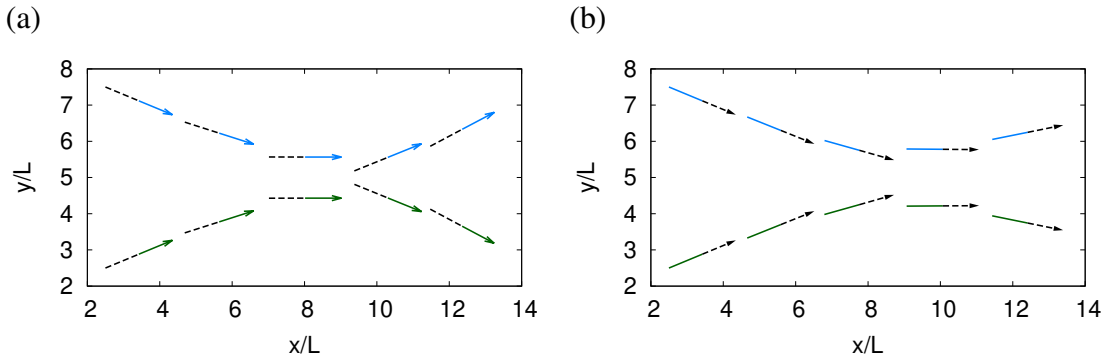

Figure 8.7: Collision of two identical swimmers starting with a relative angle of $\pi/4$. The hydrodynamic interaction between by the body's beads allows the swimmers to scatter without touching each other. (a) Pusher dynamics. The subsequent positions of the swimmers are plotted, left to right, at regular time intervals. The solid arrows indicate the inextensible rod connecting the body beads, while the dashed lines represent the flagella, connecting the rear body beads to the flagellum beads. Only the body segment is considered as a rigid boundary, on which the no-slip condition is applied for the fluid. (b) Pullers dynamics. The same time series of pushers' case is shown. The interaction in this case produces a smaller output angle due to the different hydrodynamic interaction between the swimmers.

can be obtained by reversing the propulsion. The controlling parameter for the swimmer is the equilibrium angle ϕ_0 between the flagellum rod and the body rod. The resulting trajectory of a single swimmer is a circle with a radius R_c depending on ϕ_0. Clearly in the limit $\phi_0 \to 0$ one recovers the original collinear model, with $R_c \to \infty$. One should note that when circular trajectories are observed in biological microswimmers, these are due to the swimmer's chirality. The latter results in helical swimming in the bulk and circular trajectories when confined to a surface [130]. A model describing a chiral swimmer would in principle require at least four beads, considering such an extension to the model goes beyond the scope of this work. However, this development may be the subject of future research, given the flexibility and simplicity of the model here proposed.

Once the bending angle is set, the rigidity of the swimmer is guaranteed by an elastic force that causes the relative position of the two rods to relax to that angle. This elastic force is implemented in the form of internal forces $\mathbf{g}_i$, one for each bead (see

Appendix B.2). Referring to (8.5), this means that if a perturbation produces deviations from the equilibrium angle ϕ_0 these are compensated by the torques due to the internal forces, bringing the system to the wanted configuration. It is worth noting that eq. (8.5) should produce a harmonic oscillation of the angle ϕ around ϕ_0. These oscillations are damped by viscosity through the no-slip condition on the body beads, thus causing a relaxation to the prescribed angle ϕ_0.

8.4.1 Circular trajectories of isolated swimmers

Figure 8.8 shows two examples of circular trajectories produced by circle swimmers with different bending angles, together with the dependence of the radius of the trajectory on ϕ_0. Observing that the segments identifying the body and the flagellum are approximately tangent to the circles described by head and middle beads, respectively, one can tentatively estimate the radii of those circles as $r_{\text{head}} \sim L/\tan(\phi_0)$ and $r_{\text{mid}} \sim L/\sin(\phi_0)$. The actual radii (see Fig. 8.8(c)) are smaller than the estimate (dashed lines) except for $\phi_0 \sim \pi/2$, in which case the head is almost stationary ($r_{\text{head}} \sim 0$) and the flagellum rotates by remaining approximately tangent to the outer circle ($r_{\text{mid}} \sim L$). More complex trajectories can be obtained if we allow the angle to change in time, and this can be used to control the swimming trajectory. The dynamics of active steering could be the subject of future investigations.

8.4.2 Swimmers interaction

In analogy with the case of a straight swimmer, the focus is on the interaction of two circle swimmers. The bending angle is fixed at $\pi/4$ as shown in figure 8.8(a). Two different behaviors were observed, depending on the relative initial positions of the swimmers. If the initial separation is large enough, as expected, each swimmer tends to swim on its own curvilinear trajectory without interacting, in some cases after a brief transient characterized by a repulsive interaction. Two examples of this behavior are shown in figure 8.9(a), corresponding to different initial conditions. If the initial separation is further decreased (Fig. 8.9(b)) the interaction changes qualitatively. After a more complex initial transient, the two trajectories intertwine and start revolving around the same centre.

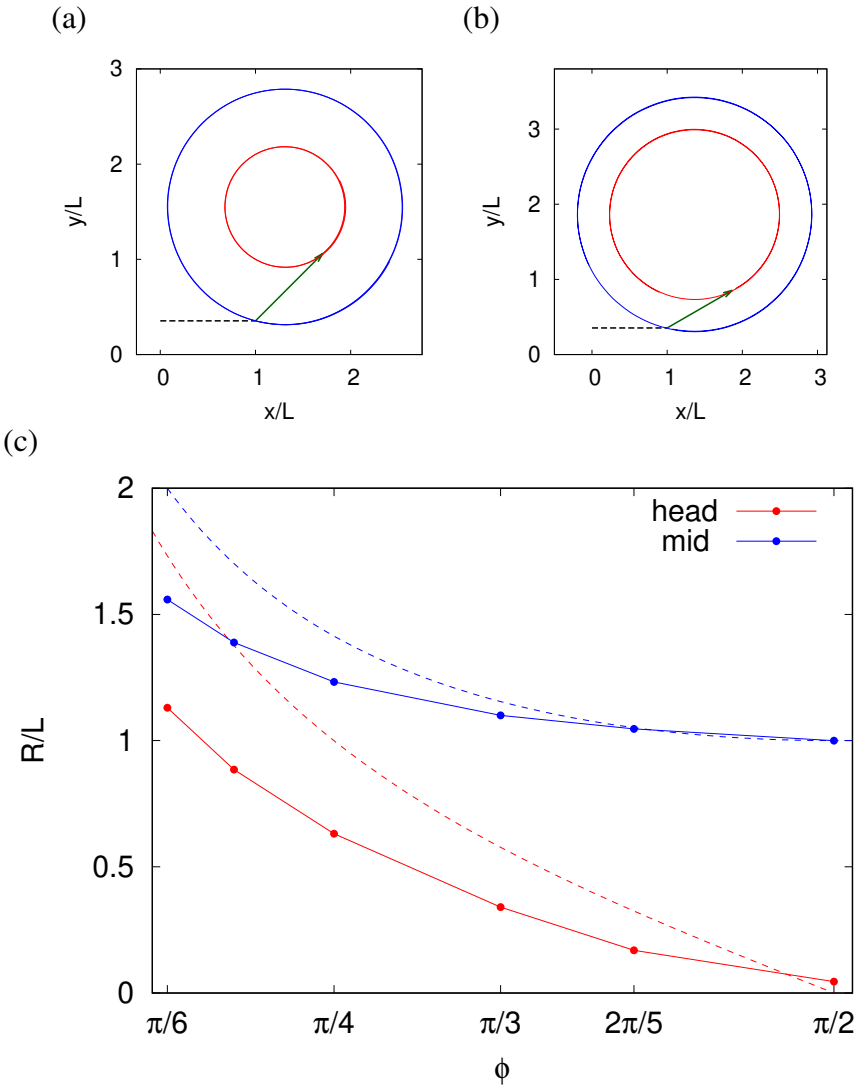

Figure 8.8: Trajectories of isolated swimmers with a constant bending angle. (a,b) Two typical trajectories, with $\phi_0 = \pi/4$ and $\phi_0 = \pi/6$, respectively. The red (blue) lines mark the trajectory of the head-bead (mid-bead). (c) Dependence of the radii of the trajectories of the head and mid beads (solid lines) on the angle ϕ_0 between the flagellum and the body. The results obtained with a simple model (dashed lines, see text) are given for comparison.

It is worth noting that the reciprocal positions of the swimmers are not locked along the orbit but change dynamically in a non-trivial way. In the presence of many swimmers, a random initial configuration can lead one swimmer to decouple from one neighbour (as

in Fig. 8.9(a)) only to be attracted by another one into forming a strongly coupled pair (as in Fig. 8.9(b)). This mechanism could lead to an ordered collective behavior as briefly discussed in the next section.

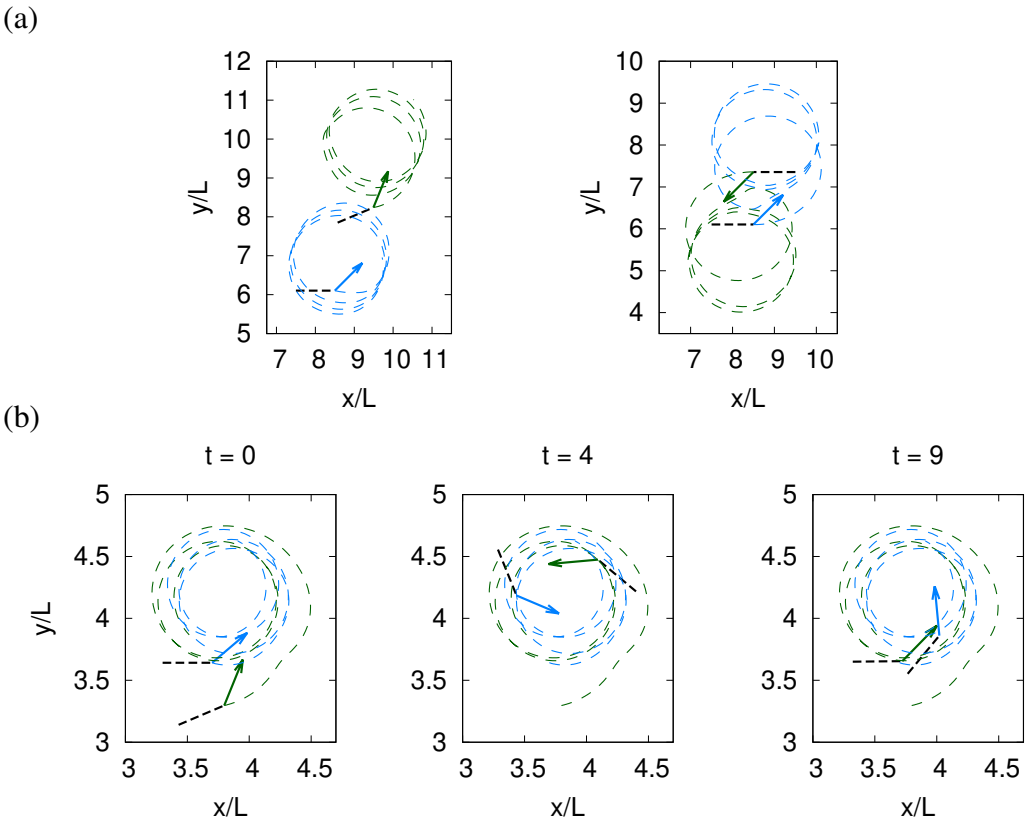

Figure 8.9: Interaction between a pair of circle swimmers. (a) Two configurations are shown in which after a transient the two swimmers settle onto essentially independent trajectories. (b) Dynamics of two swimmers starting initially very close and nearly parallel. In this case the two trajectories are intertwined and revolve around a common centre. Note how the relative positions of the swimmers change during their orbits. The position is rescaled with the rod length between two beads and times are rescaled with the period of the isolated circular trajectory.

8.5 Collective behavior

The numerical method proposed in this work can be easily scaled to a large number of swimmers to study their interaction and the emergence of collective motion. In this

section, we consider the evolution of the distributions of hundreds of straight (in the next subsection) and circle swimmers (in the following one).

8.5.1 Rectilinear swimmers

As first example we considered 500 identical straight pushers initially placed at random positions and directions on a (x, y) plane in the 3D domain. In the absence of perturbations in the z direction, the motion remains planar, thus confirming the accuracy of the numerical integration.

One snapshot of the configuration of the swimmers at late time is shown in figure 8.10. We observe that the distribution is not random any more, with local clusters (or schools) swimming in a parallel direction, similarly to the intermediate state observed in figure 8.7. This configuration is highly dynamical, as different clusters appear and dissolve in time in a statistically stationary condition (see Fig. 8.10(b,c,d)). Figure 8.11 shows the correlation function of the swimming angle as a function of the distance between the swimmers [139]. Being $\mathbf{s}$ the unit vector in the swimming direction we define for the case of N swimmers:

$$C(r) = \left\langle \frac{\sum_{ij}^{N} \delta\mathbf{s}_i \cdot \delta\mathbf{s}_j \delta(\mathrm{r} - \mathrm{r}_{ij})}{\sum_{ij}^{N} \delta(\mathrm{r} - \mathrm{r}_{ij})} \right\rangle \tag{8.10}$$

where $\delta\mathbf{s}_i = \mathbf{s}_i - \frac{1}{N}\sum_i \mathbf{s}_i$ is the deviation of the orientation from the mean, r_{ij} is the distance between two swimmers and $\langle\cdot\rangle$ is an ensemble average which in our case was exchanged with a time average, assuming ergodicity. The correlation is positive over a distance of the order of the length L. For a large enough number of swimmers the correlation length becomes independent on the number of swimmers. In this dense condition confined on a plane, the occurrence of overlapping swimmers is not uncommon. In a realistic application with the full 3D motion, the overlap would be much more occasional as the mean free path of swimmers would be much larger. Remarkably, even in the case of figure 8.10 we find that the swimmer model does not develop numerical instabilities as a consequence of the close encounters. However, when a similar case is studied for pullers (not shown), the ensuing clustering is much stronger than for pushers [140, 141] and rapidly leads to numerical instabilities due to the overlap of a large number of beads, with their relative force stencils. Clearly in this case a steric repulsion force must be

implemented. Steric interactions could likely modify also the correlations (8.11) and other characteristic of the collective motion.

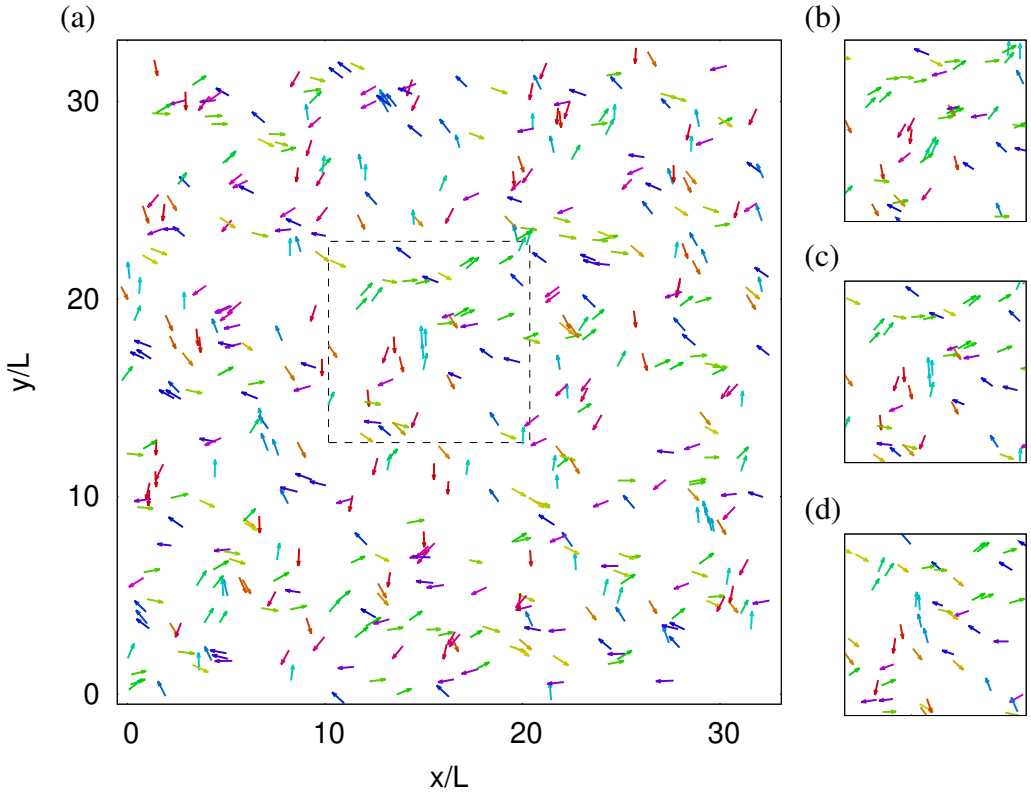

Figure 8.10: Panels (a-d): collective behaviour of 500 straight pushers in a 2D configuration within a 3D fluid domain. In this figure the flagella are not drawn and each swimmer is coloured based on its angle with respect to the x axis, so that parallel swimmers have the same colour. The fluid is forced into a chaotic flow by the motility of the swimmers. The resulting velocity fluctuations induce relatively large velocity differences between nearby swimmers which occasionally defeat the repulsive effect of hydrodynamic interactions and cause the bodies to overlap more frequently. The formation of clusters of schools of swimmers sharing the same swimming direction is highlighted by the colouring scheme. On the left a 2D snapshot of the whole domain at time $t \simeq 23$ (rescaled with the typical time in which the swimmer covers its length) is shown. (b), (c) and (d): three zoomed snapshots of the dynamics within the dashed square in panel (a). Panel (b) and (c) are taken at a time interval $\Delta t = 0.30$ before and after the main panel (corresponding to panels (a) and (c)), respectively. It is here evident that the schools persist several swimmer lengths following the surrounding dynamics.

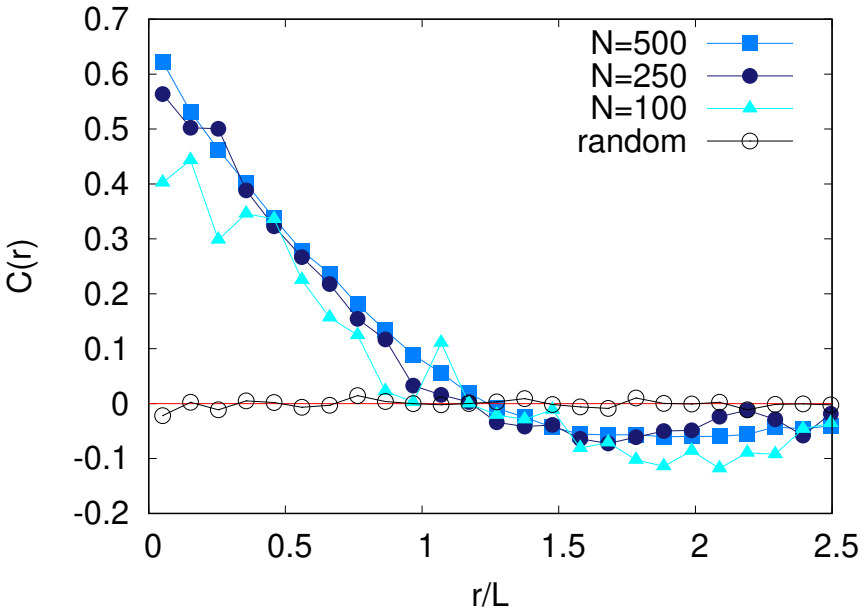

Figure 8.11: Correlation function of swimming directions $C(r)$ between swimmers separated by a distance r (see text), computed for different numbers of swimmers. The angles of neighbouring swimmers are correlated over a distance roughly equivalent to the length L, which is consistent with the clusters shown in figure 8.10. As a comparison, the same observable is shown for random configurations.

8.5.2 Circle swimmers

The discussion in the previous section, as well as previous literature [133, 131], suggest that circle swimmers can present interesting collective dynamics. Also in this case we show here only results regarding circle pushers, since pullers tend to undergo strong clustering that requires the implementation of steric interactions. We considered the case of 250 circle pushers (Fig. 8.12). The collective dynamics in this case is characterized by a transient in which swimmers with an initial condition similar to those observed in figure 8.9(a) tend to move apart until they intersect other trajectories with which to form a collective circular trajectory, as shown in figure 8.9(b). An example of the resulting collective motion is shown in the side panels of figure 8.12. Once swimmers achieve this coupled configuration, the dynamics become rather complex because each orbit is traveled at different and non-constant speeds. Starting from a configuration where all swimmers are closely packed (Fig. 8.12(b)), the flow generated by each pusher accelerates

the nearby swimmers, causing a fast rotation and a progressive separation (Fig. 8.12(c,d)) of the swimmers along their collective orbit. At later times a packed configuration forms again. This behavior repeats and allows the formation of these structures on the scale of the swimmer. Preliminary observations suggest that, once formed, these structures tend to persist and produce a global configuration characterized by many swimmer vortices (Fig. 8.12(a)). Such vortices survive for several orbital periods (estimated via the orbital period of an isolated circle swimmer) and are therefore qualitatively robust, as shown in figure 8.12(b-d). Quantitative assessment of the persistence of the collective structures as well as their statistical correlations is needed, in order to fully characterize this system, and will be the subject of future investigations focused on the collective motion.

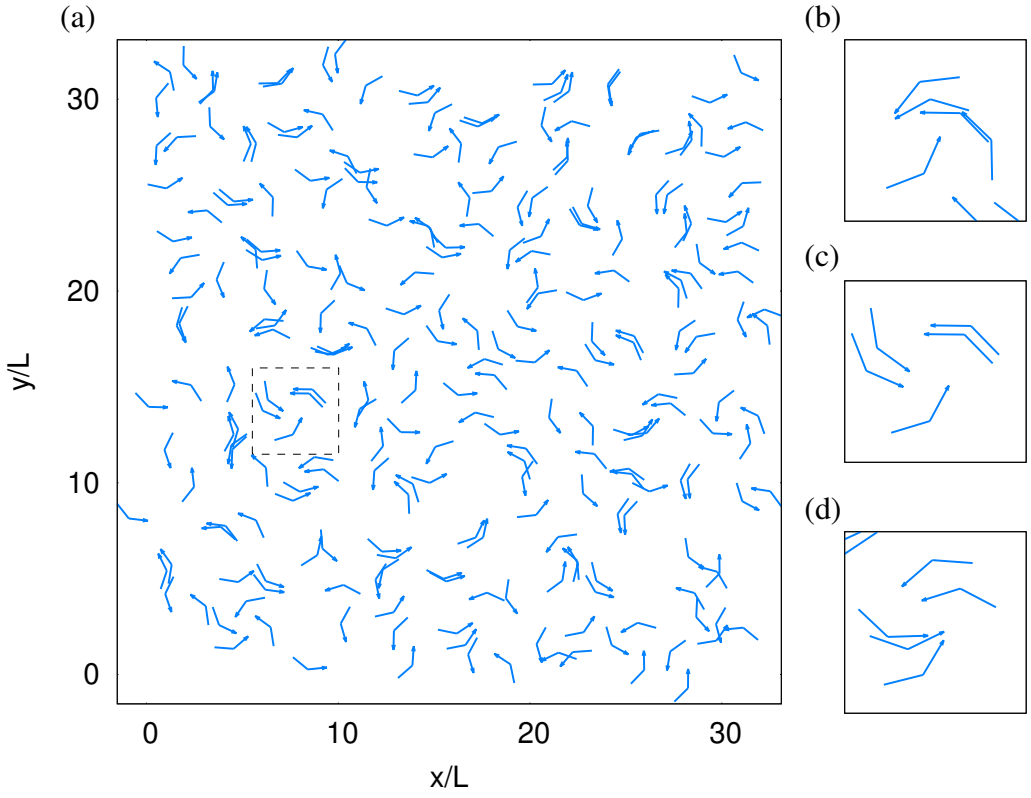

Figure 8.12: Collective behavior of 250 turning swimmers in a 2D configuration. The dynamics is characterized by the formation of groups of swimmers that, thanks to the hydrodynamic interaction, pair up to form groups of swimmers that evolve along nearly circular, approximately concentric trajectories. These structures are very robust and survive for several orbits. On the left a 2D snapshot of the whole domain. On the right three zooms of the dynamics of one structure. The central plot (c) shares the same time of the snapshot on the left and is preceded in time by the snapshot (b) at time $t \simeq -3T_0$ (in units of the period T_0 of a circular trajectory of the single circle swimmer) and followed by the snapshot (d) at time $t \simeq +3T_0$.

Conclusions

The theoretical models and simulations proposed in this thesis fall within the framework of applying physical theories and methodologies to the study of small-scale living organisms, with the aim of understanding and predicting their behaviours in response to the environment.

In this thesis we have first studied the dynamics of elongated microorganisms swimming in the flow produced by water waves and a linear shear. We have investigated in detail how the interplay of swimming and flow leads to trapping of the microswimmers below the water surface. The analysis has been done by exploiting the multiple scale analysis complemented by numerical simulations in kinematic flows. In general, our results demonstrate that the combination of swimming and flow (and/or gravity) can produce trapping but this process depends on the details of the physical and biological parameters. In particular, we have found that the presence of a shear (in combination with waves) close to the surface is essential to produce confinement with realistic values of the parameters. This is promising finding with regards to how the mechanisms discussed above could lead to the production of 'thin phytoplankton layers' since wind-generated shear will often accompany locally generated waves.

Future investigations should consider more realistic models of the microswimmers (e.g. including some randomness in the swimmer behavior) and of the velocity field, beyond the kinematic model for linear waves, as for example in the case of nonlinear waves where fluid accelerations may also become comparable to gravity requiring a more complete model of gyrotaxis [52]. Furthermore, it would be very interesting to study the problem of swimmer-water wave interaction by means of laboratory experiments with real microswimmers to see the degree of agreement with this simple model.

In the second part of the work we have proposed and analysed a numerical model based on immersed boundary methods of a minimal swimmer, whose body is modelled by two beads and flagellum represented by a single bead. The model can be used for both pushers and pullers, by simply changing the direction of the applied forces. The choice of two beads, with no slip conditions, for the body make the swimmer to feel the gradient of the velocity field allowing it to be rotated by the flow. In particular, We showed that, when the propulsion is switched off, the swimmer moves approximately according to Jeffery's equations for a thin rod.

When the three beads are collinear the model swimmer display straight swimming, while by maintaining an angle between body and flagellum it swims in circles. We analysed the close encounters between both straight and circle swimmers showing how hydrodynamic interactions mediated by the solvent fluid make the two swimmers to scatter. Then we scaled up the system by considering many either straight or circle swimmers and showed that the active suspension can give rise to non trivial collective motions. For straight swimmers, local alignment can be observed in the presence of the sole hydrodynamic interactions leading to dynamic schools of swimmers swimming in the same directions. Remarkably, interactions between co-rotating circle swimmers lead to the formation of approximately ordered vortices of swimmers, moving on approximately circular trajectories.

The preliminary results on the collective motion of swimmers suggest the directions on which the numerical investigation could be pursued more extensively, also in light of previous results on circle swimmers [131, 133]. In particular, it will be interesting to assess whether and to what extent the structures observed with other model swimmers are model-independent and how the collective dynamics changes with steric interactions. Another interesting direction of investigation is to allow the swimmers to change dynamically their geometry, this can be used to control the swimming direction internally so to the swimmer can steer and direct its motion in a desired direction. Eventually, this can be supplemented by artificial intelligence, e.g. via reinforcement learning [142] so to allow the swimmers to accomplish some single (e.g. reach a target or control dispersion [143, 144, 145]) or collective goal [146] (e.g. swimming in schools). These features can be useful to microrobots design in biomedical applications, to model animal interactions etc.

Part IV

Appendix

Appendix A

A.1 Multiple Scale Analysis

We start from (6.4) with parameters rescaled according to (6.5) and multiple times $(t, T = \epsilon^2 t)$

$$\begin{aligned}
\partial_t x + \epsilon^2 \partial_T x &= \epsilon\alpha e^z \cos(x - t) + \epsilon^2 \upsilon \sin\phi + \epsilon^2 \sigma(\beta + z) \\
\partial_t z + \epsilon^2 \partial_T z &= \epsilon\alpha e^z \sin(x - t) + \epsilon^2 \upsilon \cos\phi - \epsilon^2 \upsilon_g \\
\partial_t \phi + \epsilon^2 \partial_T \phi &= \lambda\epsilon\alpha e^z \cos(x - t + 2\phi) - \epsilon^2 \frac{1}{2\Psi} \sin\phi + \epsilon^2 \frac{\sigma}{2}(1 + \lambda \cos 2\phi).
\end{aligned} \tag{A.1}$$

together with a perturbative expansion of the variables [81]

$$\begin{aligned}
x &= x_0 + \epsilon x_1 + \epsilon^2 x_2 + \dots \\
z &= z_0 + \epsilon z_1 + \epsilon^2 z_2 + \dots \\
\phi &= \phi_0 + \epsilon x_1 + \epsilon^2 \phi_2 + \dots
\end{aligned} \tag{A.2}$$

At order zero, ϵ^0, (A.1), gives

$$\begin{aligned}
\partial_t x_0 = 0 \quad &\Longrightarrow \quad x_0 = X(T) \\
\partial_t z_0 = 0 \quad &\Longrightarrow \quad z_0 = Z(T) \\
\partial_t \phi_0 = 0 \quad &\Longrightarrow \quad \phi_0 = \Phi(T)\,,
\end{aligned} \tag{A.3}$$

i.e. zero-order solutions are function of the slow time T only.

At the order ϵ^1 we have

$$\begin{aligned}
\partial_t x_1 &= \alpha e^Z \cos(X - t) \\
\partial_t z_1 &= \alpha e^Z \sin(X - t) \\
\partial_t \phi_1 &= \alpha\lambda e^Z \cos(X + 2\Phi - t).
\end{aligned} \tag{A.4}$$

Notice that the integral on t over $[0, 2\pi]$ of the right-hand side of each equation (A.4) vanishes (which is the solvability condition) and therefore the solutions are [74]

$$\begin{aligned} x_1 &= -\alpha e^Z \sin(X - t) \\ z_1 &= \alpha e^Z \cos(X - t) \\ \phi_1 &= -\alpha\lambda e^Z \sin(X + 2\Phi - t). \end{aligned} \tag{A.5}$$

Finally, at the order ϵ^2 we have

$$\begin{aligned} &\partial_t x_2 + \partial_T X = \alpha^2 e^{2Z} + \upsilon \sin\Phi + \sigma(\beta + Z) \\ &\partial_t z_2 + \partial_T Z = \upsilon\cos\Phi - \upsilon_g \\ &\partial_t \phi_2 + \partial_T \Phi = \alpha^2\lambda e^{2Z}[\cos(2\Phi) + 2\lambda\sin^2(X - t + 2\Phi)] - \frac{1}{2\Psi}\sin\Phi + \frac{\sigma}{2}(1 + \lambda\cos 2\Phi). \end{aligned} \tag{A.6}$$

At this order, by averaging (A.6) over one period, we obtain the nontrivial solvability conditions (6.6).

A.2 3D model with orientation dependent settling

We now introduce two extensions which improve the mathematical model. The first one is to consider a three-dimensional model, in which the orientation of the swimmers is parametrized by the two angles (θ, ϕ) and therefore

$$\mathbf{p} = (\sin\theta\sin\phi, \cos\theta, \sin\theta\cos\phi)\,. \tag{A.7}$$

The second modification is a more realistic model for the settling velocity which depends on the orientation of the ellipsoidal body:

$$\mathbf{v}_g = -\mathrm{v}_{sm}\left[\hat{\mathbf{k}} + (\mathrm{v}_{sr} - 1)(\hat{\mathbf{k}}\cdot\mathbf{p})\mathbf{p}\right], \tag{A.8}$$

where v_{sm} is the settling velocity in quiescent fluid in the highest drag orientation (i.e. symmetry axis perpendicular to gravity for prolate spheroids and symmetry axis parallel to gravity for oblate spheroids), and v_{sr} is the relative increment of this velocity in the case of lowest drag orientation (and thus $\mathrm{v}_{sr} > 1$). For prolate spheroids we have (see,

e.g., [147])

$$\mathrm{v}_{sm} = \frac{3S\sqrt{\frac{1}{\lambda}-1}}{32\lambda}\left[2\sqrt{\lambda(1+\lambda)} + \sqrt{2}(5\lambda-1)\,\mathrm{arcsinh}\left(\sqrt{\frac{1+\lambda}{1-\lambda}-1}\right)\right] \tag{A.9}$$

$$\mathrm{v}_{sr} = -\frac{2\sqrt{2\lambda(1+\lambda)} + 2(3\lambda+1)\,\mathrm{arcsinh}\left(\sqrt{\frac{1+\lambda}{1-\lambda}-1}\right)}{\sqrt{2\lambda(1+\lambda)} + (5\lambda-1)\,\mathrm{arcsinh}\left(\sqrt{\frac{1+\lambda}{1-\lambda}-1}\right)}, \tag{A.10}$$

where $S = \frac{(\rho_p-\rho)d_p^2 gk}{18\mu\omega}$ and μ is the dynamic viscosity, ρ is the fluid density, ρ_p is the particle's density, d_p is the particle diameter. Note that both v_{sm} and v_{sr} are dimensionless.

The complete model reads:

$$\dot{x} = \alpha e^z \cos(x-t) + \upsilon \sin\phi \sin\theta - \mathrm{v}_{sm}(\mathrm{v}_{sr}-1)\cos\phi\sin\phi\sin^2\theta \tag{A.11}$$

$$\dot{y} = \upsilon\cos\theta - \mathrm{v}_{sm}(\mathrm{v}_{sr}-1)\cos\phi\cos\theta\sin\theta \tag{A.12}$$

$$\dot{z} = \alpha e^z \sin(x-t) + \upsilon\cos\phi\sin\theta - \mathrm{v}_{sm}[1+(\mathrm{v}_{sr}-1)\cos^2\phi\sin^2\theta] \tag{A.13}$$

$$\dot{\phi} = \lambda\alpha e^z\cos(x-t+2\phi) - \frac{1}{2\Psi}\frac{\sin\phi}{\sin\theta} \tag{A.14}$$

$$\dot{\theta} = \lambda\alpha e^z\cos\theta\sin\theta\sin(x-t+2\phi) + \frac{1}{2\Psi}\cos\theta\cos\phi. \tag{A.15}$$

It is again possible to obtain the slow time equations using a multiple scale analysis. Neglecting the equations for X and Y, that are independent of the others, one obtains

$$\partial_T Z = \upsilon\cos\Phi\sin\Theta - \mathrm{v}_{sm}[1+(\mathrm{v}_{sr}-1)\cos^2\Phi\sin^2\Theta] \tag{A.16}$$

$$\partial_T \Phi = \lambda\alpha^2 e^{2Z}(\lambda+\cos(2\Phi)) - \frac{1}{2\Psi}\frac{\sin\Phi}{\sin\Theta} \tag{A.17}$$

$$\partial_T \Theta = \lambda\alpha^2 e^{2Z}\cos\Theta\sin\Theta\sin(2\Phi) + \frac{1}{2\Psi}\cos\Theta\cos\Phi. \tag{A.18}$$

From the third equation we note that a solution is $\cos\theta = 0$ and so $\theta = \pi/2$. Based on the analysis of the 2D case, we expect that a pair of fixed points is on the xz-plane. We remark that $\theta = \pi/2$ is also the stable orientation for neutrally buoyant, non-swimmers [148]. Using $\theta = \pi/2$ in (A.18) we obtain the equation for the fixed points as

$$\upsilon\cos\Phi - \mathrm{v}_{sm}[1+(\mathrm{v}_{sr}-1)\cos^2\Phi] = 0 \tag{A.19}$$

$$\lambda\alpha^2 e^{2Z}(\lambda+\cos(2\Phi)) - \frac{1}{2\Psi}\sin\Phi = 0. \tag{A.20}$$

The first equation gives two real solutions for the angle Φ

$$\Phi^{\pm} = \pm \arccos(A), \quad \text{where} \quad A = \frac{1 - \sqrt{1 - 4q^2(\mathrm{v}_{sr} - 1)}}{2q(\mathrm{v}_{sr} - 1)} \tag{A.21}$$

and $q = \mathrm{v}_{sm}/\upsilon$. The associated values of Z are:

$$Z^{\pm} = \frac{1}{2}\ln\left(\pm\frac{\sqrt{1 - A^2}}{2\Psi\lambda\alpha^2\left(\lambda - 1 + 2A^2\right)}\right). \tag{A.22}$$

The existence domain and the physical observability condition (i.e. whether $Z < 0$) of these fixed points are not trivial, but it can be shown that they never coexist in the same range of parameters and, where they exist, they are both negative (i.e. below the sea level, thus observable).

We can conclude that the 3D case is a natural extension of the 2D one. Indeed, despite the different form of the settling velocity, the fixed points qualitatively agree with the results in section 6.2.2. One can also note that in the formal limit $\mathrm{v}_{sr} \to 1$ (A.22) reduces to (6.13) once the identification $\upsilon_g = \mathrm{v}_s$ is made and v_{sr} and υ_g are considered as independent on λ.

Appendix B

B.1 Stokeslets superposition

Let's start by considering a single sphere with a constant speed $\mathbf{v}$. The velocity field produced, in the very low Re regime, is described by the Stokes equation and leads to the following solution [1]:

$$\mathbf{u} = \frac{3}{4}R\frac{\mathbf{v} + \hat{\mathbf{r}}(\mathbf{v}\cdot\hat{\mathbf{r}})}{r} + \frac{1}{4}R^3\frac{\mathbf{v} - 3\hat{\mathbf{r}}(\mathbf{v}\cdot\hat{\mathbf{r}})}{r^3} \tag{B.1}$$

where $\hat{\mathbf{r}}$ is a unit vector pointing from the centre of the sphere (origin) to a point in space, r is the distance with respect to the origin and R is the radius of the sphere. The previous equation could be rewritten as:

$$\begin{aligned} u_\alpha &= \frac{3}{4}\frac{R}{r}[\mathrm{v}_\alpha + \hat{r}_\alpha(\mathrm{v}_\beta\hat{r}_\beta)] + \frac{1}{4}\frac{R^3}{r^3}[\mathrm{v}_\alpha - 3\hat{r}_\alpha(\mathrm{v}_\beta\hat{r}_\beta)] \\ &= \frac{1}{4}\left(\frac{3R}{r} + \frac{R^3}{r^3}\right)\mathrm{v}_\alpha + \frac{3}{4}\hat{r}_\alpha(\mathrm{v}_\beta\hat{r}_\beta)\left(\frac{R}{r} - \frac{R^3}{r^3}\right) \end{aligned} \tag{B.2}$$

where the Greek subscript stands for spatial components. On the surface of the sphere $r = R$ the no slip condition $u_\alpha = \mathrm{v}_\alpha$ is enforced. The fluid field around a dumbbell swimmer is approximately given by the superposition of two solutions having the same form of (B.2). This approximation clearly breaks down on the surface of the beads because it violates the no-slip condition, but this is not relevant to our numerical model because the beads have only an effective radius and their surface is not resolved. Carrying on with this approximation, we denote by v_i^* the speed of the $i-$th sphere if it were isolated. Taking into account the disturbance induced by the other bead, one gets a linear relation

between these speeds and the ones resulting from hydrodynamic interaction, formally

$$\begin{cases} \mathrm{v}_{1,\alpha} = \mathrm{v}^*_{1,\alpha} + \mathrm{v}^*_{2,\alpha} S_\alpha \\ \mathrm{v}_{2,\alpha} = \mathrm{v}^*_{2,\alpha} + \mathrm{v}^*_{1,\alpha} S_\alpha, \end{cases} \tag{B.3}$$

where 1 and 2 are the indices of the flagellum and body beads respectively and S is a geometric factor which can be computed from (B.2). S appears in a symmetric way in both equations because the beads are identical. Let us focus, as example, on the horizontal dynamics, with a dumbbell that is swimming along the x-axis with $\mathrm{v}_x \neq 0, \mathrm{v}_y = 0, \mathrm{v}_z = 0$. The horizontal dynamics is characterized by $\hat{r}_x = 1, \hat{r}_y = 0, \hat{r}_z = 0$. Thus, the horizontal component of the velocity is

$$u_x = \frac{1}{4}\left(\frac{3R}{r} + \frac{R^3}{r^3}\right)\mathrm{v}_x + \frac{3}{4}\hat{r}_x(\mathrm{v}_x\hat{r}_x)\left[\frac{R}{r} - \frac{R^3}{r^3}\right] \tag{B.4}$$

from which

$$u_x = \mathrm{v}_x\left[\frac{3R}{2r} - \frac{R^3}{2r^3}\right] \quad \rightarrow \quad S_x = \left[\frac{3R}{2r} - \frac{R^3}{2r^3}\right] \tag{B.5}$$

on the other hand y, z-component of the fluid:

$$u_{y,z} = \frac{3}{4}\hat{r}_{y,z}\hat{r}_x\mathrm{v}_x\left[\frac{R}{r} - \frac{R^3}{r^3}\right] \quad \rightarrow \quad S_{y,z} = 0. \tag{B.6}$$

Using v_α known from the numerical computation, equations (B.3) can be inverted obtain the unknown velocities v^*, which can then be plugged into (B.2) to compute the disturbance field. Thus this two Stokes solutions are superposed and compared with the numerical velocity field in order to fit the effective radius R of each sphere.

B.2 Implementation of inextensibility and rigidity

Here we detail how inextensibility and rigidity are imposed and used to fix the model parameters. Consider the 2-beads model discussed in the introduction. The inextensibility condition is:

$$|\mathbf{x}_2 - \mathbf{x}_1| = \text{const} \quad \Rightarrow \quad \frac{d}{dt}|\mathbf{x}_2 - \mathbf{x}_1|^2 = 0 \tag{B.7}$$

from which expanding the square $\mathbf{x}_2 - \mathbf{x}_1$ and considering further derivation we obtain a condition on accelerations

$$(\dot{\mathbf{v}}_2 - \dot{\mathbf{v}}_1) \cdot \mathbf{n} = -\frac{|\mathbf{v}_2 - \mathbf{v}_1|^2}{|\mathbf{x}_2 - \mathbf{x}_1|}. \tag{B.8}$$

In the last equation we have introduced the unit vector $\mathbf{n} = (\mathbf{x}_2 - \mathbf{x}_1)/|\mathbf{x}_2 - \mathbf{x}_1|$. Equation (B.8) is trivial for the 1D case, where a zero relative acceleration leads to a zero relative velocity difference. From this point on, the simplified notation $\mathbf{u}_i = \mathbf{u}(\mathbf{x}_i)$ is used to denote the fluid velocity in the position of the i-th bead.

From the (B.8) and (8.7) we get:

$$\Lambda = \frac{1}{2}\left[\frac{|\mathbf{v}_2 - \mathbf{v}_1|^2}{|\mathbf{x}_2 - \mathbf{x}_1|} - f_p - \beta[\mathbf{v}_2 - \mathbf{u}_2] \cdot \mathbf{n}\right] \tag{B.9}$$

that is the module of the tension. From (8.7) it is easy to obtain the stationary state $f_p\mathbf{n} = \beta(\mathbf{v}_2 - \mathbf{u}_2)$ when $\dot{\mathbf{v}}_1 = \dot{\mathbf{v}}_2 = 0$. Numerical simulations of the model here introduced, with the constrain expressed by (B.9), were carried out on a dumbbell $0.5h$ long (where h is the grid step) in a 2D Kolmogorov flow of period 2π with velocity $\mathbf{u} = (\cos(z), 0, 0)$ and we observed a maximum relative deviation of the length of each rod of order 10^{-6}, which validates the model.

The model can be easily extended to the 3-beads swimmer. We define two unit vectors $\mathbf{n}_1$ e $\mathbf{n}_2$ that point respectively from the tail to the central bead and from the central to the head bead. This model introduces a new degree of freedom that is the angle ϕ between the two unit vectors (see Fig. 8.1(c) in the main text). To maintain a rigid shape we need this angle to relax to a fixed value ϕ_0. We define the unit vectors $\mathbf{t}_1$ and $\mathbf{t}_3$ perpendicular to $\mathbf{n}_1$ and $\mathbf{n}_2$, respectively, such that they lie in the plane defined by the swimmer (Fig.8.2), in formulae:

$$\mathbf{t}_1 = \frac{\mathbf{n}_2 - \cos\phi\mathbf{n}_1}{|\mathbf{n}_2 - \cos\phi\mathbf{n}_1|} \tag{B.10}$$

$$\mathbf{t}_3 = \frac{-\mathbf{n}_1 + \cos\phi\mathbf{n}_2}{|-\mathbf{n}_1 + \cos\phi\mathbf{n}_2|} \tag{B.11}$$

We introduce $\mathbf{g}_1$ along $\mathbf{t}_1$, $\mathbf{g}_3$ along $\mathbf{t}_3$, and $\mathbf{g}_2$ such that $\mathbf{g}_2 = -(\mathbf{g}_1 + \mathbf{g}_3) = -g(\mathbf{t}_1 + \mathbf{t}_3)$. In the last equality we suppose that $|\mathbf{g}_1| = |\mathbf{g}_3| = g$. At each time step t we compute g as

$$g = -a(\phi - \phi_0), \tag{B.12}$$

where a is a constant setting the stiffness of the spring which keeps ϕ close to ϕ_0. The

equations of the dynamics for a generic angle ϕ are:

$$\begin{cases} \dot{\mathbf{v}}_1 = f_p \mathbf{n}_1 + \Lambda_{12}\mathbf{n}_1 + g\mathbf{t}_1 \\ \dot{\mathbf{v}}_2 = -\Lambda_{12}\mathbf{n}_1 + \Lambda_{23}\mathbf{n}_2 - \beta(\mathbf{v}_2 - \mathbf{u}_2) + g\mathbf{t}_2 \\ \dot{\mathbf{v}}_3 = -\Lambda_{23}\mathbf{n}_2 - \beta(\mathbf{v}_3 - \mathbf{u}_3) + g\mathbf{t}_3 \end{cases} \tag{B.13}$$

where Λ_{12} and Λ_{23} are the tension forces that guarantee the inextensibility. The condition (B.8) is now applied on each rod and we obtain:

$$\Lambda_{23} = \left[-\frac{|\mathbf{v}_2 - \mathbf{v}_1|^2}{|\mathbf{x}_2 - \mathbf{x}_1|} - \frac{2}{\cos\phi}\frac{|\mathbf{v}_3 - \mathbf{v}_2|^2}{|\mathbf{x}_3 - \mathbf{x}_2|} + f_p - \beta(\mathbf{v}_2 - \mathbf{u}_2)\cdot\left(\frac{2\mathbf{n}_2}{\cos\phi} - \mathbf{n}_1\right) + \frac{2\beta}{\cos\phi}(\mathbf{v}_3 - \mathbf{u}_3)\cdot\mathbf{n}_2 - g_2\mathbf{t}_2\cdot\left(\frac{-2\mathbf{n}_2}{\cos\phi} + \mathbf{n}_1\right)\right]\frac{1}{\cos\phi - \frac{4}{\cos\phi}}$$

$$\Lambda_{12} = \left[-\frac{|\mathbf{v}_3 - \mathbf{v}_2|^2}{|\mathbf{x}_3 - \mathbf{x}_2|} - \frac{2}{\cos\phi}\frac{|\mathbf{v}_2 - \mathbf{v}_1|^2}{|\mathbf{x}_2 - \mathbf{x}_1|} + \frac{2f_p}{\cos\phi} + \beta(\mathbf{v}_2 - \mathbf{u}_2)\cdot\left(\frac{2\mathbf{n}_1}{\cos\phi} - \mathbf{n}_2\right) + \beta(\mathbf{v}_3 - \mathbf{u}_3)\cdot\mathbf{n}_2 - g_2\mathbf{t}_2\cdot\left(\frac{2\mathbf{n}_1}{\cos\phi} - \mathbf{n}_2\right)\right]\frac{1}{\cos\phi - \frac{4}{\cos\phi}}$$

B.3 The limit to Jeffery's model of a rod

In this appendix we show that the dynamics of a short dumbbell is well described by Jeffery's equation for an infinitely thin rod. Consider a dumbbell with fixed length L and particles $\mathbf{x}_1$ and $\mathbf{x}_2$. Assume the dynamics is Stokesian with relaxation time τ. The equations of motion are

$$\begin{cases} \dot{\mathbf{v}}_1 = -\dfrac{\mathbf{v}_1 - \mathbf{u}_1}{\tau} - \Lambda\mathbf{n} \\ \dot{\mathbf{v}}_2 = -\dfrac{\mathbf{v}_2 - \mathbf{u}_2}{\tau} + \Lambda\mathbf{n} \end{cases} \tag{B.14}$$

where $\mathbf{u}_i = \mathbf{u}(\mathbf{x}_i)$ is the fluid's velocity at the i-th particle and $\mathbf{n} = \mathbf{L}/L$, with $\mathbf{L} = \mathbf{x}_2 - \mathbf{x}_1$. The modulus of the rod's tension Λ is obtained by imposing inextensibility $dL^2/dt = 0$ (see (B.7)). Further derivation to obtain a condition on accelerations gives

$$\ddot{\mathbf{L}}\cdot\mathbf{L} + |\dot{\mathbf{L}}|^2 = 0, \tag{B.15}$$

where $\dot{\mathbf{L}} = \mathbf{v}_2 - \mathbf{v}_1$ and $\ddot{\mathbf{L}} = \dot{\mathbf{v}}_2 - \dot{\mathbf{v}}_1$. Defining $\mathbf{w}_i = \mathbf{v}_i - \mathbf{u}_i$, we get from (B.14)

$$\ddot{\mathbf{L}} = -\frac{\mathbf{w}_2 - \mathbf{w}_1}{\tau} + 2\Lambda\mathbf{n} \tag{B.16}$$

and from (B.15) and the definition of $\mathbf{n}$

$$\Lambda = -\frac{|\dot{\mathbf{L}}|^2}{2L} + \frac{\mathbf{w}_2 - \mathbf{w}_1}{2\tau} \cdot \mathbf{n}. \tag{B.17}$$

Finally, the equations of motion for the positions of the dumbbell's beads are

$$\begin{cases} \dot{\mathbf{v}}_1 = -\dfrac{\mathbf{w}_1}{\tau} + \dfrac{|\mathbf{v}_2 - \mathbf{v}_1|^2}{2L}\mathbf{n} - \dfrac{\mathbf{w}_2 - \mathbf{w}_1}{2\tau} \cdot \mathbf{n} \otimes \mathbf{n} \\ \dot{\mathbf{v}}_2 = -\dfrac{\mathbf{w}_2}{\tau} - \dfrac{|\mathbf{v}_2 - \mathbf{v}_1|^2}{2L}\mathbf{n} + \dfrac{\mathbf{w}_2 - \mathbf{w}_1}{2\tau} \cdot \mathbf{n} \otimes \mathbf{n}. \end{cases} \tag{B.18}$$

The latter equations are essentially the same obtained when imposing no-slip conditions on the two spheres via an immersed boundary method. If we now take the overdamped (or Re = 0) limit $\tau \to 0$, we get

$$\begin{cases} 0 = -\mathbf{w}_1 - \dfrac{\mathbf{w}_2 - \mathbf{w}_1}{2} \cdot \mathbf{n} \otimes \mathbf{n} \\ 0 = -\mathbf{w}_2 + \dfrac{\mathbf{w}_2 - \mathbf{w}_1}{2} \cdot \mathbf{n} \otimes \mathbf{n}. \end{cases} \tag{B.19}$$

By summing the two equations one gets $\mathbf{w}_1 = -\mathbf{w}_2$, and by substituting this relation into each equation

$$(\mathbb{I} - \mathbf{n} \otimes \mathbf{n})\mathbf{w}_{1,2} = 0. \tag{B.20}$$

Since $(\mathbf{v}_2 - \mathbf{v}_1) \cdot \mathbf{n} = 0$ because of inextensibility, we can take the difference of (B.20) for $\mathbf{w}_2$ and $\mathbf{w}_1$ and get

$$\dot{\mathbf{L}} = (\mathbb{I} - \mathbf{n} \otimes \mathbf{n})(\mathbf{u}_2 - \mathbf{u}_1). \tag{B.21}$$

Now, since $\dot{\mathbf{n}} = (\mathbb{I} - \mathbf{n} \otimes \mathbf{n})\dot{\mathbf{L}}/L$, one gets

$$\dot{\mathbf{n}} = \frac{1}{L}(\mathbb{I} - \mathbf{n} \otimes \mathbf{n})(\mathbb{I} - \mathbf{n} \otimes \mathbf{n})(\mathbf{u}_2 - \mathbf{u}_1) = \frac{1}{L}(\mathbb{I} - \mathbf{n} \otimes \mathbf{n})(\mathbf{u}_2 - \mathbf{u}_1) \tag{B.22}$$

with the last equality stemming from the idempotence of the projector. If the dumbbell's length is very small we can write $\mathbf{u}_2 - \mathbf{u}_1 = \nabla\mathbf{u}\mathbf{n}L + O(L^2)$, so we get to first order in L

$$\dot{\mathbf{n}} = (\mathbb{I} - \mathbf{n} \otimes \mathbf{n})\nabla\mathbf{u}\mathbf{n}. \tag{B.23}$$

The latter is Jeffery's equation [4] with elongation parameter $\lambda = 1$. Indeed Jeffery's equation can be written as

$$\dot{\mathbf{n}} = \mathbb{O}\mathbf{n} + \lambda\mathbb{S}(\mathbb{I} - \mathbf{n} \otimes \mathbf{n})\mathbf{n} \tag{B.24}$$

with $\mathbb{O}$ and $\mathbb{S}$ the antisymmetric and symmetric part of the velocity gradient tensor $\nabla\mathbf{u}$, respectively. Because of symmetry $\mathbb{O}\mathbf{n} = (\mathbb{I} - \mathbf{n} \otimes \mathbf{n})\mathbb{O}\mathbf{n}$ so for $\lambda = 1$ one can reconstruct the gradients and obtain (B.23).

Bibliography

[1] Lev Davidovich Landau and Evgenii Mikhailovich Lifshitz. *Fluid Mechanics: Landau and Lifshitz: Course of Theoretical Physics, Volume 6*, volume 6. Elsevier, Oxford, 1987.

[2] David Saintillan. Rheology of active fluids. *Annual review of fluid mechanics*, 50(1):563–592, 2018.

[3] Saverio E Spagnolie and Eric Lauga. Hydrodynamics of self-propulsion near a boundary: predictions and accuracy of far-field approximations. *Journal of Fluid Mechanics*, 700:105–147, 2012.

[4] George Barker Jeffery. *Proceedings of the Royal Society of London. Series A, Containing papers of a mathematical and Phys. character*, 102(715):161–179, 1922.

[5] Daphne Klotsa. As above, so below, and also in between: mesoscale active matter in fluids. *Soft matter*, 15(44):8946–8950, 2019.

[6] Edward M Purcell. Life at low reynolds number. In *Physics and our world: reissue of the proceedings of a symposium in honor of Victor F Weisskopf*, pages 47–67. World Scientific, 2014.

[7] Brian Chan. *Bio-inspired fluid locomotion*. PhD thesis, Massachusetts Institute of Technology, Department of Mechanical Engineering, 2009.

[8] Tian Qiu, Tung-Chun Lee, Andrew G Mark, Konstantin I Morozov, Raphael Münster, Otto Mierka, Stefan Turek, Alexander M Leshansky, and Peer Fischer.

Swimming by reciprocal motion at low reynolds number. *Nature communications*, 5(1):5119, 2014.

[9] Ali Najafi and Ramin Golestanian. Simple swimmer at low reynolds number: Three linked spheres. *Physical Review E—Statistical, Nonlinear, and Soft Matter Physics*, 69(6):062901, 2004.

[10] Eric Lauga. *The fluid dynamics of cell motility*, volume 62. Cambridge University Press, 2020.

[11] Shahid Khan and Jonathan M Scholey. Assembly, functions and evolution of archaella, flagella and cilia. *Current Biology*, 28(6):R278–R292, 2018.

[12] Cathy Fisch and Pascale Dupuis-Williams. Ultrastructure of cilia and flagella–back to the future! *Biology of the Cell*, 103(6):249–270, 2011.

[13] Farners Amargant i Riera, Montserrat Barragan, Rita Vassena, and Isabelle Vernos. Insights of the tubulin code in gametes and embryos: from basic research to potential clinical applications in humans. *Biol Reprod. 2019; 100 (3): 575-589*, 2019.

[14] Christopher Brennen and Howard Winet. Fluid mechanics of propulsion by cilia and flagella. *Annual Review of Fluid Mechanics*, 9(1):339–398, 1977.

[15] Geoffrey Ingram Taylor. Analysis of the swimming of microscopic organisms. *Proceedings of the Royal Society of London. Series A. Mathematical and Physical Sciences*, 209(1099):447–461, 1951.

[16] Eamonn A Gaffney, Hermes Gadêlha, David J Smith, John R Blake, and Jackson C Kirkman-Brown. Mammalian sperm motility: observation and theory. *Annual Review of Fluid Mechanics*, 43(1):501–528, 2011.

[17] Michael James Lighthill. On the squirming motion of nearly spherical deformable bodies through liquids at very small reynolds numbers. *Communications on pure and applied mathematics*, 5(2):109–118, 1952.

[18] John R Blake. A spherical envelope approach to ciliary propulsion. *Journal of Fluid Mechanics*, 46(1):199–208, 1971.

[19] Timothy J Pedley. Spherical squirmers: models for swimming micro-organisms. *IMA Journal of Applied Mathematics*, 81(3):488–521, 2016.

[20] Douglas R Brumley, Marco Polin, Timothy J Pedley, and Raymond E Goldstein. Metachronal waves in the flagellar beating of volvox and their hydrodynamic origin. *Journal of the Royal Society Interface*, 12(108):20141358, 2015.

[21] Erik Theodoor Buitenhuis, William KW Li, Daniel Vaulot, MW Lomas, MR Landry, Frédéric Partensky, DM Karl, O Ulloa, L Campbell, Stéphan Jacquet, et al. Picophytoplankton biomass distribution in the global ocean. *Earth System Science Data*, 4(1):37–46, 2012.

[22] C Zhan, G Sardina, E Lushi, and L Brandt. Accumulation of motile elongated micro-organisms in turbulence. *J. Fluid Mech.*, 739:22, 2013.

[23] N Pujara, MAR Koehl, and EA Variano. Rotations and accumulation of ellipsoidal microswimmers in isotropic turbulence. *J. Fluid Mech.*, 838:356, 2018.

[24] M Borgnino, K Gustavsson, F De Lillo, G Boffetta, M Cencini, and B Mehlig. Alignment of Nonspherical Active Particles in Chaotic Flows. *Phys. Rev. Lett.*, 123:138003, 2019.

[25] M Borgnino, G Boffetta, M Cencini, F De Lillo, and K Gustavsson. *Phys. Rev. Fluids*, 7(7):074603, 2022.

[26] C Torney and Z Neufeld. Transport and Aggregation of Self-Propelled Particles in Fluid Flows. *Phys. Rev. Lett.*, 99(7):078101, 2007.

[27] N Khurana, J Blawzdziewicz, and N T Ouellette. Reduced Transport of Swimming Particles in Chaotic Flow due to Hydrodynamic Trapping. *Phys. Rev. Lett*, 106:198104, 2011.

[28] N Khurana and N T Ouellette. Interactions between active particles and dynamical structures in chaotic flow. *Phys. Fluids*, 24:091902, 2012.

[29] A Sokolov and I S Aranson. Rapid expulsion of microswimmers by a vortical flow. *Nat. Commun.*, 7:11114, 2016.

[30] S A Berman, J Buggeln, D A Brantley, K A Mitchell, and T H Solomon. Transport barriers to self-propelled particles in fluid flows. *Phys. Rev. Fluids*, 6(1):L012501, 2021.

[31] S A Berman and K A Mitchell. Trapping of swimmers in a vortex lattice. *Chaos*, 30(6):063121, 2020.

[32] JA Arguedas-Leiva and M Wilczek. Microswimmers in an axisymmetric vortex flow. *New J. Phys.*, 22:053051, 2020.

[33] Ivan Tanasijević and Eric Lauga. Microswimmers in vortices: dynamics and trapping. *Soft Matter*, 18:8931, 2022.

[34] Roberto Rusconi, Jeffrey S Guasto, and Roman Stocker. Bacterial transport suppressed by fluid shear. *Nat. Phys.*, 10(3):212, 2014.

[35] Andreas Zöttl and Holger Stark. Nonlinear dynamics of a microswimmer in poiseuille flow. *Phys. Rev. Lett.*, 108(21):218104, 2012.

[36] Andreas Zöttl and Holger Stark. Periodic and quasiperiodic motion of an elongated microswimmer in poiseuille flow. *Eur. Phys. J. E*, 36(1):1, 2013.

[37] Gaspard Junot, Nuris Figueroa-Morales, Thierry Darnige, Anke Lindner, Rodrigo Soto, Harold Auradou, and Eric Clément. Swimming bacteria in poiseuille flow: The quest for active bretherton-jeffery trajectories. *EPL*, 126(4):44003, 2019.

[38] Rachel N Bearon and Andrew L Hazel. The trapping in high-shear regions of slender bacteria undergoing chemotaxis in a channel. *J. Fluid Mech.*, 771:R3, 2015.

[39] Simona Colabrese, Kristian Gustavsson, Antonio Celani, and Luca Biferale. Flow navigation by smart microswimmers via reinforcement learning. *Phys. Rev. Lett.*, 118:158004, 2017.

[40] Jingran Qiu, Navid Mousavi, Kristian Gustavsson, Chunxiao Xu, Bernhard Mehlig, and Lihao Zhao. Navigation of micro-swimmers in steady flow: The importance of symmetries. *J. Fluid Mech.*, 932:A10, 2022.

[41] Rémi Monthiller, Aurore Loisy, Mimi AR Koehl, Benjamin Favier, and Christophe Eloy. Surfing on turbulence: A strategy for planktonic navigation. *Phys. Rev. Lett.*, 129(6):064502, 2022.

[42] Anupam Sengupta, Francesco Carrara, and Roman Stocker. Phytoplankton can actively diversify their migration strategy in response to turbulent cues. *Nature*, 543(7646):555, 2017.

[43] Kevin T Du Clos, Lee Karp-Boss, Tracy A Villareal, and Brad J Gemmell. Coscinodiscus wailesii mutes unsteady sinking in dark conditions. *Biol. Lett.*, 15(3):20180816, 2019.

[44] Nimish Pujara, Kevin T Du Clos, Stephanie Ayres, Evan A Variano, and Lee Karp-Boss. Measurements of trajectories and spatial distributions of diatoms (Coscinodiscus spp.) at dissipation scales of turbulence. *Exp. Fluids*, 62:149, 2021.

[45] Rebekka E Breier, Cristian C Lalescu, Devin Waas, Michael Wilczek, and Marco G Mazza. Emergence of phytoplankton patchiness at small scales in mild turbulence. *Proc. Natl. Acad. Sci. U.S.A.*, 115(48):12112, 2018.

[46] John O Kessler. Hydrodynamic focusing of motile algal cells. *Nature*, 313(5999):218, 1985.

[47] Timothy John Pedley and J. O. Kessler. The orientation of spheroidal microorganisms swimming in a flow field. *Proc. R. Soc. Lond.*, 231(1262):47, jun 1987.

[48] Graeme J. Thorn and Rachel N. Bearon. Transport of spherical gyrotactic organisms in general three-dimensional flow fields. *Phys. Fluids*, 22(4):041902, 04 2010.

[49] Massimo Cencini, Guido Boffetta, Matteo Borgnino, and Filippo De Lillo. Gyrotactic phytoplankton in laminar and turbulent flows: a dynamical systems approach. *Eur. Phys. J. E*, 42(3):1, 2019.

[50] R. N. Bearon and W. M. Durham. Elongation enhances migration through hydrodynamic shear. *Phys. Rev. Fluids*, 8:033101, Mar 2023.

[51] William M Durham, Eric Climent, Michael Barry, Filippo De Lillo, Guido Boffetta, Massimo Cencini, and Roman Stocker. Turbulence drives microscale patches of motile phytoplankton. *Nat. Commun.*, 4:1, 2013.

[52] Filippo De Lillo, Massimo Cencini, William M Durham, Michael Barry, Roman Stocker, Eric Climent, and Guido Boffetta. Turbulent fluid acceleration generates clusters of gyrotactic microorganisms. *Phys. Rev. Lett.*, 112(4):044502, 2014.

[53] K Gustavsson, F Berglund, PR Jonsson, and B Mehlig. Preferential sampling and small-scale clustering of gyrotactic microswimmers in turbulence. *Phys. Rev. Lett.*, 116(10):108104, 2016.

[54] Zehua Liu, Linfeng Jiang, and Chao Sun. Accumulation and alignment of elongated gyrotactic swimmers in turbulence. *Phys. Fluids*, 34:033303, 2022.

[55] Jingran Qiu, Cristian Marchioli, and Lihao Zhao. A review on gyrotactic swimmers in turbulent flows. *Acta Mech. Sin.*, 38(8):722323, 2022.

[56] W M Durham, J O Kessler, and R Stocker. Disruption of vertical motility by shear triggers formation of thin phytoplankton layers. *Science*, 323:1067, 2009.

[57] Michael T Barry, Roberto Rusconi, Jeffrey S Guasto, and Roman Stocker. Shear-induced orientational dynamics and spatial heterogeneity in suspensions of motile phytoplankton. *J. R. Soc. Interface*, 12(112):20150791, 2015.

[58] William M Durham and Roman Stocker. Thin phytoplankton layers: characteristics, mechanisms, and consequences. *Annu. Rev. Mar. Sci.*, 4:177, 2012.

[59] Jeanette D Wheeler, Eleonora Secchi, Roberto Rusconi, and Roman Stocker. Not just going with the flow: the effects of fluid flow on bacteria and plankton. *Annu. Rev. Cell Dev. Biol.*, 35:21, 2019.

[60] Margaret M Dekshenieks, Percy L Donaghay, James M Sullivan, Jan EB Rines, Thomas R Osborn, and Michael S Twardowski. Temporal and spatial occurrence

of thin phytoplankton layers in relation to physical processes. *Marine Ecology Progress Series*, 223:61–71, 2001.

[61] Mark A Moline, Kelly J Benoit-Bird, Ian C Robbins, Maddie Schroth-Miller, Chad M Waluk, and Brian Zelenke. Integrated measurements of acoustical and optical thin layers ii: Horizontal length scales. *Continental Shelf Research*, 30(1):29–38, 2010.

[62] James H Churnside and Richard D Marchbanks. Subsurface plankton layers in the arctic ocean. *Geophysical Research Letters*, 42(12):4896–4902, 2015.

[63] Peter Koefoed Bjørnsen and Torkel Gissel Nielsen. Decimeter scale heterogeneity in the plankton during a pycnocline bloom of gyrodinium aureolum. *Marine Ecology Progress Series*, pages 263–267, 1991.

[64] Ira M Cohen and Pijush K Kundu. *Fluid mechanics*. Elsevier, 2004.

[65] AM Roberts. Mechanisms of gravitaxis in chlamydomonas. *The Biological Bulletin*, 210(2):78–80, 2006.

[66] George Barker Jeffery. The motion of ellipsoidal particles immersed in a viscous fluid. *Proc. R. Soc. Lond.*, 102(715):161, nov 1922.

[67] Ramón Margalef. Turbulence and marine life. 1997.

[68] Pijush K Kundu, Ira M Cohen, David R Dowling, and Jesse Capecelatro. *Fluid mechanics*. Elsevier, 2024.

[69] Robert G Dean and Robert A Dalrymple. *Water wave mechanics for engineers and scientists*, volume 2. world scientific publishing company, 1991.

[70] Blair Kinsman. *Wind waves: their generation and propagation on the ocean surface*. Courier Corporation, 1984.

[71] Steven A Hughes. *Physical models and laboratory techniques in coastal engineering*, volume 7. World Scientific, 1993.

[72] Cristian Marchioli, Harshit Bhatia, Gaetano Sardina, Luca Brandt, and Alfredo Soldati. Role of large-scale advection and small-scale turbulence on vertical migration of gyrotactic swimmers. *Phys. Rev. Fluids*, 4(12):124304, 2019.

[73] Maryam Mashayekhpour, Cristian Marchioli, Salvatore Lovecchio, Ebrahim Nemati Lay, and Alfredo Soldati. Wind effect on gyrotactic micro-organism surfacing in free-surface turbulence. *Adv. Water Resour.*, 129:328, 2019.

[74] Kunlin Ma, Nimish Pujara, and Jean-Luc Thiffeault. Reaching for the surface: Spheroidal microswimmers in surface gravity waves. *Phys. Rev. Fluids*, 7(1):014310, 2022.

[75] F. Santamaria, G. Boffetta, M. M. Afonso, A. Mazzino, M. Onorato, and D. Pugliese. Stokes drift for inertial particles transported by water waves. *Europhys. Lett.*, 102:14003, 2013.

[76] M. H. DiBenedetto and N. T. Ouellette. Preferential orientation of spheroidal particles in wavy flow. *J. Fluid Mech.*, 856:850, 2018.

[77] T S van den Bremer, C Whittaker, R Calvert, A Raby, and P H Taylor. Experimental study of particle trajectories below deep-water surface gravity wave groups. *J. Fluid Mech.*, 879:168, 2019.

[78] R. Calvert, M.L. McAllister, C. Whittaker, A. Raby, A.G.L. Borthwick, and T.S. van den Bremer. A mechanism for the increased wave-induced drift of floating marine litter. *J. Fluid Mech.*, 915:A73, 2021.

[79] M H DiBenedetto, L K Clark, and N Pujara. Enhanced settling and dispersion of inertial particles in surface waves. *J. Fluid Mech.*, 936:A38, 2022.

[80] Omar H. Shemdin. Wind-generated current and phase speed of wind waves. *J. Phys. Oceanogr.*, 2(4):411, 1972.

[81] Carl M Bender, Steven Orszag, and Steven A Orszag. *Advanced mathematical methods for scientists and engineers I: Asymptotic methods and perturbation theory*, volume 1. Springer Science & Business Media, 1999.

[82] G. G. Stokes. On the theory of oscillatory waves. *Trans. Camb. Philos. Soc.*, 8:441, 1847.

[83] Gerald Beresford Whitham. *Linear and nonlinear waves*. John Wiley & Sons, 2011.

[84] Salvatore Lovecchio, Eric Climent, Roman Stocker, and William M Durham. Chain formation can enhance the vertical migration of phytoplankton through turbulence. *Sci. Adv.*, 5(10):eaaw7879, 2019.

[85] Chiang C Mei. *The applied dynamics of ocean surface waves*, volume 1. World scientific, 1989.

[86] Stephen O'Malley and Martin Bees. The orientation of swimming biflagellates in shear flows. *Bull. Math. Biol.*, 74:232, 07 2011.

[87] S. A. Thorpe. *An Introduction to Ocean Turbulence*. Cambridge University Press, 2007.

[88] Thomas Kiørboe. *ASLO Web Lectures*, 1(2):1–91, 2009.

[89] Jens Elgeti, Roland G Winkler, and Gerhard Gompper. *Reports on Progress in Physics*, 78(5):056601, 2015.

[90] Ben Wang, Kostas Kostarelos, Bradley J Nelson, and Li Zhang. *Advanced Materials*, 33(4):2002047, 2021.

[91] Bernard Bonnard, Monique Chyba, Jéremy Rouot, and Daisuke Takagi. *Pacific Journal of Mathematics for Industry*, 10:1–27, 2018.

[92] Simona Colabrese, Kristian Gustavsson, Antonio Celani, and Luca Biferale. *Phys. Rev. Letters*, 118(15):158004, 2017.

[93] M Cristina Marchetti, Jean-François Joanny, Sriram Ramaswamy, Tanniemola B Liverpool, Jacques Prost, Madan Rao, and R Aditi Simha. *Rev.s of Modern Physics*, 85(3):1143, 2013.

[94] Knut Drescher, Raymond E Goldstein, Nicolas Michel, Marco Polin, and Idan Tuval. *Phys. Rev. Letters*, 105(16):168101, 2010.

[95] Knut Drescher, Jörn Dunkel, Luis H Cisneros, Sujoy Ganguly, and Raymond E Goldstein. *Proceedings of the National Academy of Sciences*, 108(27):10940–10945, 2011.

[96] Roberto Di Leonardo, Luca Angelani, Dario Dell'Arciprete, Giancarlo Ruocco, Valerio Iebba, Serena Schippa, Maria Pia Conte, Francesco Mecarini, Francesco De Angelis, and Enzo Di Fabrizio. *Proceedings of the National Academy of Sciences*, 107(21):9541–9545, 2010.

[97] M Carlson, SL Seyler, and S Pressé. *BioRxiv*, pages 2020–11, 2020.

[98] Eric Lauga and Thomas R Powers. *Reports on Progress in Physics*, 72(9):096601, 2009.

[99] Kristian Gustavsson, Luca Biferale, Antonio Celani, and Simona Colabrese. *Eur. Phys. J. E*, 40:1–6, 2017.

[100] Eric Lauga. *Annual Rev. of Fluid Mechanics*, 48:105–130, 2016.

[101] Maximilian Seyrich, Zahra Alirezaeizanjani, Carsten Beta, and Holger Stark. *New Journal of Physics*, 20(10):103033, 2018.

[102] Anders Andersen, Navish Wadhwa, and Thomas Kiørboe. *Phys. Rev. E*, 91(4):042712, 2015.

[103] Sergio Chibbaro, Astrid Decoene, Sebastien Martin, and Fabien Vergnet. *Phys. Rev. Fluids*, 6(1):013104, 2021.

[104] Charu Datt and Gwynn J Elfring. *Phys. Rev. Letters*, 123(15):158006, 2019.

[105] Christian Hoell, Hartmut Löwen, and Andreas M Menzel. *The Journal of Chemical Physics*, 149(14), 2018.

[106] Arne W Zantop and Holger Stark. *Soft Matter*, 18(33):6179–6191, 2022.

[107] Jun Huang and Zhi-Gang Shao. *Eur. Phys. J. E*, 47(2):11, 2024.

[108] Enkeleida Lushi and Charles S Peskin. *Computers & Structures*, 122:239–248, 2013.

[109] Juan P Hernandez-Ortiz, Christopher G Stoltz, and Michael D Graham. *Phys. Rev. Letters*, 95(20):204501, 2005.

[110] Juan P Hernandez-Ortiz, Patrick T Underhill, and Michael D Graham. *Journal of Physics: Condensed Matter*, 21(20):204107, 2009.

[111] Akira Furukawa, Davide Marenduzzo, and Michael E Cates. *Phys. Rev. E*, 90(2):022303, 2014.

[112] Vitaliy Gyrya, Igor S Aranson, Leonid V Berlyand, and Dmitry Karpeev. *Bulletin of Mathematical Biology*, 72:148–183, 2010.

[113] M Cavaiola and A Mazzino. *Physics of Fluids*, 33(5), 2021.

[114] M Cavaiola. *Physics of Fluids*, 34(2), 2022.

[115] Benjamin M Friedrich and Frank Jülicher. Steering chiral swimmers along noisy helical paths. *Physical review letters*, 103(6):068102, 2009.

[116] Ting-Wei Su, Inkyum Choi, Jiawen Feng, Kalvin Huang, Euan McLeod, and Aydogan Ozcan. Sperm trajectories form chiral ribbons. *Scientific reports*, 3(1):1664, 2013.

[117] Charles S Peskin. *Acta Numerica*, 11:479–517, 2002.

[118] Charles S Peskin. *Journal of Computational Physics*, 10(2):252–271, 1972.

[119] Charles S Peskin. *Journal of Computational Physics*, 25(3):220–252, 1977.

[120] Charles S Peskin and David M McQueen. *High-Performance Computing in Biomedical Research*, pages 51–59, 2020.

[121] Charles S Peskin and David M McQueen. *Journal of Computational Physics*, 37(1):113–132, 1980.

[122] Charles S Peskin and David M McQueen. *Journal of Computational Physics*, 81(2):372–405, 1989.

[123] Lisa J Fauci and Charles S Peskin. *Journal of Computational Physics*, 77(1):85–108, 1988.

[124] Lisa J Fauci. *Journal of Computational Physics*, 86(2):294–313, 1990.

[125] Bengt Fornberg and David M Sloan. *Acta Numerica*, 3:203–267, 1994.

[126] David Gottlieb and Steven A Orszag. *Numerical analysis of spectral methods: theory and applications*. SIAM, Philadelphia, 1977.

[127] Claudio Canuto, M. Yousuff Hussaini, Alfio Quarteroni, and Thomas A. Zang. *Spectral Methods in Fluid Dynamics*. Springer Berlin, Heidelberg, Berlin, 2012.

[128] John P Boyd. *Chebyshev and Fourier spectral methods*. Courier Corporation, Mineola, 2001.

[129] Rodrigo Ledesma-Aguilar, Hartmut Löwen, and Julia M Yeomans. *Eur. Phys. J. E*, 35:1–9, 2012.

[130] Hartmut Löwen. *Eur. Phys. J. Special Topics*, 225:2319–2331, 2016.

[131] Yingzi Yang, Feng Qiu, and Gerhard Gompper. *Phys. Rev. E*, 89(1):012720, 2014.

[132] Felix Kümmel, Borge Ten Hagen, Raphael Wittkowski, Ivo Buttinoni, Ralf Eichhorn, Giovanni Volpe, Hartmut Löwen, and Clemens Bechinger. *Phys. Rev. Letters*, 110(19):198302, 2013.

[133] A Kaiser and H Löwen. *Phys. Rev. E*, 87(3):032712, 2013.

[134] Jinxing Li, Berta Esteban-Fernández de Ávila, Wei Gao, Liangfang Zhang, and Joseph Wang. *Science Robotics*, 2(4):eaam6431, 2017.

[135] Alexandre M Roma, Charles S Peskin, and Marsha J Berger. *Journal of Computational Physics*, 153(2):509–534, 1999.

[136] Takuji Ishikawa, MP Simmonds, and Timothy J Pedley. Hydrodynamic interaction of two swimming model micro-organisms. *Journal of Fluid Mechanics*, 568:119–160, 2006.

[137] Nicholas G Chisholm, Dominique Legendre, Eric Lauga, and Aditya S Khair. A squirmer across reynolds numbers. *Journal of Fluid Mechanics*, 796:233–256, 2016.

[138] LD Meshalkin and Ia G Sinai. *Journal of Applied Mathematics and Mechanics*, 25(6):1700–1705, 1961.

[139] Francesco Ginelli. *Eur. Phys. J. Special Topics*, 225:2099–2117, 2016.

[140] Dóra Bárdfalvy, Viktor Škultéty, Cesare Nardini, Alexander Morozov, and Joakim Stenhammar. *Communications Physics*, 7(1):93, 2024.

[141] Viktor Škultéty, Dóra Bárdfalvy, Joakim Stenhammar, Cesare Nardini, and Alexander Morozov. *Journal of Fluid Mechanics*, 980:A28, 2024.

[142] Richard S Sutton and Andrew G Barto. *Reinforcement learning: An introduction*. MIT press, Cambridge, 2018.

[143] Francesco Borra, Luca Biferale, Massimo Cencini, and Antonio Celani. *Phys. Rev. Fluids*, 7(2):023103, 2022.

[144] Chiara Calascibetta, Luca Biferale, Francesco Borra, Antonio Celani, and Massimo Cencini. *Eur. Phys. J. E*, 46(3):9, 2023.

[145] Mischa Putzke and Holger Stark. *Eur. Phys. J. E*, 46(6):48, 2023.

[146] Mihir Durve, Fernando Peruani, and Antonio Celani. *Phys. Rev. E*, 102(1):012601, 2020.

[147] K Gustavsson, MZ Sheikh, D Lopez, A Naso, Alain Pumir, and B Mehlig. Effect of fluid inertia on the orientation of a small prolate spheroid settling in turbulence. *New J. Phys.*, 21(8):083008, 2019.

[148] Michelle H DiBenedetto, Jeffrey R Koseff, and Nicholas T Ouellette. Orientation dynamics of nonspherical particles under surface gravity waves. *Phys. Rev. Fluids*, 4(3):034301, 2019.